Uranium Isotope Variations in Nature:

Mechanisms, Applications, and Implications

by

Gregory A. Brennecka

A Dissertation Presented in Partial Fulfillment
of the Requirements for the Degree
Doctor of Philosophy

Approved July 2011 by the
Graduate Supervisory Committee:

Meenakshi Wadhwa, Co-Chair
Ariel Anbar, Co-Chair
Achim Herrmann
Richard Hervig
Patrick Young

ARIZONA STATE UNIVERSITY

December 2011

ABSTRACT

Historically, uranium has received intense study of its chemical and isotopic properties for use in the nuclear industry, but has been largely ignored by geoscientists despite properties that make it an intriguing target for geochemists and cosmochemists alike. Uranium was long thought to have an invariant $^{238}U/^{235}U$ ratio in natural samples, making it uninteresting for isotopic work. However, recent advances in mass spectrometry have made it possible to detect slight differences in the $^{238}U/^{235}U$ ratio, creating many exciting new opportunities for U isotopic research.

Using uranium ore samples from diverse depositional settings from around the world, it is shown that the low-temperature redox transition of uranium (U^{6+} to U^{4+}) causes measurable fractionation of the $^{238}U/^{235}U$ ratio. Moreover, it is shown experimentally that a coordination change of U can also cause measurable fractionation in the $^{238}U/^{235}U$ ratio. This improved understanding of the fractionation mechanisms of U allows for the use of the $^{238}U/^{235}U$ ratio as a paleoredox proxy. The $^{238}U/^{235}U$ ratios of carbonates deposited spanning the end-Permian extinction horizon provide evidence of pronounced and persistent widespread ocean anoxia at, or immediately preceding, the extinction boundary.

Variable $^{238}U/^{235}U$ ratios correlated with proxies for initial Cm/U in the Solar System's earliest objects demonstrates the existence of ^{247}Cm in the early Solar System. Proof of variable $^{238}U/^{235}U$ ratios in meteoritic material forces a substantive change in the previously established procedures of Pb-Pb dating, which assumed an invariant $^{238}U/^{235}U$ ratio. This advancement improves the

accuracy of not only the Pb-Pb chronometer that directly utilizes the $^{238}U/^{235}U$ ratio, but also for short-lived radiometric dating techniques that indirectly use the $^{238}U/^{235}U$ ratio to calculate ages of Solar System material.

ACKNOWLEDGMENTS

While this document officially only has one author, this dissertation would never have been produced if it were not for a large group of brilliant and supportive people that influenced me and this research along the way.

First, I would like to thank my advisory committee, in particular Ariel Anbar and Meenakshi Wadhwa, who not only provided great advice and support, but also allowed me the freedom to pursue ideas that were not necessarily always in line with the current research in their labs. Several people at ASU that were not part of my advisory committee had a major influence on my academic career – I would like to thank the members of the AnbarLab and the ASU Center for Meteorite Studies for all the suggestions and support, and, in particular Gwyn Gordon and Phil Janney for their infinite patience and time spent in the lab and on various machines collecting isotopic data. I would also like to thank Laura Wasylenki, who is a great influence on anyone, and was especially generous with her time during my graduate career. Additionally at ASU, I would like to thank my friends and officemates for the countless office discussions (some useful, most not) that make graduate life a lot of fun.

I was extremely fortunate during my graduate career to work with exceptional external collaborators. I would like to thank Stefan Weyer for his efforts in not only developing capabilities to measure uranium isotopes, but for his time and advice during the projects we worked on together. Additionally, I would like to thank the nuclear forensics group at Lawrence Livermore National Laboratory for inspiring me to pursue a PhD in isotope geochemistry. That group, and in particular Lars Borg, Erick Ramon, and Ian and Nancy Hutcheon provided (and continue to provide) world-class advice and support, both personally and scientifically. I will always be grateful.

Lastly, I would like to thank my long-term partner and future wife, Celeste Riley, for her support throughout my entire graduate career. Her patience with late nights, travel, and endless talk about various isotopes has been incredible.

TABLE OF CONTENTS

Page

LIST OF TABLES x

LIST OF FIGURES xi

CHAPTER

1 INTRODUCTION TO THE URANIUM ISOTOPE SYSTEM 1

1.1 Brief History of the Study of Uranium Isotopes 1

1.1.1 The Basics of the Uranium Isotope System 1

1.1.2 Early Peacful Studies of Uranium Isotopes 2

1.1.3 The Nuclear Volume Effect 3

1.1.4 The Discovery of ^{238}U/^{235}U Variability on Earth 4

1.2 Opportunities Created by Variable ^{238}U/^{235}U Ratios 6

2 NATURAL VARIATIONS IN URANIUM ISOTOPE RATIOS OF URANIUM ORE CONCENTRATES: UNDERSTANDING THE FRACTIONATION MECHANISM 8

2.1 Introduction 8

2.2 Background 10

2.2.1 Previous ^{238}U/^{235}U Ore Deposit Work 10

2.2.2 Sample Types 11

2.3 Methods 13

2.3.1 Sample Preparation 13

2.3.2 Isotope Ratio Measurements 13

2.4 Results 16

Chapter Page

2.5 Discussion 20

2.5.1 Production of UOC 20

2.5.2 Preferential Leaching of Isotopes 21

2.5.3 Isotope Fractionation via Redox Changes 23

2.5.4 Nuclear Forensics and Uranium Isotope Variations .. 26

2.5.5 Conclusion 27

3 URANIUM ISOTOPE FRACTIONATION DURING ADSORPTION TO MN-OXYHYDROXIDES 29

3.1 Introduction 29

3.2 Experimental Procedures 31

3.2.1 Experimental Setup 31

3.2.2 Concentration Determinations 32

3.2.3 Isotope Ratio Measurements 32

3.2.4 EXAFS Measurements 34

3.3 Results 35

3.3.1 Concentration Results 35

3.3.2 Isotopic Results 36

3.3.3 EXAFS Results 38

3.4 Discussion 41

3.4.1 Fractionation Mechanisms of Heavy Elements 41

3.4.2 Isotope Effect Matching that Observed in Nature 42

3.4.3 Coordination of U Adsorbed to Birnessite 43

Chapter Page

3.4.4 Mechanism of Adsorption and Fractionation? 46

3.4.5 Applications of $^{238}U/^{235}U$ Variability 46

4 RAPID EXPANSION OF OCEANIC ANOXIA IMMEDIATELY BEFORE THE END-PERMIAN MASS EXTINCTION 48

4.1 Introduction 48

4.2 Background 49

4.3 Results and Discussion 50

4.3.1 Uranium Isotopes Over the Extinction Horizon......... 50

4.3.2 Quantifying Increased Anoxic Deposition 53

4.3.3 Th/U Ratios of the Dawen Carbonates 55

4.3.4 Implications for Late-Permian Ocean Models 56

4.4 Methods and Further Discussion 59

4.4.1 Sample Preparation and Measurement 59

4.4.2 Discussion on Secondary Alteration of Carbonates... 62

5 $^{238}U/^{235}U$ VARIATIONS IN METEORITES: EXTANT ^{247}CM AND IMPLICATIONS FOR PB-PB DATING 66

5.1 Introduction 66

5.2 Background 67

5.3 Results 68

5.4 Discussion 71

5.4.1 Elemental Fractionation in CAIs 71

Chapter Page

5.4.2 Determining the Interval of Free Decay 74

5.4.3 Implications for Pb-Pb Dating 75

5.5 Methods 77

6 URANIUM ISOTOPE COMPOSITIONS OF THE BASALTIC ANGRITE METEORITES AND THE CHRONOLOGICAL IMPLICATIONS FOR THE EARLY SOLAR SYSTEM 82

6.1 Introduction 82

6.2 Background 83

6.2.1 Time Anchors 83

6.2.2 Angrites as Time Anchors 83

6.3 Results 85

6.4 Discussion and Implications 87

6.4.1 Age Change of Angrites 87

6.4.2 Uranium Isotopes of the Angrite Parent Body 90

6.4.3 Chronometer Concordance 91

6.5 Materials and Methods 94

REFERENCES 99

APPENDIX

A BARIUM, NEODYMIUM, AND SAMARIUM ISOTOPIC COMPOSITIONS OF REFRACTORY INCLUSIONS 111

Appendix Page

A.1 Introduction 114

A.2 Materials and Methods 117

  A.2.1 Barium Isotopic Measurement 118

  A.2.2 Neodymium Isotopic Measurement 119

  A.2.3 Samarium Isotopic Measurement 119

A.3 Results 120

  A.3.1 Barium Isotopes 120

  A.3.2 Neodymium Isotopes 121

  A.3.3 Samarium Isotopes 122

A.4 Discussion 127

  A.4.1 Evidence of ^{138}La decay to ^{138}Ba 127

  A.4.2 Comparison to previous isotopic data 128

  A.4.3 Evidence of extant ^{135}Cs? 129

  A.4.4 Origin of isotopic anomalies in CAIs? 129

    A.4.4.1 Mixing of FUN or presolar components .. 130

    A.4.4.2 Incomplete digestion of materials 132

    A.4.4.3 Neutron capture and normalization 133

    A.4.4.4 Nuclear field shift fractionation 136

    A.4.4.5 Supernovae input after CAI formation 141

A.5 Conclusion 141

B PERMISSION FROM CO-AUTHORS 144

LIST OF TABLES

Table Page

2.1 UOC Sample Description and Results 17

3.1 Uranium Isotopic Data from Adsorption Experiments 38

3.2 EXAFS Fitting Results 41

4.1 Data from Dawen Carbonates 53

5.1 Isotopic and Elemental Ratios of Allende CAIs 73

5.2 Uranium Standard and Instrument Parameter Data 78

6.1 $^{238}U/^{235}U$ Ratios of Samples of this Study.. 87

6.2 Recalculated Pb-Pb ages of Various Angrites.................................... 90

6.3 Weights and U Contents of Samples of this Study 96

A.1 Nucleosynthetic pathways of Ba, Nd, and Sm isotope creation...... 116

A.2 Ba isotopic and La/Ba ratios of Allende CAIs................................ 124

A.3 Nd isotopic and $^{147}Sm/^{144}Nd$ ratios of Allende CAIs...................... 125

A.4 Sm isotopic ratios of Allende CAIs... 126

LIST OF FIGURES

Figure Page

1.1 Box Model of Terrestrial U Reservoirs 5

2.1 Comparison of Uranium Standard Data 15

2.2 $^{238}U/^{235}U$ Ratios of Uranium Ore Concentrates 18

2.3 $^{235}U/^{234}U$ Ratios of Uranium Ore Concentrates 18

2.4 $^{238}U/^{235}U$ vs. $^{235}U/^{234}U$ Ratios of Uranium Ore Concentrates 22

3.1 Percent Uranium Adsorped on Birnessite 36

3.2 Isotopic Results of U Adsorption on Birnessite 37

3.3 EXAFS Spectra k^3 vs. k 39

3.4 EXAFS Spectra Fourier Transform vs. R+ΔR 40

4.1 Location Map and Stratigraphic Column of Dawen Carbonates 49

4.2 Data Plots from Dawen Carbonates 51

4.3 Box Model of Modern and Late-Permian Oceans 55

4.4 Long Term Reproducibility of Uranium Standards 61

4.5 Cross Plots of U/Al and %Dolomite vs. Th/U and $\delta^{238}U$ 65

5.1 $^{238}U/^{235}U$ Variation in CAIs 68

5.2 $^{238}U/^{235}U$ Correlation with Th/U and Nd/U 70

5.3 REE Patterns of Allende CAIs 72

5.4 Age Adjustment Required by $^{238}U/^{235}U$ Values 76

5.5 Long Term Reproducibility at different U concentrations 80

6.1 $^{238}U/^{235}U$ Ratio of Angrites 86

6.2 Recalculated Pb-Pb Ages 89

Figure Page

6.3 Chronometer Concordance 92

6.4 External Reproducibility of the SRM950a Standard 97

A.1 Average Ba Isotopic Composition of Allende CAIs 121

A.2 Average Nd Isotopic Composition of Allende CAIs 122

A.3 Average Sm Isotopic Composition of Allende CAIs........................ 123

A.4 Evidence of ^{138}Ba Ingrowth from ^{138}La 128

A.5 Ba, Nd, and Sm Isotopic Compositions of SiC and EK1-4-1........... 131

A.6 Alternate Normalizations of Sm Isotope Data 134

A.7 Predicted Neutron Capture Correlation 135

A.8 Barium Nuclear Field Shift Effects 137

A.9 Neodymium Nuclear Field Shift Effects.. 138

A.10 Samarium Nuclear Field Shift Effects... 138

A.11 Molybdenum Nuclear Field Shift Effects 139

A.12 Nickel Nuclear Field Shift Effects.. 140

A.13 Tellurium Nuclear Field Shift Effects 140

Chapter 1

INTRODUCTION TO THE URANIUM ISOTOPE SYSTEM

1.1 BRIEF HISTORY OF THE STUDY OF THE URANIUM SYSTEM

1.1.1 The Basics (and Potential) of the Uranium Isotope System

Since the 1930s, uranium (U) has received a great deal of attention from government officials and scientists worldwide, largely due to the fissile properties of the ^{235}U nucleus. While this attention to U has had a great deal of geopolitical consequences far beyond the scope of this thesis, it has also produced a vast knowledge about the chemical behavior of U. This knowledge is of great use for the scientific endeavors that are at the crux of this thesis.

While a large portion of the study of U has been dedicated to energy production, either in the form of nuclear reactors on nuclear weapons, U has many properties that make it an intriguing target for geoscientists and cosmochemists alike. The two primordial U isotopes, ^{238}U ($t_{1/2} \approx 4.5$ Ga) and ^{235}U ($t_{1/2} \approx 703$ Ma), have very long, non-overlapping decay chains, making them very powerful tools for geochronology. The α-decay of ^{238}U indirectly produces ^{234}U, a short-lived isotope ($t_{1/2} \approx 245{,}000$ a). In addition to these natural isotopes, ^{233}U ($t_{1/2} \approx 160{,}000$ a) and ^{236}U ($t_{1/2} \approx 23.4$ Ma) can be produced in substantial quantities by specific nuclear reactions, creating excellent geochemical tracers. Furthermore, U is a redox sensitive metal, suggesting its isotopes can be used to trace geochemical reactions over time, allowing for a more complete understanding of geologic history.

1.1.2 Early Peaceful Studies of Uranium Isotopes

It was realized early on that the long-lived decay systems of $^{238}U \rightarrow ^{206}Pb$ and $^{235}U \rightarrow ^{207}Pb$ would be of great importance for chronology (Boltwood 1907), and were later used to determine the age of meteorites and Earth (Patterson 1956). These chronometers can be used separately, in the case of U-Pb dating, or combined in Pb-Pb dating. In Pb-Pb dating, the ratio of the Pb daughter products ($^{206}Pb^*$ and $^{207}Pb^*$) from the decay of ^{238}U and ^{235}U, respectively are measured to calculate an age for the material. This equation is shown below, where "λ" is the decay constant of the parent isotope and "t" is time:

$$\frac{^{207}Pb^*}{^{206}Pb^*} = \frac{^{235}U \;\; e^{\lambda_{235}t} - 1}{^{238}U \;\; e^{\lambda_{238}t} - 1} = \frac{1}{137.88} \; \frac{e^{\lambda_{235}t} - 1}{e^{\lambda_{238}t} - 1}$$

Since no variation in natural U isotopes had ever been measured, this equation assumed the value of the $^{238}U/^{235}U$ ratio to be equal to 137.88.

Additional work on U isotopes showed that excesses of ^{234}U, an intermediate daughter of ^{238}U decay, existed in aqueous phases. This disequilibrium reflects the increased mobility of ^{234}U relative to other U isotopes, caused by preferential leaching of ^{234}U from damaged crystal sites from the α-decay of ^{238}U (Kigoshi 1971). Discovery of $^{234}U/^{238}U$ disequilibrium provided a short-term chronometer and tracer of U mobility.

During the late 1970s, huge $^{238}U/^{235}U$ variations were reported in various meteoritic materials and used as proof of extant ^{247}Cm (an isotope produced in supernovae that decays to ^{235}U) (Arden 1977; Tatsumoto and Shimamura 1980). Continued work on the $^{238}U/^{235}U$ ratio in the same and similar samples showed the claims of large $^{238}U/^{235}U$ variations in meteoritic material to be false (Chen and Wasserburg 1980; Shimamura and Lugmair 1981; Lugmair and Galer 1992; Stirling et al. 2005). While the early claims of ^{247}Cm were discredited, the existence of "live" ^{247}Cm in the early Solar System was still predicted based on data for other short-lived radioisotopes such as ^{129}I and ^{244}Pu that are thought to be produced in similar stellar environments as ^{247}Cm.

1.1.3 The Nuclear Volume Effect

By the end of the 1980s, it had been firmly established by measurements of various meteorite samples and countless U ores provided by the U mining industry that the modern $^{238}U/^{235}U$ ratio was an invariant value (=137.88) in our Solar System (Shields 1960; Chen and Wasserburg 1980; Chen and Wasserburg 1981). Uranium was thought to be too heavy to undergo significant mass-dependent isotope fractionation. However, theoretical work by Fujii (1989), Bigeleisen (1996), and Schauble (2006, 2007) suggested that fractionation of U isotopes should occur during chemical reactions involving redox change. The mechanism of fractionation postulated by these theorists was not the more familiar mass-dependent fractionation, but volume-dependent fractionation. For very heavy elements like U, the nuclei are of sufficient size to influence the distribution of electrons around the nucleus (Bigeleisen 1996). Thus, the differing volumes of the nuclei rather than strictly their masses alter the zero point energy of the isotopes, causing preferential bonding and isotope fractionation. This type of fractionation is therefore referred to as the "nuclear volume effect."

It was shown in Schauble (2007) that volume-dependent fractionation and mass-dependent fractionation in Tl and Hg are both predicted to enrich heavy isotopes in the oxidized species. Oxidation of Hg(0) or Tl(I) involves loss of 6s electrons, reducing the electron density at each nucleus. However, U differs from Hg and Tl in a critical way: the oxidation of U(IV) to U(VI) involves 5f electrons, and their removal actually increases the electronic charge density at the nucleus, leading to a preference of light U isotopes in the oxidized species (Schauble, unpublished). Consequently, the effects of mass-dependent and volume-dependent fractionation on the $^{238}U/^{235}U$ ratio are in opposite directions, leaving the dominant volume-dependent fractionation as the observable effect.

The effect of temperature (T) in mass-dependent fractionation has been well documented, with the magnitude of fractionation scaling as $1/T^2$. The magnitude of volume-dependent fractionation is also a function of T, but instead scales as 1/T (Schauble 2007). Therefore, while U behaves differently from other very heavy elements in the direction of volume-dependent fractionation, the importance of temperature on the reactions remains the same.

A thorough discussion of the nuclear volume effect and its increased importance for very heavy nuclei is provided by Bigeleisen (1996) and Schauble (2007).

1.1.4 The discovery of $^{238}U/^{235}U$ variability on Earth

The development and maturation of multi-collector mass spectrometers gave scientists the ability to measure multiple ion beams simultaneously, greatly improving the precision of isotopic ratio measurements. Using multi-collection capability, Stirling et al. (2007) and Weyer et al. (2008) were the first to show natural variability in the terrestrial $^{238}U/^{235}U$ ratio. The samples measured in both studies strongly suggested that low-temperature redox transitions were the major cause of $^{238}U/^{235}U$ fractionation. Interestingly, the reduced species, U^{IV} was isotopically heavier than the oxidized species, U^{VI}, as displayed in Figure 1. This pattern was opposite to that of lighter elements such as Fe or S, providing evidence that the predicted volume dependency, and not mass dependency, was the likely driving force behind the observed $^{238}U/^{235}U$ fractionation. Also shown in Stirling et al. (2007) and Weyer et al. (2008) was a measurable offset between U in seawater and U contained in ferromanganese crusts, both oxidized forms of U in which redox fractionation was not the cause of U isotope fractionation.

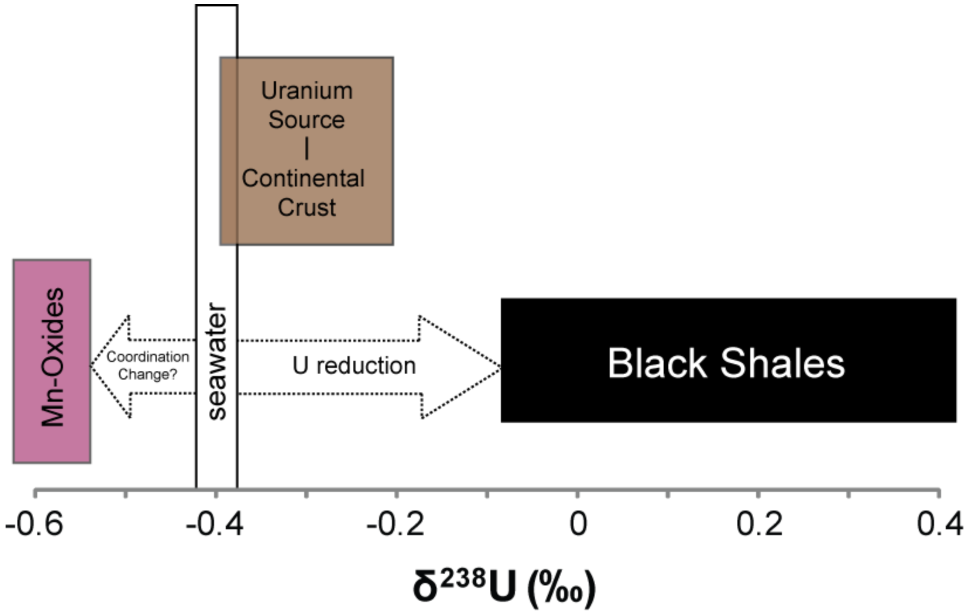

Fig. 1.1. Box model showing U isotope compositions and ranges of various terrestrial U reservoirs. The dotted arrows show the possible causes of U isotope fractionation. Data and figure redrawn from Weyer et al. (2008).

1.2 OPPORTUNITIES CREATED BY VARIABLE ^{238}U/^{235}U RATIOS

The exciting affirmation of variability in the ^{238}U/^{235}U ratio and the improved precision at which the ratio can be measured created many opportunities for new work on the U isotope system. The goal of this thesis is to address some important areas in which high precision ^{238}U/^{235}U ratio measurements could be useful to understand scientific questions, both in terrestrial and extraterrestrial systems.

First, this thesis explores and addresses possible fractionation mechanisms that cause ^{238}U/^{235}U variability in Earth systems, using both natural and experimental samples. Separate studies investigate possible redox driven fractionation and the hypothesized fractionation due to a coordination change of U. Additionally, this thesis examines the use of the ^{238}U/^{235}U ratio as a redox proxy to study the history of oxygen in the Earth's oceans over geologic time.

This thesis utilizes variable ^{238}U/^{235}U ratios in the Solar System's earliest objects to determine the existence of ^{247}Cm and quantify the initial ^{247}Cm/^{235}U ratio of the Solar System. The proof of variable ^{238}U/^{235}U ratios in meteoritic material shown in this thesis forces a substantive change in the previously established procedures of Pb-Pb dating, which previously assumed an invariant ^{238}U/^{235}U ratio. This advancement will improve the accuracy of not only the Pb-

Pb chronometer that directly utilizes the $^{238}U/^{235}U$ ratio, but also for short-lived radiometric dating techniques that indirectly use the $^{238}U/^{235}U$ ratio to calculate ages of Solar System material.

Chapter 2

NATURAL VARIATIONS IN URANIUM ISOTOPE RATIOS OF URANIUM ORE CONCENTRATES: UNDERSTANDING THE FRACTIONATION MECHANISM

2.1 INTRODUCTION

The uranium isotope system is unusual in that it contains two long-lived natural isotopes in ^{238}U ($t_{1/2} \approx 4.5$ Ga) and ^{235}U ($t_{1/2} \approx 700$ Ma), as well as ^{234}U, a short-lived isotope ($t_{1/2} \approx 245{,}000$ a) that is part of the ^{238}U decay chain. This isotope system has been well studied not only because of the fissile properties of ^{235}U, but also because of its wide applications in the age dating of natural materials. The decay systems of $^{238}\text{U} \rightarrow {}^{206}\text{Pb}$ and $^{235}\text{U} \rightarrow {}^{207}\text{Pb}$ provide both long and short-range chronometers when utilizing intermediate decay products, such as ^{234}U.

Until very recently it was assumed that the current ^{238}U/^{235}U ratio was a constant value (=137.88) in our Solar System because uranium was thought to be too heavy to undergo significant isotope fractionation. Theoretical work by Fujii (1989), Bigeleisen (1996), and Schauble (2006, 2007) suggested, however, that fractionation in uranium isotopes should be present and measurable with modern analytical techniques. Recent work has in fact shown variability in the terrestrial ^{238}U/^{235}U ratio over a range of ~1.3‰ (Stirling et al. 2007; Weyer et al. 2008). This study utilizes modern multi-collector ICP-MS technology to analyze 40 uranium ore concentrate samples from U ore mines across the world to search not only for differences in the $^{238}U/^{235}U$ and $^{235}U/^{234}U$ ratios, but to identify the specific mechanisms that cause the $^{238}U/^{235}U$ fractionation.

Although significant variations in the $^{238}U/^{235}U$ ratio are a recent discovery, much larger variations in the $^{234}U/^{235}U$ ratio in the terrestrial variations have long been observed. The ocean, for example, contains elevated abundances of ^{234}U. Specifically, the increased mobility of ^{234}U relative to other U isotopes reflects production from ^{238}U by α-decay and subsequent emplacement in crystal sites damaged by α-recoil. Aqueous weathering of materials containing U results in preferential leaching of ^{234}U from these α-damaged crystal sites (Kigoshi 1971).

If preferential leaching is also the primary mechanism for $^{238}U/^{235}U$ fractionation, the magnitude of changes in $^{238}U/^{235}U$ should be positively correlated with those in $^{235}U/^{234}U$. On the other hand, $^{238}U/^{235}U$ variations have been attributed to oxidation and reduction (redox) processes (Schauble 2006; Stirling et al. 2007; Weyer et al. 2008; Bopp et al. 2009). In this scenario, the ability of individual U nuclei to attract electrons varies slightly due to the different number of neutrons in the nucleus of ^{238}U and ^{235}U. This has been termed the “nuclear volume effect”.

If reduction of U^{VI} to U^{IV} is a major cause of isotope fractionation in the uranium system, then uranium ores deposited in variable oxidation conditions should show resolvable differences in uranium isotope abundances. By examining the relationship between all three naturally occurring uranium isotopes in samples deposited by: 1) low-temperature redox processes, 2) high-temperature redox processes and 3) non-redox processes, it should be possible to determine the relative importance of preferential leaching and redox changes at high and low-temperatures in fractionation of the $^{238}U/^{235}U$ ratio.

2.2 BACKGROUND

2.2.1 Previous $^{238}U/^{235}U$ ore deposit work

Early work by Cowan and Adler (1976) on the $^{238}U/^{235}U$ ratio in uranium ore samples concluded that there was a bimodal distribution of uranium ores with a statistically significant, ~+0.3‰ difference between sandstone-type and magmatic deposits. Their study also concluded that there were insufficient data to attribute the variations either to fractionation of uranium isotopes between magmatic and sandstone deposits, or ^{235}U depletion caused by Precambrian nuclear reactions. This work was performed using UF_6 gas mass spectrometers, achieving a reported precision of ~0.4‰ on the $^{238}U/^{235}U$ ratio. However, the UF_6 was sometimes stored in containers that previously contained depleted uranium (i.e., $^{238}U/^{235}U>>137$), creating a potential source of contamination and making the results of the study somewhat ambiguous. A more recent study by Bopp et al. (2009) examined uranium ore from six uranium mines, sampling two low-temperature deposits and four high-temperature deposits. This study concluded that $^{238}U/^{235}U$ fractionation takes place during the low-temperature redox transition, citing higher $^{238}U/^{235}U$ ratios from low-temperature deposits. This study involves a significantly more diverse sample suite in order to determine the cause of the $^{238}U/^{235}U$ ratio variations in ore deposits by testing all likely modes of isotope fractionation.

2.2.2 Sample Types

Uranium ore concentrate (UOC; née, yellowcake) is a fungible commodity traded worldwide and is the final product of uranium mining and milling operations. Uranium deposits occur worldwide in a variety of geologic settings and can be divided into 3 major depositional settings based on the temperature and the redox environment of deposition. The major settings, coupled with examples of typical uranium deposit types, are described briefly below.

1) ***Low-Temperature, Redox Sensitive*** **–** consist primarily of sandstone or "roll-front" deposits, but also included in this category are black shale uranium deposits. Uranium mineralization occurs below the water table where low-temperature, oxidized fluids (carrying soluble U^{VI}) interact with a reducing agent, usually carbonaceous material, sulfides, or hydrocarbons, and precipitate uranium as insoluble U^{IV} (IAEA-TEC-DOC-328, 1985). Major examples include the sandstone deposits of the Syr-Darya basin in Kazakhstan, the Arlit district of Niger, and the gulf coast deposits of Texas, USA.
2) ***High-Temperature, Redox Sensitive*** **–** includes some of the largest and richest uranium deposits in the world. Like sandstone and black shale deposits, this category includes uranium deposited because of the reduction of U^{VI} to U^{IV}, but at higher temperatures associated with igneous

and metamorphic processes. Uranium deposits in this category include unconformity deposits, vein-type deposits, intrusive deposits, metamorphic core complex deposits and collapse breccia-pipe deposits. Major examples include the massive Olympic Dam breccia complex and unconformity-style Ranger deposits of Australia, as well as Namibia's intrusive-style Rössing deposit.

3) ***Non-Redox Sensitive*** **–** this setting exclusively contains quartz-pebble conglomerate deposits. These are ancient deposits formed from fluvial oligomictic detritus (including pyrite and uraninite) prior to the emergence of an oxygenated atmosphere on Earth, and therefore not deposited by a redox related mechanism (IAEA-TEC-DOC-427, 1987). The Stanleigh, Stanrock and Denison deposits of Canada are all examples of quartz-pebble conglomerate deposits.

By examining the uranium isotope composition of samples from these deposits, the goal is to constrain the potential roles preferential leaching, oxidation, and temperature play in fractionating the isotopes of uranium in the terrestrial environment. If fractionation patterns reflect preferential leaching of isotopes, variations in $^{238}U/^{235}U$ and $^{235}U/^{234}U$ will be positively correlated and not dependent on the oxidation environment. If, in contrast, the pattern of U-isotope shifts reflects oxidation/reduction, as suggested by Weyer et al. (2008), U-isotope fractionation will be pronounced in the redox-related deposits and absent from the non-redox deposits. The role that temperature may play in U isotopic fractionation is evaluated by analyzing U-ores that formed at both low and high temperatures.

2.3 METHODS

2.3.1 Sample Preparation

Samples were obtained as UOC; an aliquot of ~100 mg was removed and placed into a 50 ml centrifuge tube. The sample was dissolved using 20 ml of 4M HNO_3. From the solution, an aliquot of 250 µl was removed and brought to 4 ml in a 3M HNO_3 + 0.05M HF acid mixture. This solution was passed through a column containing Eichrom® UTEVA resin, following a revised procedure outlined in Weyer et al. (2008) to separate uranium from the matrix. Due to the extremely high uranium concentrations associated with these samples, a $^{236}U/^{233}U$ double spike was added to sample aliquots only after uranium concentrations were determined using a Thermo XSII quadrupole Inductively Coupled Plasma Mass Spectrometer and samples were appropriately diluted for isotope ratio measurements. It has been shown that no measurable U isotope fractionation occurs during the column elution for the procedure used, so timing of spike addition does not affect measured ratios (Weyer et al. 2008).

2.3.2 Isotope Ratio Measurements

High precision uranium isotope ratio measurements were collected on a ThermoFinnigan Neptune MC-ICP-MS instrument at Arizona State University (ASU). Samples dissolved in 2% HNO_3 were introduced by an Apex-Q sample introduction system. $^{238}U/^{235}U$ measurements were performed at concentrations of ~120 ppb U to obtain ~35 volt signal (3.5 x10^{-10} amperes) on ^{238}U. A second, more concentrated aliquot was used for the $^{235}U/^{234}U$ measurement to obtain ~25 V signal on ^{235}U. A $^{236}U/^{233}U$ double-spike was used to correct for instrumental mass bias during the measurements. In order to minimize analytical error associated with the addition of ^{234}U, ^{235}U, and ^{238}U from the spike, samples were spiked to achieve ^{236}U and ^{233}U signals of ~2.5 times the lowest natural isotope for each run. This spiking technique maximizes the counting statistics on the spike masses while minimizing the tailing contributions at mass 235. The spike was calibrated at ASU and has an isotopic composition of $^{236}U/^{233}U = 1.00525$, $^{238}U/^{233}U = 0.000958$, $^{235}U/^{233}U = 0.000108$.

Uranium isotopic data are reported as an average of multiple runs (2 or more), differing by an average value ($^{238}U/^{235}U$) of less than 0.007, or 0.05‰. Each measurement session included multiple (10 or more) runs of CRM 129-A, a certified uranium standard (New Brunswick Laboratory 2003) obtained as a uranium oxide and was put through the same chemistry as all samples. Uncertainties are based on the errors calculated on the replicate runs for the CRM129-A standard ($^{238}U/^{235}U \pm 0.018$; $^{235}U/^{234}U \pm 0.42$), and are reported at the bottom of Table 2.1 for both ratios measured. The standard error of each individual run (30 cycles, 8.4 second integration per cycle) was, in all cases, less than 0.009 for the $^{238}U/^{235}U$ ratio, and less than 0.01 for the $^{235}U/^{234}U$ ratio. The $^{238}U/^{235}U$ value determined on CRM129-A was 137.631±0.018 (2SD) is just inside the analytical uncertainty of the certified value (137.71±0.07). In order to test the spike calibration and assess the accuracy of the newly reported value, aliquots of CRM129-A, IRMM-184 and several selected samples were run using the ^{236}U-^{233}U double spike on the Thermo Triton TI at LLNL. The values determined at LLNL using the Triton were all within analytical uncertainty of those determined at ASU using the Neptune. The 15 runs of CRM129-A on the Triton averaged 137.619±0.018, compared with 32 runs with an average of 137.631±0.018 on the Neptune. Furthermore, the $^{238}U/^{235}U$ ratio determined on IRMM-184 was 137.696±0.011 (n=10), closely matching the certified value 137.697±0.042 (IRMM Certificate 2005). All standard data are displayed in Figure 2.1.

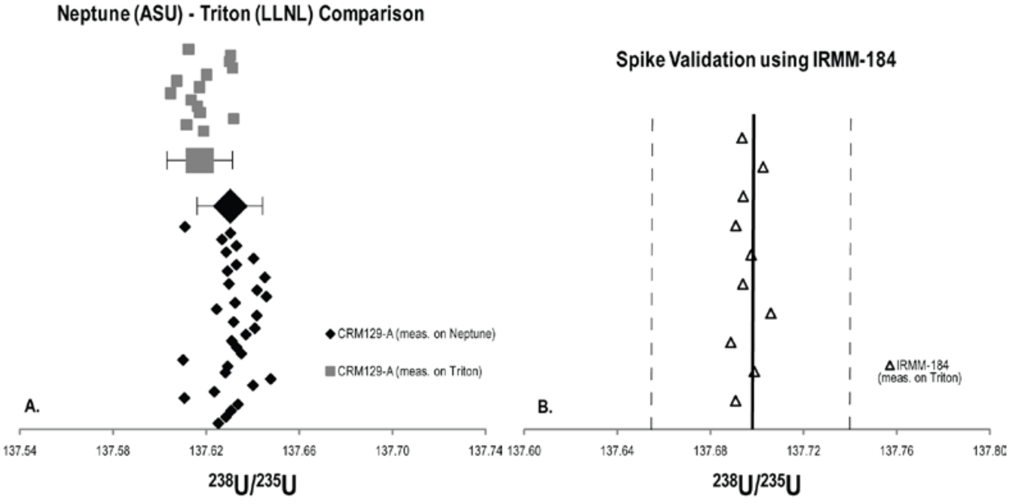

Fig. 2.1. A) Comparison of the data obtained at ASU on a ThermoFinnigan Neptune with data obtained from the same CRM129-A standard solution on a Thermo Triton at LLNL. The average values obtained for $^{238}U/^{235}U$ on CRM129-A are 137.631±0.018 and 137.619±0.018, respectively. The large symbols represent the average and 2SD error for that population. While the values

obtained at ASU and LLNL agree within error of one another, they fall at the very low end of the certified value of CRM129-A, 137.715±0.074. The combined 2SD error reported from ASU and LLNL is substantially smaller than the uncertainty on CRM129-A.

B) Validation of the U-double spike procedure was performed using IRMM-184 on the Triton at LLNL, obtaining a value of 137.696±0.011. The certified value of IRMM-184 is 137.697±0.042, which is shown with the solid vertical line with associated 2SD error on the certified value in dashed lines.

2.4 RESULTS

Uranium isotopic compositions were determined on 40 UOC samples from known locations and depositional settings around the world. Table 2.1 shows the $^{238}U/^{235}U$ and $^{235}U/^{234}U$ ratios of the samples measured in this study. The data are shown graphically in Figures 2.2 and 2.3.

Table 2.1. Uranium isotope ratios of this study are presented here. The far left column indicates the type of geochemical environment in which the deposit was formed (Category), and the second column from the left indicates the geologic classification of the deposit (Deposit type). At the bottom of the chart, the average error (2SD) is reported, based on the multiple runs of the CRM129-A standard for both $^{238}U/^{235}U$ (n=40) and $^{235}U/^{234}U$ (n=15).

TABLE 2.1 SAMPLE DESCRIPTION AND RESULTS

Category	Deposit type	Country and mine name	$^{238}U/^{235}U$	$^{235}U/^{234}U$
Low-Temp Redox	Sandstone	Czech Rep. - Straz Pod Ralskem	137.848	83.63
	Sandstone	Gabon - Mouana	137.859	136.75
	Sandstone	Kazakhstan - Kanzhugan	137.934	134.85
	Sandstone	Kazakhstan - Uvanas	137.934	161.61
	Sandstone	Niger – Arlit	137.895	123.89
	Sandstone	Serbia – Rudnik	137.961	138.98
	Black Shale	Sweden - Ranstadt	137.865	164.17
	Sandstone	USA - El Mesquite	137.891	146.48
	Sandstone	USA - Everest Black	137.871	133.01
	Sandstone	USA - Everest Yellow	137.909	144.78
	Sandstone	USA - Falls City	137.892	153.47
	Sandstone	USA – Irigary	137.821	126.85
	Sandstone	USA - Lucky McGill	137.887	134.70
	Sandstone	USA - Pathfinder	137.871	134.70
	Sandstone	USA – Petromic	137.852	140.56
	Sandstone	USA - Shirley Basin	137.871	134.58
	Sandstone	USA - Susquehan	137.918	151.02
High-Temp Redox	Metamorphic	Australia - Mary Kathleen	137.833	132.37
	Breccia Complex	Australia - Olympic Dam	137.845	135.52
	Intrusive	Australia - Radium Hill	137.836	136.71
	Unconformity	Australia - Ranger	137.846	135.05
	Unconformity	Australia - Rum Jungle	137.846	134.38
	Unconformity	Australia - South Alligator	137.826	134.51
	Intrusive	Canada – Dyno	137.843	135.26
	Vein	Canada - El Dorado	137.809	134.51
	Intrusive	Canada - Faraday	137.837	132.71
	Vein	Canada - Gunnar	137.820	135.42
	Unconformity	Canada - Key Lake	137.792	132.46
	Intrusive	Canada - Madawaska	137.847	132.02
	Unconformity	Canada - Rabbit Lake	137.842	133.76
	Vein	Canada - Rayrock	137.849	135.17
	Vein	DR Congo – Shinkolobwe	137.805	133.01
	Intrusive	Namibia – Rössing	137.836	133.75
	Intrusive	South Africa – Palabora	137.865	132.02
	Vein	USA – Dawn	137.817	133.84
Non-Redox	QP Conglomerate	Canada - Blind River	137.835	136.88
	QP Conglomerate	Canada – Denison	137.855	137.25
	QP Conglomerate	Canada - Miliken Lake	137.826	136.56
	QP Conglomerate	Canada – Stanleigh	137.823	135.78
	QP Conglomerate	Canada – Stanrock	137.831	138.06
		ASU - CRM 129A Standard	137.631	135.98
		ASU - Average error (2SD)	0.018	0.42
		LLNL - CRM 129A Standard	137.619	
		LLNL - Average error (2SD)	0.018	
		CRM 129A Certified Value	137.714	136.11
		Certified error (2SD)	0.074	0.35
		LLNL – IRMM-184 Standard	137.696	
		LLNL - Average error (2SD)	0.011	
		IRMM-184 Certified Value	137.697	
		Certified error (2SD)	0.042	

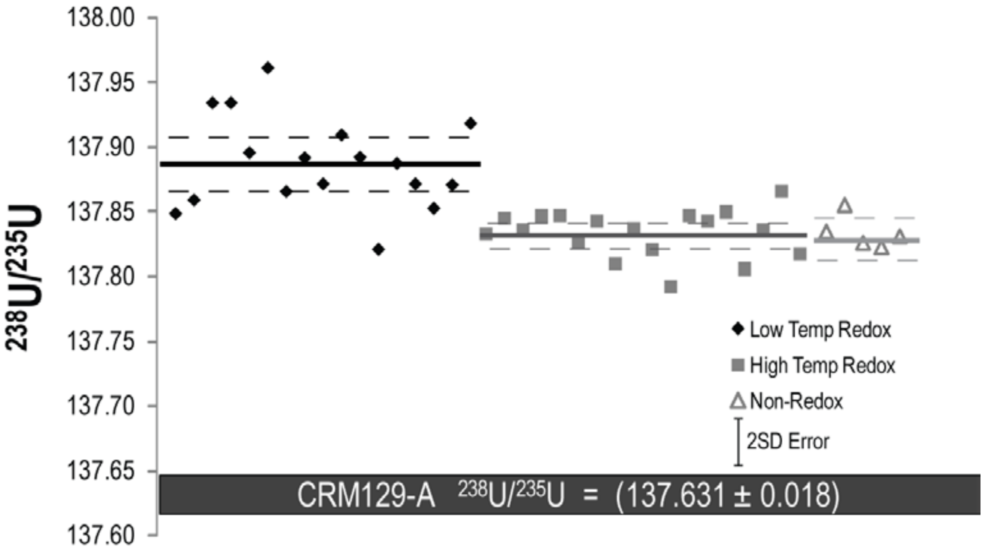

Fig. 2.2. The 40 samples of this study are shown by depositional style and $^{238}U/^{235}U$ values. The solid lines represent the average group values and 2SD standard error is shown for each depositional style in dashed lines. The reported value and external reproducibility of the CRM129a standard is shown as the grey box at the bottom of Figure 2.

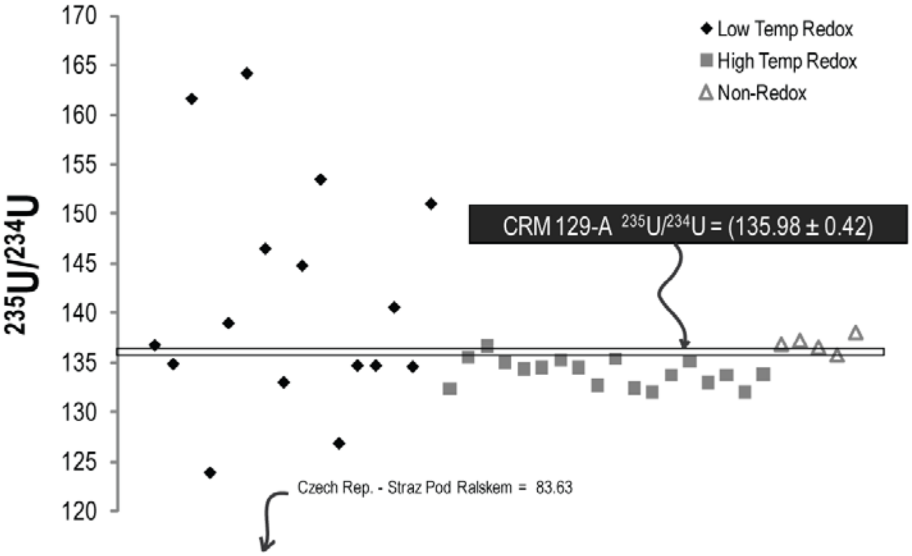

Fig. 2.3. The 40 samples of this study shown by depositional style and $^{235}U/^{234}U$ values. Error bars (2SD) are contained within the symbols. The anomalous Straz Pod Ralskem (Czech Rep.) data point is off scale and noted at the bottom of the figure.

The range of $^{238}U/^{235}U$ observed in the samples is between 137.792 and 137.961, whereas the range of $^{235}U/^{234}U$ is 83.63 to 164.17. These variations are well beyond the uncertainty associated with the $^{238}U/^{235}U$ and $^{235}U/^{234}U$ measurements determined by multiple analyses of standards. From Figure 2.2 it is apparent that the $^{238}U/^{235}U$ values of samples from the high-temperature redox mines and the non-redox mines are indistinguishable from one another. Samples from the low-temperature redox mines are, however, more enriched in ^{238}U (Figure 2.2) and demonstrate significantly greater variability in the $^{238}U/^{235}U$ ratio. Samples from the low temperature environments average 137.887±0.072 (2SD), whereas all other samples average 137.833±0.034 (2SD), a difference of 0.39 ± 0.08‰ (2SD). The $^{235}U/^{234}U$ ratios of the high-temperature and non-redox samples show very little variation in $^{235}U/^{234}U$ and have values approximately consistent with secular equilibrium ($^{235}U/^{234}U \approx 132$). In marked contrast, the low-temperature redox samples show significant scatter, manifest by both enrichments and depletions in ^{234}U (Figure 2.3).

One UOC sample, from the Straz Pod Ralskem mine in the Czech Republic, is extremely enriched in ^{234}U with a $^{235}U/^{234}U$ ratio of only ~84. A U-ore sample from the same location was reported by Richter et al. (1999) to have similarly high amounts of ^{234}U with a reported ^{235}U/^{234}U ratio of ~87. Richter et al. (1999) suggested that the anomalous ^{235}U/^{234}U value was likely caused by anthropogenic contamination with Pu, especially ^{238}Pu which decays to ^{234}U ($t_{1/2} \approx 87.7$ a). Anthropogenic contamination is supported by the observation that the ore from Straz Pod Ralskem also contains unusually high levels of ^{236}U, ^{236}U/^{235}U ~3.5×10^{-6}. This isotope of U is most commonly produced by neutron capture on ^{235}U in nuclear reactors. If this interpretation is correct, the fact that very similar, low ^{235}U/^{234}U values are also observed in UOC from Straz Pod Ralskem implies that Pu contamination must be widespread in this area. If the elevated level of ^{236}U is also ascribed to anthropogenic Pu contamination, the ^{238}Pu/^{240}Pu can be estimated to be ~13.

2.5 DISCUSSION

2.5.1 Production of UOC

The production of UOC from uranium ore involves concentrating uranium from the relatively low levels (0.01 to 10 wt. %) found in ore at a specific mine to the >65 weight percent uranium in UOC sold on the commercial market. This study measures UOC and not uranium ore directly and assumes no significant isotope fractionation of ^{238}U from ^{235}U during the production of UOC.

Conventional uranium concentration is carried out by crushing and leaching ore, using either acidic or alkaline solutions. Recent work has shown that progressive leaching and incomplete dissolution of uranium ore does not cause measurable ^{238}U/^{235}U fractionation (Stirling et al. 2007; Bopp et al. 2009).

Because 90-95% of the uranium from ore is concentrated into UOC (Fernandez 1996), even if minor isotope fractionation occurs during conversion from ore to UOC, this effect would be negligible compared to the variations reported here based on the high uranium yield during the milling process. Moreover, the study of uranium isotopes in six uranium ores by Richter et al. (1999) contained two mines in common with this study of UOCs: the aforementioned Straz Pod Ralskem of the Czech Republic, and the Rössing mine of Namibia. The ^{238}U/^{235}U ratios from both ores and the respective UOCs from these mines agree within error, confirming that milling and concentration processes do not fractionate ^{238}U from ^{235}U at the combined level of precision of the two studies (<0.5‰). The ^{235}U/^{234}U ratios obtained from the Rössing mine also match within error, implying that this ratio is unfractionated during milling and concentration. Note, however, that the ^{235}U/^{234}U ratios from Straz Pod Ralskem do not agree within the stated errors. It is believed this difference is most plausibly attributed to sample heterogeneity.

2.5.2 Preferential leaching of isotopes

It has been known for decades that there is an increased amount of ^{234}U in groundwater and the oceans due to radioactive decay of ^{238}U to ^{234}U (via ^{234}Th and ^{234}Pa) and the subsequent alpha-recoil damage to the crystalline lattice of uranium-containing minerals that enables isotope-selective leaching to occur (Kigoshi 1971). Thus, percent-level ^{235}U/^{234}U variability in waters or weathered samples provides a clear indication of aqueous alteration. A positive correlation between $^{235}U/^{234}U$ and $^{238}U/^{235}U$ ratios in a sample suite would, therefore, be indicative of fractionation of ^{238}U from ^{235}U by aqueous alteration. In a prior study, Stirling et al. (2007) reported such a correlation for a variety of low-temperature, late-Quaternary age samples. Alternatively, the lack of correlation would suggest processes other than aqueous alteration are primarily responsible for fractionation of $^{238}U/^{235}U$. There is no evidence of a correlation between the measured $^{238}U/^{235}U$ and $^{235}U/^{234}U$ ratios in data of this study (Figure 2.4). This lack of correlation indicates that preferential leaching of ^{234}U and fractionation of $^{238}U/^{235}U$ in uranium ore bodies are not linked, and at least two distinct processes control the variations in $^{238}U/^{235}U$ and $^{235}U/^{234}U$ ratios.

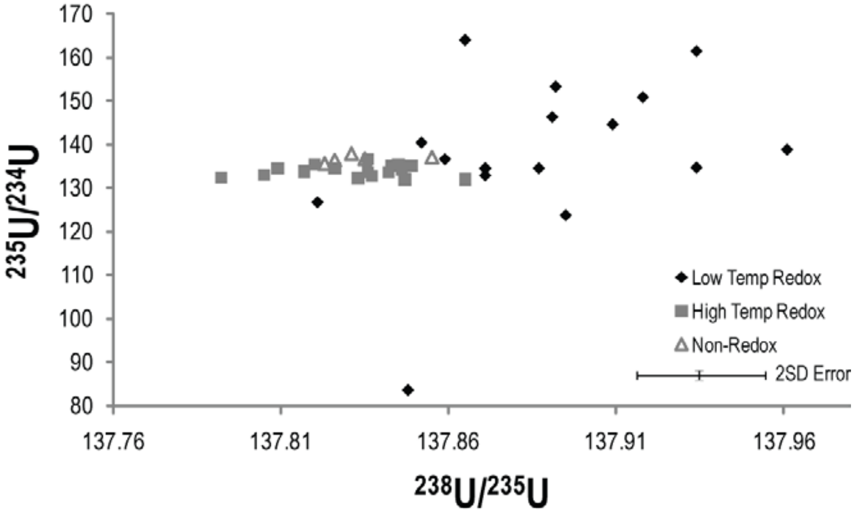

Fig. 2.4. $^{235}U/^{234}U$ and $^{238}U/^{235}U$ ratios for the 40 samples of this studied. All samples plotted together produce a correlation coefficient of 0.114; low-temperature redox samples plotted separately produce a correlation coefficient of

0.151. This lack of correlation suggests that ^{238}U, ^{235}U and ^{234}U are fractionated from one another by more than one mechanism.

The $^{235}U/^{234}U$ ratios of the high-temperature and non-redox deposits appear to lie close to the secular equilibrium value, whereas the $^{235}U/^{234}U$ ratios of the low-temperature deposits show significant scatter. This difference is likely related to the nature of the deposits themselves as open or closed systems. Low-temperature deposits primarily consist of sandstone or “roll front” deposits that form below the water table. The relatively high porosity of the host sandstone allows for greater open system behavior than does the more compacted lithology of the host rocks of high-temperature and non-redox deposits. Whenever large amounts of modern groundwater interact with a deposit, the deposit is expected to contain either 1) excesses of ^{234}U, if deposition is still occurring, or 2) depletions in ^{234}U if deposition has stopped.

2.5.3 Isotope fractionation via redox changes and the nuclear volume effect

Uranium commonly occurs in two oxidation states in terrestrial environments: U^{IV} and U^{VI}. The oxidized form of uranium, U^{VI}, is highly soluble under normal groundwater conditions and exists predominantly as $U^{VI}O_2^{+2}$ and $U^{VI}O_2OH^+$ or, when in the presence of carbonate, as a negatively charged carbonate complex (i.e., $U^{VI}O_2(CO_3)_3^{-4}$; Abdelouas et al. 1998). When reduced to U^{IV}, uranium becomes an essentially insoluble uranium oxide (generally, $U^{IV}O_2$). Thus, the reduction of U^{VI} to U^{IV} is a key step in the formation of many U-rich ore deposits. Although both high-temperature and low-temperature deposition of

U occurs, only the low-temperature samples exhibit significant fractionation in $^{238}U/^{235}U$. This difference suggests that temperature plays a significant role in the fractionation of U under redox conditions. It further suggests that the low-temperature redox transition ($U^{VI}O_2^{+2} \rightarrow U^{IV}O_2$) between the U^{VI} and U^{IV} valence states of uranium provides the primary mechanism in which $^{238}U/^{235}U$ fractionates.

It has been shown in thermodynamic calculations that the amount of $^{238}U/^{235}U$ nuclear-volume fractionation scales as a function of temperature (Abe et al. 2008). Equilibrium nuclear-volume isotopic fractionation factors should scale as $1/T$, rather than $1/T^2$ (Schauble 2007), and given the precision of this study, it is possible some of the scatter in the low-temperature deposits can be explained by variable temperatures of deposition. A thorough investigation of the temperature effects on the $^{238}U/^{235}U$ value of U ore requires a variety of individual uranium bearing minerals deposited at known temperatures.

The fractionation of $^{238}U/^{235}U$ results in the heavy isotope being preferentially concentrated into the reduced phase. Whereas this observation is consistent with work by Weyer et al. (2008) and Bopp et al. (2009), the fractionation direction is opposite that of the lighter elements in which the light isotope is concentrated in the reduced phase. Unlike lighter elements, in which isotopic fractionation occurs as a consequence of mass dependent differences in vibrational energies, the isotopes of uranium and other very heavy elements appear to be fractionated by a different process. Bigeleisen (1996) theorized that differences in the nuclear size and shape of individual uranium isotopes should lead to slightly different bonding environments for each isotope, based on the nuclear charge distribution and structure of the nuclear shell. The magnitude of this effect correlates with the nuclear volume of each isotope rather than strictly with mass, and is therefore referred to as the “nuclear volume effect” (or, alternatively, the “nuclear field shift”). As with mass dependent fractionation, the magnitude of the isotope shift decreases with increasing temperature. A thorough discussion of the nuclear volume effect is provided by Bigeleisen (1996) and Schauble (2007).

The consistently higher $^{238}U/^{235}U$ in the UOC of low-temperature deposits is evidence of low-temperature U isotope fractionation. However, in order for this low-temperature fractionation to be expressed, it is required that a large portion of the uranium passing through the system escaped and was not deposited in the primary ore body, as fully quantitative capture would cause no isotope fractionation to be expressed. It is possible that some of the scatter in the data from low-temperature ore deposit could be caused by variable amounts of U capture, where a higher percentage of capture reduces the effect of the fractionation, resulting in a lower $^{238}U/^{235}U$ value. Given ideal conditions in an undisturbed ore body, it would be theoretically possible to trace a distillation trend towards low $^{238}U/^{235}U$ as the ^{238}U is preferentially removed from solution through the reduction of U^{VI} to U^{IV}.

Fractionation of U by the nuclear volume effect is supported by two important observations in this study. First, for heavy elements like uranium, the magnitude of fractionation from this effect is expected to be large and potentially larger than for lighter elements. This makes U an ideal element in which to observe this effect. Second, this nuclear volume driven effect is unusual compared to traditional mass dependent isotope fractionation because it concentrates the heavier isotope in the reduced species during redox reactions. In lighter elements, like Mo, the light isotopes are in general preferentially partitioned into the reduced species, a function of the difference of the stiffness of the bonds. In the isotopes of extremely heavy elements, like U, the difference between the stiffness of the bonds is dominated by the volume of the isotope, not by the mass of the isotope. Thus, the direction and magnitude of U isotope fractionation that is observed is consistent with what is predicted on a theoretical basis for the nuclear volume effect (Schauble 2006), that there is a positive correlation between valence and the concentration of heavy isotopes of U.

2.5.4 Nuclear forensic applications of uranium isotope variations

Developing improved methods to identify or verify the sources of nuclear materials at the front end of the nuclear fuel cycle (e.g., yellowcake, uranium ore) is of great interest to the nuclear forensic community. Whereas isotopic systems such as Sr or Pb may help identify characteristics of the regional geology at the origin of the sample, the measurement of uranium isotopes has the potential to provide isotopic “fingerprints” of individual uranium mines (Richter et al. 1999). This stems from the fact that the three relatively abundant, long-lived isotopes of uranium exhibit decoupled variations of the respective isotope ratios, providing insight into distinct geologic and/or geochemical processes. By measuring the

^{238}U/^{235}U ratio, the type of the U-ore deposit (low-temperature redox deposit vs. high-temperature redox deposit/non-redox) can be determined. Measurement of the ^{235}U/^{234}U ratio with per mil precision in suites of samples containing percent-level variations has the potential to limit the possible source mines only to those that have very similar modern water/rock interactions, compared to the sample of interest, regardless of the depositional environment. The use of this signature is greatly aided by the fact that U is a major constituent of both UOC and U ores and is, therefore, easily separated and analyzed in these materials, and is difficult to contaminate. Thus multiple measurements at high signal intensities for both the ^{238}U/^{235}U and ^{235}U/^{234}U are possible and allow both isotope ratios to be determined with the highest possible precision. Although it is unlikely that any single isotope system will provide sufficient information to uniquely locate the source location of an interdicted UOC sample of unknown origin among the hundreds of currently and historically active uranium mines, the application of multiple isotopic systems will dramatically restrict the number of possible sources and prove invaluable in this endeavor.

2.5.5 Conclusions

The new U isotope data reported here support the suggestion that low-temperature redox changes are the major cause of fractionation between ^{238}U and ^{235}U. The direction and magnitude of the fractionation consistently follow the predictions of the nuclear volume effect associated with very heavy elements, and are opposite to the fractionation patterns of more well-studied, lighter elements (e.g., N, S, Fe). Variations in ^{234}U content are most plausibly explained by fluid mediated transport and are not correlated with ^{238}U/^{235}U fractionation, suggesting that preferential leaching from aqueous alteration does not play a major role in ^{238}U/^{235}U variability.

Chapter 3

URANIUM ISOTOPE FRACTIONATION DURING ADSORPTION TO MN-OXYHYDROXIDES

3.1 INTRODUCTION

With modern multi-collector ICP mass spectrometers, it is possible to resolve small isotopic variations for elements like U that were previously not known to undergo natural fractionation. It has been shown recently that variations of ~1.3‰ ($\delta^{238/235}$U, defined below) exist among natural Earth materials (Stirling et al. 2007; Weyer et al. 2008; Bopp et al. 2009). Much of this variation appears to be driven by isotope fractionation induced by redox changes (i.e., reduction of U^{6+} to U^{4+}) (Weyer et al. 2008; Bopp et al. 2009; Bopp et al. 2010; Brennecka et al. 2010; Montoya-Pino et al. 2010). However, significant isotopic variation was also reported between seawater and marine ferromanganese sediments. Uranium is likely hexavalent in seawater and at the surface of ferromanganese minerals (Weyer et al. 2008). Therefore the origin of this U isotope variation is not redox-driven fractionation.

It is well established that isotope fractionation between metals in seawater and ferromanganese sediments can occur during adsorption to mineral surfaces, driven by differences in metal coordination. Most notably, laboratory studies of the molybdenum isotope system have shown that significant isotope fractionation occurs during Mo adsorption onto Mn-oxyhydroxides (Barling et al. 2004; Wasylenki et al. 2008). The magnitude of this effect matches that seen in natural systems (Barling et al. 2001; Seibert et al. 2003). This fractionation results from a difference in the coordination environment of Mo between dissolved Mo and adsorbed Mo (Wasylenki et al. in review). Because adsorption to Mn-oxyhydroxides drives Mo isotopic fractionation, it is hypothesized that the fractionation of U isotopes observed by Weyer et al. (2008) between seawater and ferromanganese crusts could also be due to coordination change during adsorption. Like Mo, U occurs predominantly as anionic species in seawater, and thus will not readily adsorb as a weakly bound, outer-sphere complex, but must sorb as an inner-sphere complex. Inner-sphere adsorption often involves coordination change and is thus likely to cause isotope fractionation. If coordination change during adsorption is found to cause U isotope fractionation in this system, then it is possible that adsorption of U to many other materials will do likewise. Thus adsorption reactions in oxidizing zones of aquifers may cause a pattern of U isotope variation that could be useful for tracking the extent to which adsorption immobilizes this element in aquifers. This hypothesis is tested in batch adsorption experiments with synthetically produced birnessite (Mn oxyhydroxide) and U-bearing solutions.

In order to compare the coordination environment of U adsorbed to birnessite with that of dissolved U, one of the experimental samples was analyzed with extended X-ray absorption fine structure spectroscopy (EXAFS). EXAFS analysis provides information about the short-range coordination environment of the element of interest (U in this case), including the identity, number, and distance to neighboring atoms. In this study, comparison of the coordination environments of dissolved U and U adsorbed on birnessite sheds light on the molecular mechanism driving U isotope fractionation.

3.2 EXPERIMENTAL PROCEDURES

3.2.1 Experimental Setup

Batch adsorption experiments were conducted from solutions with two different U concentrations and over a range of experimental durations. These experiments were modeled after Mo isotope fractionation experiments (Barling et al. 2004; Wasylenki et al. 2008). Birnessite particles were synthesized by reducing $KMnO_4$ with HCl (Stroes-Gascoyne et al. 1987). As in previous studies, the birnessite, once filtered and washed, was kept in suspension, in this case in distilled, 18.2 MΩ-cm water. The U solution was prepared by diluting an ICP standard solution. The birnessite suspension and U stock solution were sparged for a few hours with a gas mixture of N_2 and 382 ppm CO_2 to facilitate equilibration with atmospheric CO_2 and to stabilize the weakly buffered solution. The *p*H of both solutions was adjusted to ~5 with HCl. To ensure enough U was present as both adsorbed U and dissolved U, a range of U/birnessite ratios was tested. The birnessite was mixed with solutions containing either 30 μM or 140 μM U (7.1 ppm or 33.3 ppm), which had an initial isotope composition of $^{238}U/^{235}U = 137.794 \pm 0.015$ ($\delta^{238/235}U \equiv 0.00 \pm 0.011$). Each 50 ml centrifuge tube of U solution with birnessite was agitated on a shaker table for periods of 0.17, 2, 10, 24 or 48 hours, after which the suspensions were filtered (0.2 μm) to halt the isotope exchange between dissolved and adsorbed U. The particles with adsorbed

U and solutions with remaining dissolved U were then processed separately; the U in each was extracted and purified by ion exchange chromatography, using Eichrom UTEVA resin and the elution procedure outlined in Weyer et al. (2008). Concentrations and isotope compositions of U were determined in both the dissolved and adsorbed U fractions.

3.2.2 Concentration Determinations

After separation of U from the sample matrix was completed, the U concentration of each sample was measured by quadrupole ICP-MS (Thermo X series). Typical uncertainties on these concentration measurements are <5% relative. Subsequently, a ^{236}U:^{233}U double spike was added to the sample, to correct for instrumental mass bias during measurement of the ^{238}U/^{235}U isotope ratio. In order to optimize spike/sample ratios, the samples were spiked after the concentrations of the samples were known rather than before purification. It has been shown that no measurable U isotope fractionation occurs during purification with the Eichrom UTEVA procedure (Weyer et al. 2008).

3.2.3 Isotope Ratio Measurements

Uranium isotope ratios were measured using a ^{236}U:^{233}U double-spike MC-ICP-MS procedure outlined in Weyer et al. (2008) to correct for instrumental mass bias. The double spike used (ASU in-house, Brennecka et al. 2010b) consists of a ~1:1 ratio of ^{236}U and ^{233}U and was calibrated against the accepted value for SRM950a (Richter et al. 2010). Extremely minor contributions of ^{235}U and ^{238}U were subtracted during data reduction ($^{236}U/^{233}U = 1.00496$; $^{238}U/^{233}U = 0.0009582$; $^{235}U/^{233}U = 0.0001084$). Samples in this study were spiked to achieve ^{236}U and ^{233}U signals of ~2.5 times the least abundant natural isotope of interest, ^{235}U. It has been shown that varying the amount of spike isotopes added within a range of ~2 to ~10 times has no measurable effect on the measured $^{238}U/^{235}U$ values of the samples (Weyer et al. 2008). Uranium isotope measurements were performed by MC-ICP-MS (on Thermo Scientific Neptune), using instruments at Arizona State University (ASU) and the University of Frankfurt. Samples were introduced with an Aridus desolvating nebulizer at the University of Frankfurt and with an Apex-Q sample introduction system at ASU. Uranium isotopes were measured simultaneously using Faraday collectors equipped with 10^{11} Ω resistors. Samples were dissolved in 0.32 M HNO_3 and measured at a concentration of ~120 ppb U (~0.5 μM) to obtain greater than 150 mV (1.5×10^9 milliamp) signals on ^{235}U. Data consistency was monitored by analyzing previously characterized U isotope standards every 3 to 4 samples during U isotope analyses at both laboratories (Weyer et al. 2008; Brennecka et al. 2010a; Brennecka et al. 2010b). All measurements at ASU and University of Frankfurt were identical with the analytical uncertainties (see Table 3.1). Results are expressed in δ notation, with R defined as the ratio measured:

$$\delta^{238/235}U = [R_{meas}/R_{std} - 1] \times 1000‰$$

$$\Delta^{238/235}U = \delta^{238/235}U_{(dissolved)} - \delta^{238/235}U_{(adsorbed)}$$

The standard was defined as the isotopic composition of the experimental stock solution.

3.2.4 EXAFS Measurements

In EXAFS analysis, monochromatic X-rays penetrate the sample and eject inner-shell electrons from the element of interest, causing outer-shell electrons to fill the vacancies and emit photoelectrons. The incoming X-ray energy is varied systematically from just below to just above the energy needed to eject electrons from a chosen shell, in this case the L_{III} edge of U. The absorption of X-rays by the sample depends upon how the photoelectrons scatter during interactions with neighboring atoms and is measured as a function of incident X-ray energy. The resulting absorption spectrum is then converted by Fourier transform to a radial distribution function. This function is then compared to the spectra of reference compounds and to the calculated spectra of various coordination models in order to constrain the coordination chemistry of the target element. Useful tutorials can be found by visiting http://xafs.org/tutorials.

A sample of U adsorbed on birnessite was prepared with the same methods described above for adsorption experiments, but with larger quantites of U stock solution and birnessite to produce enough material for EXAFS analysis. The U stock solution contained 50 µM U (11.9 ppm), and the solution and birnessite were separated by centrifugation so that the product was a moist paste. Allowing the sample to dry was avoided to prevent birnessite from recrystallizing into other Mn oxyhydroxides. Within three days, the birnessite with adsorbed U was loaded as a wet paste into a 1 mm thick polycarbonate sample holder and sealed with polycarbonate windows and Kapton tape. Analysis was performed on

Beamline 4-1 at the Stanford Synchrotron Radiation Laboratory, using a Lytle detector and a silicon (220) double crystal monochromator. The U L_{III} edge was calibrated at 17166 eV by measuring the edge of Y foil. Ta slits were set at 2 mm x 20 mm, and a Sr filter was used to reject elastic scattering. Six scans were collected for incident energies of 17025 to 17851 eV (up to $k = 13$ Å^{-1}). Using SIXPACK software (Webb et al. 2005), the scans were averaged, the background subtracted, fit the spline, and the resulting spectrum was fit using phase and amplitude files from FEFF8.40 (Ankudinov et al. 1998).

3.3 RESULTS

3.3.1 Concentration Results

The approach to steady state (both concentration and isotopic) appears to occur rapidly, in ≤ 2 hours for experiments at both initial U concentrations. Approximately 80% of the total U was adsorbed to the birnessite in the 30 μM experiment, while approximately 40% was adsorbed to the birnessite in the 140 μM experiment (Figure 3.1). In all cases, the sum of the measured U in solution and measured U adsorbed represented >95% of the U added to the experiment.

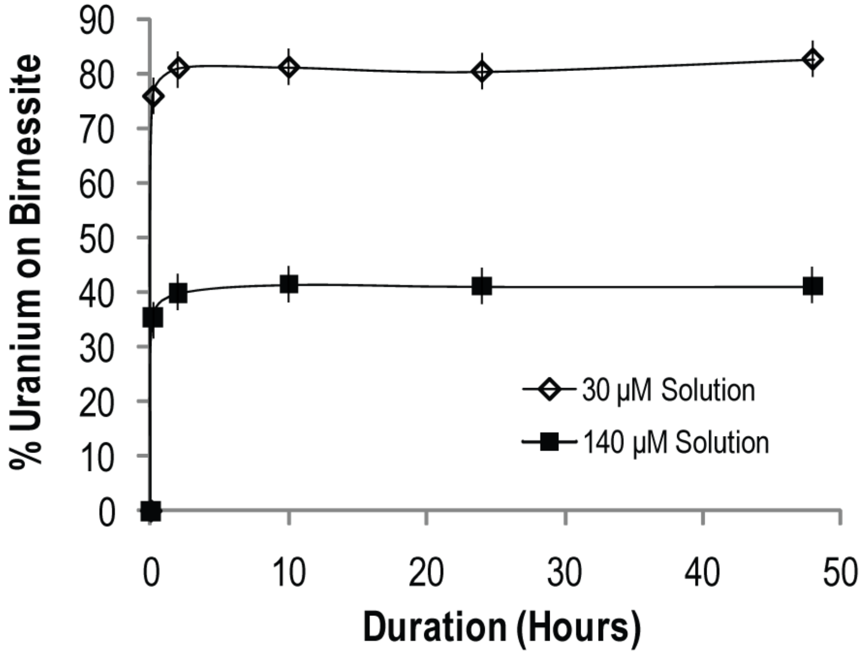

Fig. 3.1. Fraction of U adsorbed in two experiments as a function of time. The U concentration in the stock solution was 30 μM for one set of experiments (open diamond symbols) and 140 μM for the second (black square symbols).

3.3.2 Isotopic Results

Uranium isotope compositions were similar in all experiments; U adsorbed to the birnessite is isotopically lighter by 0.22±0.09‰ ($\delta^{238/235}$U, 2SD of all δ-values) compared to U in the filtrate (Table 3.1, Figure 3.2). Isotopic mass balance is satisfied within the uncertainties for all experiments.

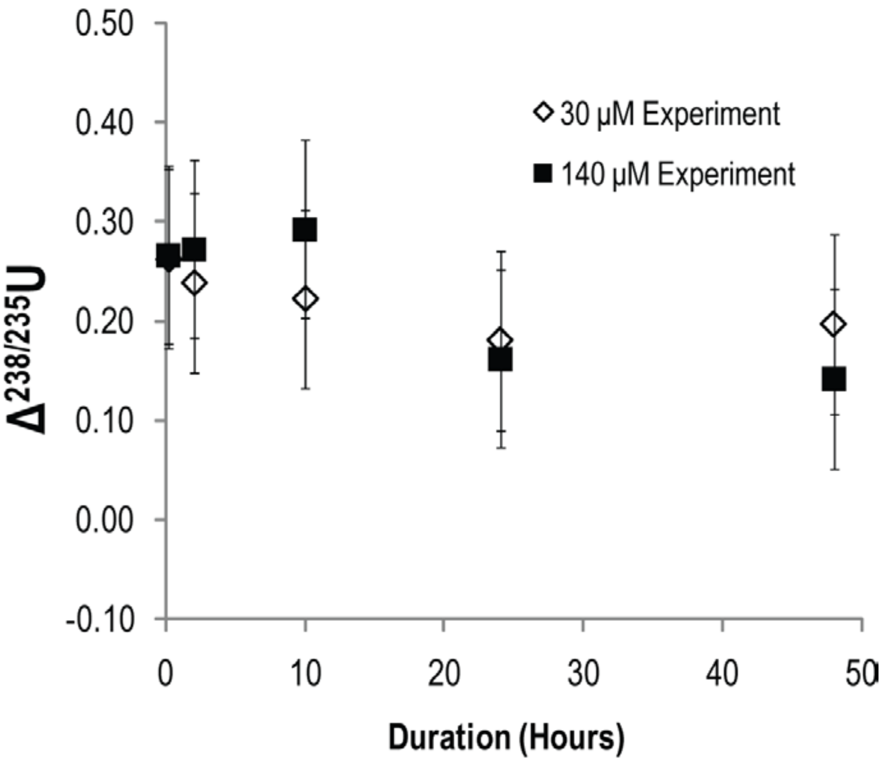

Fig. 3.2. Magnitude and direction of isotope fractionation between birnessite and 30 μM and 140 μM experimental stock solutions. Big delta (Δ) denotes the difference between the small delta (δ) values of the dissolved and adsorbed uranium (formulas shown above). Uncertainties are shown as the 2SD of the population of all Δ-values for all experiments. For figure clarity, plotted data are only that collected at ASU.

Table 3.1. Uranium isotopic data from the two experiments.

	ASU Measurements 30 µM Experiment			**Frankfurt Measurements 30 µM Experiment**			**ASU Measurements 140 µM Experiment**		
	$^{238}U/^{235}U$	$\delta^{238/235}U$	$\Delta^{238/235}U$	$^{238}U/^{235}U$	$\delta^{238/235}U$	$\Delta^{238/235}U$	$^{238}U/^{235}U$	$\delta^{238/235}U$	$\Delta^{238/235}U$
10 Min Filtrate	137.821	0.24	0.26	137.819	0.27	0.27	137.806	0.16	0.27
10 Min Birnessite	137.785	-0.02		137.781	-0.01		137.769	-0.10	
2 Hr Filtrate	137.822	0.25	0.24	137.824	0.30	0.20	137.811	0.17	0.27
2 Hr Birnessite	137.789	0.01		137.797	0.10		137.773	-0.11	
10 Hr Filtrate	137.820	0.26	0.22	137.825	0.24	0.23	137.802	0.10	0.29
10 Hr Birnessite	137.789	0.04		137.793	0.01		137.762	-0.19	
24 Hr Filtrate	137.812	0.20	0.18	137.813	0.13	0.17	137.800	0.10	0.16
24 Hr Birnessite	137.787	0.02		137.791	-0.04		137.778	-0.06	
48 Hr Filtrate	137.824	0.30	0.20	137.822	0.21	0.22	137.798	0.09	0.14
48 Hr Birnessite	137.797	0.10		137.791	-0.02		137.778	-0.06	
Stock Ave.	**137.787**	**≡0.00**		**137.791**	**≡0.00**		**137.787**	**≡0.00**	
2SD* Error	**0.015**			**0.008**			**0.015**		

*2SD is calculated as 2 × the standard deviation of multiple measurements of the stock solution during that analytical session.

3.3.3 EXAFS results

The spectra for two aqueous species (with fits) and the U-on-birnessite sample are shown in Figures 3.3 and 3.4. Figure 3.3 shows the EXAFS spectrum after the atomic absorption background is subtracted, the energies are converted to units of $Å^{-1}$ (*k*-space), and the spectrum is weighted by k^3 to enhance the small variations at high values of *k*. Figure 3.4 shows the same data after a Fourier transform is applied to generate a radial distribution function, as Fourier transform magnitude vs distance to scattering neighbor atoms (R+ΔR), where R+ΔR has not been corrected for phase shift. Below these spectra are plotted the arithmetic differences between each aqueous species spectrum and the spectrum of the adsorbed U on birnessite. The significance of these difference spectra is discussed below. The raw absorption spectrum for the adsorption sample shows the U L_{III} absorption edge at 17170 eV.

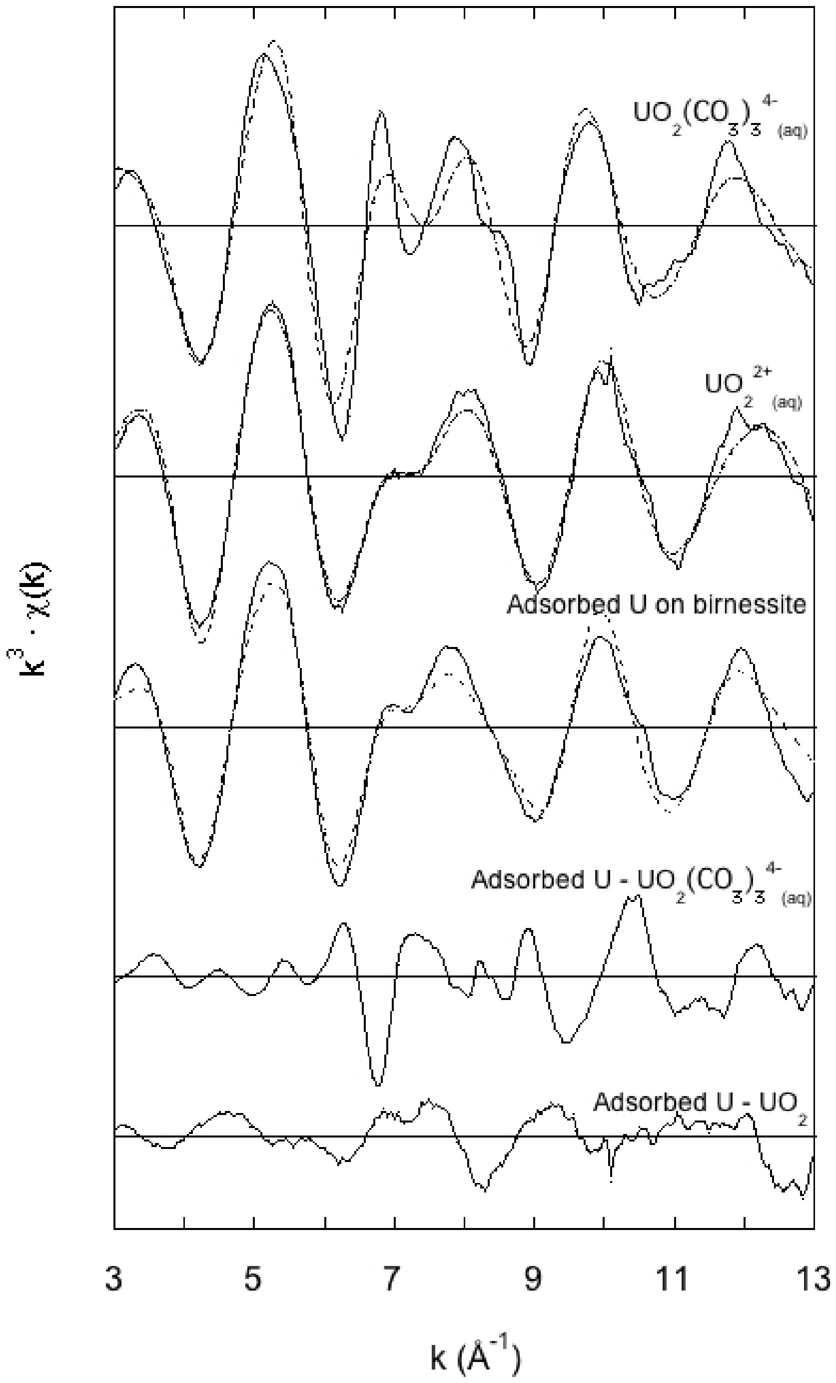

Fig. 3.3. EXAFS spectra for aqueous U species and an experimental sample of U adsorbed on birnessite, shown as k^3-weighted EXAFS vs k. The differences between each aqueous species and the U-on-birnessite sample are also shown. Solid lines are data; dashed lines are best fits, as tabulated in Table 3.2.

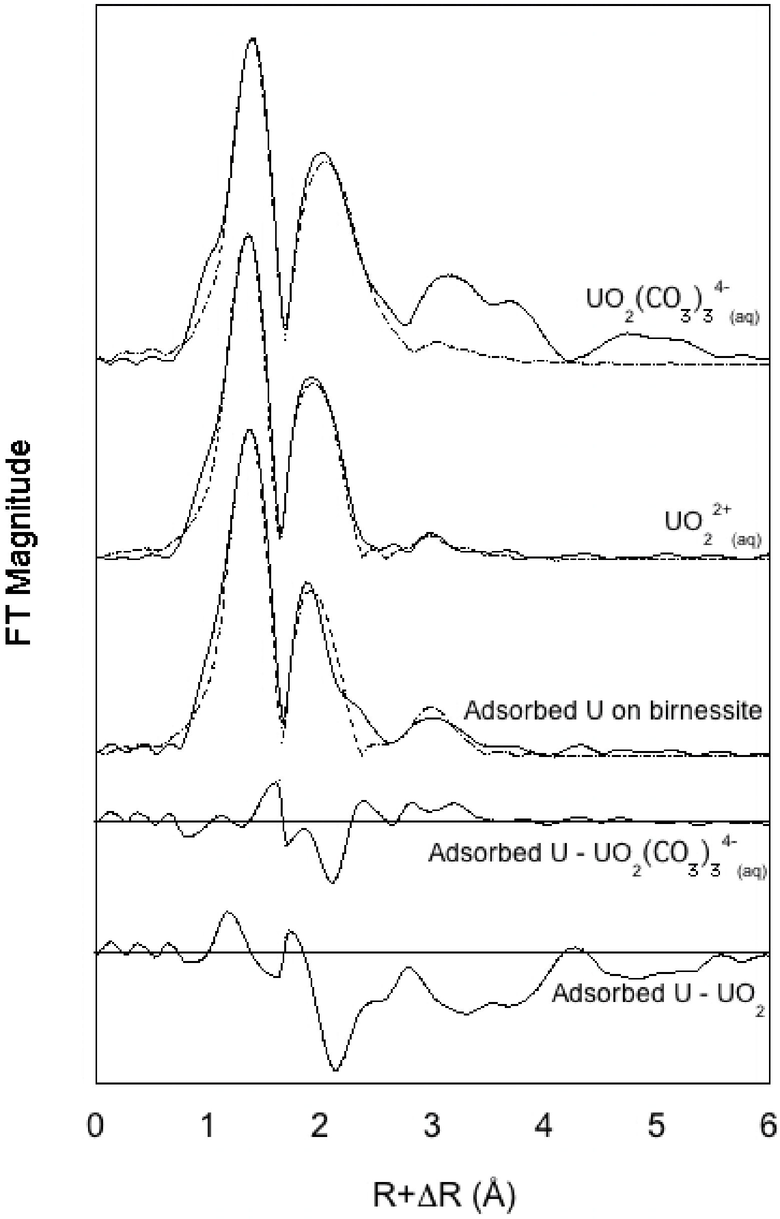

Fig. 3.4. EXAFS spectra for aqueous U species and an experimental sample of U adsorbed on birnessite, shown in Fourier transform space, without correction of distances for the phase shift. The unfit amplitude above R+ΔR = 2.8 Å in the uranyl triscarbonato complex is due to several multiple scattering paths (Bargar et al. 2000), which was not modeled here, since the objective was to examine

oxygen atoms within 3 Å of U absorbers. Differences between the Fourier transform of the adsorbed U spectrum and the two aqueous species are also shown. Solid lines are data; dashed lines are best fits.

Table 3.2. EXAFS fitting results

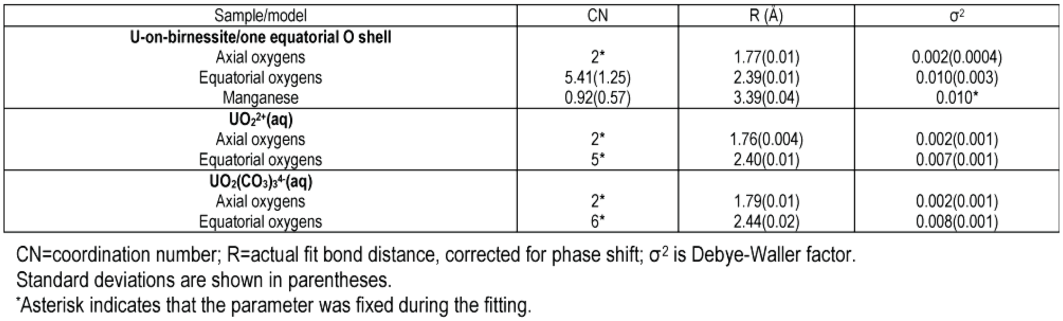

Sample/model	CN	R (Å)	σ^2
U-on-birnessite/one equatorial O shell			
Axial oxygens	2*	1.77(0.01)	0.002(0.0004)
Equatorial oxygens	5.41(1.25)	2.39(0.01)	0.010(0.003)
Manganese	0.92(0.57)	3.39(0.04)	0.010*
UO_2^{2+}(aq)			
Axial oxygens	2*	1.76(0.004)	0.002(0.001)
Equatorial oxygens	5*	2.40(0.01)	0.007(0.001)
$UO_2(CO_3)_3^{4-}$(aq)			
Axial oxygens	2*	1.79(0.01)	0.002(0.001)
Equatorial oxygens	6*	2.44(0.02)	0.008(0.001)

CN=coordination number; R=actual fit bond distance, corrected for phase shift; σ^2 is Debye-Waller factor.
Standard deviations are shown in parentheses.
*Asterisk indicates that the parameter was fixed during the fitting.

3.4 DISCUSSION

3.4.1 Fractionation mechanisms of isotopes of heavy elements

In general, equilibrium isotope effects occur when an element partitions between two or more possible species or sites that have different vibrational bond energies. The isotopes will partition among the possible sites such that the vibrational bond energy of the entire system is minimized (Urey 1947). Often the species or sites available differ in the redox state of the element of interest or in the identity and configuration of the neighboring atoms, and the masses of the isotopes affect the bond vibrational energies and thus govern equilibrium partitioning. However, for the heaviest elements, fractionations are not primarily driven by mass-dependent differences in bond vibrational frequencies. For very heavy elements, the nuclei are of sufficient size to influence the distribution of electrons (Bigeleisen 1996). The result is that the distributions of electrons in bonds formed by heavy and light isotopes vary slightly due to the difference in number of neutrons. The magnitude of this effect correlates with the nuclear volume of the isotope rather than strictly with mass, and is therefore referred to as the "nuclear volume effect." A thorough discussion of the nuclear volume effect and its increased importance for very heavy nuclei is provided by Bigeleisen (1996) and Schauble (2007).

3.4.2 An equilibrium isotope effect matching that observed in nature

Results from this experimental study show that adsorption of U to birnessite causes fractionation of ~0.2‰ in δ^{238}U (lighter isotope preferentially adsorbed). The fractionation is constant with time within error, implying an equilibrium isotope effect. If this fractionation were due to a kinetic isotope effect, in which a slightly faster rate of reaction for the light isotope leads to an isotopically light product, then the magnitude of fractionation observed would depend on the duration of the experiment. The sense and magnitude of the fractionation observed in these experiments is the same as that reported between seawater and ferromanganese sediments by Weyer et al. (2008). Because the *p*H of these experiments and therefore the most abundant species of dissolved U differ from the marine environment, it is possible that the two fractionations match by coincidence. But it may also be that the two effects are driven by a common mechanism, as discussed below.

3.4.3 Coordination of U adsorbed to birnessite differs from that in aqueous U species

In these experiments, U is introduced as U(VI). The experiment takes place in oxidizing conditions in the presence of birnessite, a strong oxidant on its own. Thus it is expected that all U remained in the oxidized, hexavalent state in this system. Reduction to U(IV) would have been evident as a shift of the absorption edge in the spectra to lower energy values. The U(VI) reference compound edge was at 17167 eV and the sample's adsorption edge was at 17170 eV, which is consistent with 100% U(VI) in the adsorption sample (Bertsch et al. 1994). Since there is no evidence of a redox change, the $^{238}U/^{235}U$ fractionation reported here is most likely the result of a difference in the coordination environment of U between the most abundant dissolved species and the dominant adsorbed species.

In seawater, U occurs predominantly as the hexavalent uranyl triscarbonato complex, ($UO_2(CO_3)_3^{-4}$), but $UO_2(CO_3)_2^{-2}$ is also abundant (Ku et al. 1977; Waite et al. 1994; Swarzinski et al. 1999; McManus et al. 2006; refs therein). At lower pH values, such as in this adsorption experiment and some groundwaters (*p*H ~5), other species become more important, including $UO_2(CO_3)_2^{2-}$, $(UO_2)_2CO_3(OH)_3^{-}$, $UO_2(OH)^{+}$, and especially UO_2^{2+}. All of these species involve multiply-bonded axial oxygens atoms at distances of 1.75-1.80 Å and varying numbers of equatorial oxygens. Only $UO_2(CO_3)_3^{-4}$ and UO_2^{2+} can be easily isolated in solution by manipulating *p*H; hence EXAFS spectra were collected for these two species, as shown in Figures 3.3 and 3.4. The overall resemblance between the spectra for the two dissolved species and this spectrum of U adsorbed to birnessite is obvious. Therefore, subtle differences in the arrangement of coordinating atoms that might explain the observed isotope effect. To expose such differences, the spectra of $UO_2(CO_3)_3^{-4}$ and UO_2^{2+} is arithmetically subtracted from this adsorbed sample spectrum. The differences are shown at the bottom of Figures 3.3 and 3.4. There is no normalization or change in scale applied, and yet the amplitudes of the difference spectra exceed one half of the amplitudes of the spectra themselves in some places. Therefore these differences cannot be attributed to analytical uncertainties or noise. These experiments were conducted at *p*H ~5, so the most relevant comparison is between UO_2^{2+} and the adsorbed sample. The presence of significant differences in both the EXAFS and Fourier transform plots confirms that coordination of U in the sample of this study is indeed distinct from that in UO_2^{2+}, supporting the hypothesis that a difference in coordination geometry between dissolved and adsorbed U drives the observed isotope effect in these experiments.

It is very possible that the specific coordination change that occurs when UO_2^{++} adsorbs to birnessite differs from the specific coordination change when $UO_2(CO_3)_3^{-4}$ adsorbs to birnessite. However, the dissolved species both in the experiments and in seawater have symmetrical arrangements of equatorial oxygens. Waite et al. (1994), Bargar et al. (2000), and Catalano and Brown (2005) reported a loss of symmetry of equatorial oxygens surrounding U compared to aqueous U when adsorbed to ferrihydrite, hematite, and montmorillonite, respectively. To explore whether similar splitting of equatorial oxygens into two groups, or subshells, with slightly different U-O distances occurs in the adsorbed complex of U on birnessite, it is attempted to fit the adsorbed EXAFS spectrum first with a single, symmetric shell of equatorial oxygens and then with two subshells. Although the fit with two subshells of equatorial oxygens is slightly better in terms of goodness-of-fit (the R factor, as defined by Hamilton 1965), the uncertainties in the U-O distances, coordination numbers, and Debye-Waller factors (a fit variable associated with scattering attenuation due to thermal motion of the atoms) were larger. In addition, the two equatorial shell distances (2.36 and 2.49 Å), while in good agreement with the distances reported in Waite et al. (1994), Bargar et al. (2000), and Catalano and Brown (2005), are too close together to be properly resolved with the current data set. Given the density of this data set (collected from $k = 3$ to 13), the minimum distance between shells that is resolveable in these fits is given by the Nyquist criterion: minimum resolvable distance = $\Delta r = \pi/(2\Delta k) = 0.16$ Å. While a disordered set of equatorial oxygens is certainly possible in the adsorbed complex, it cannot be concluded here that it is a better model for the adsorbed complex than a symmetric shell of equatorial oxygens, and it is not included it in the figures. Future studies of U adsorbed on birnessite should aim for larger EXAFS data sets such that these two models may be properly distinguished. In addition, the hypothesis that splitting of the equatorial oxygens around U can drive equilibrium isotope fractionation between dissolved and adsorbed U can be tested experimentally for U adsorbed to ferrihydrite, hematite, and montmorillonite, since split shells have been previously demonstrated for those substrates. If a similar change in coordination environment for U occurs, one would expect similar U isotope behavior, i.e., adsorption of isotopically light U, with a magnitude of fractionation near 0.2‰.

3.4.4 A common mechanism of adsorption and fractionation?

These experiments demonstrate that isotopic fractionation occurs between dissolved UO_2^{2+} and adsorbed U on birnessite from slightly acidic solution. It was also shown that there is a subtle U coordination difference between the dissolved and adsorbed species, which likely governs the observed isotope effect. There was no direct comparison between the predominant aqueous U species in seawater (likely $UO_2(CO_3)_3^{4-}$ or $Ca_2UO_2(CO_3)_3$) and the adsorbed complex on natural ferromanganese oxides, which is as yet unidentified. The agreement in direction and magnitude of fractionation in these experiments and between seawater and ferromanganese sediments, however, suggests that the mechanism causing isotope fractionation (i.e., a shift in bond distances and in the distribution function of bond distances for nearest neighbor oxygens) in both the experimental system and the marine system may be the same.

3.4.5 Applications of $^{238}U/^{235}U$ variability

As demonstrated in Bopp et al. (2010), U migration from contaminated aquifers can be tracked using the $^{238}U/^{235}U$ ratio in groundwaters. Their approach utilizes the ~1‰ difference ($\delta^{238/235}U$) caused by the reduction of U(VI) to U(IV). This work indicates that U isotopes also fractionate during adsorption, the other major process that immobilizes U. It may be possible in future work to track the effects of adsorption reactions on migration of U in groundwater in oxidizing aquifers, especially if U turns out to fractionate with similar magnitude during adsorption to other abundant substrates, such as Fe oxyhydroxides. In this case, a progressive depletion in ^{235}U would be measurable in U contaminated groundwater interacting with manganese and iron oxyhydroxides. Future adsorption experiments are needed to determine U isotope fractionation during adsorption for a variety of groundwater conditions and on a variety of different minerals for this application to be realized.

The development of ^{238}U/^{235}U in marine sediments as a paleoredox proxy would represent a major advance, complementing existing paleoredox proxies. If there is a consistent equilibrium U isotope offset between seawater and natural, hydrogenetic ferromanganese sediments, then ancient sediments could be used to establish the ^{238}U/^{235}U of ancient seawater. Because reduction and removal of U from anoxic waters is associated with a large fractionation (1‰, heavier isotope preferentially removed), the U isotope composition of ancient seawater can be expected to reflect the extent to which U was removed by reduction over time (Montoya-Pino et al. 2010).

Chapter 4

RAPID EXPANSION OF OCEANIC ANOXIA IMMEDIATELY BEFORE THE END-PERMIAN MASS EXTINCTION

4.1 INTRODUCTION

The end-Permian extinction represents the largest mass extinction in Earth history, with the demise of an estimated 90% of all marine species (Stanley 2007). While it has been extensively studied, the exact nature and cause of the end-Permian extinction remains the subject of intense scientific debate. Proposed kill mechanisms have included a nearby supernova, bolide impacts, periods of extreme volcanism (e.g., Siberian traps), extensive glaciation, and widespread ocean anoxia (Erwin et al. 2002). Evidence for shallow ocean anoxia in conjunction with the end-Permian mass extinction is widespread (Bond and Wignall 2005; Grice et al. 2005; Cao et al. 2009), but the intensity and timing of oceanic redox changes remain uncertain (Algeo et al. 2010a; Isozaki 1997; Algeo et al. 2011; Ehrenberg et al. 2008). Recent hypotheses invoke thet release of hydrogen sulfide gas (H_2S) as a kill mechanism (Kump et al. 2005, Meyer et al. 2008; Riccardi et al. 2007). Such models call upon strong expansion of oceanic anoxia below the oxygenated surface layer to allow buildup of H_2S, followed by an upward excursion of the chemocline that releases the poisonous gas into the atmosphere (Riccardi et al. 2007). In this study, the $^{238}U/^{235}U$ and Th/U ratios in a carbonate section spanning the end-Permian extinction horizon (EH) is examined to test this hypothesis. Samples for this study were collected from the Dawen section of the Yangtze Block in southern China (Fig. 4.1), which was has been correlated with the global stratotype section and point (GSSP) of the Permian–Triassic boundary at Meishan (Chen et al. 2009).

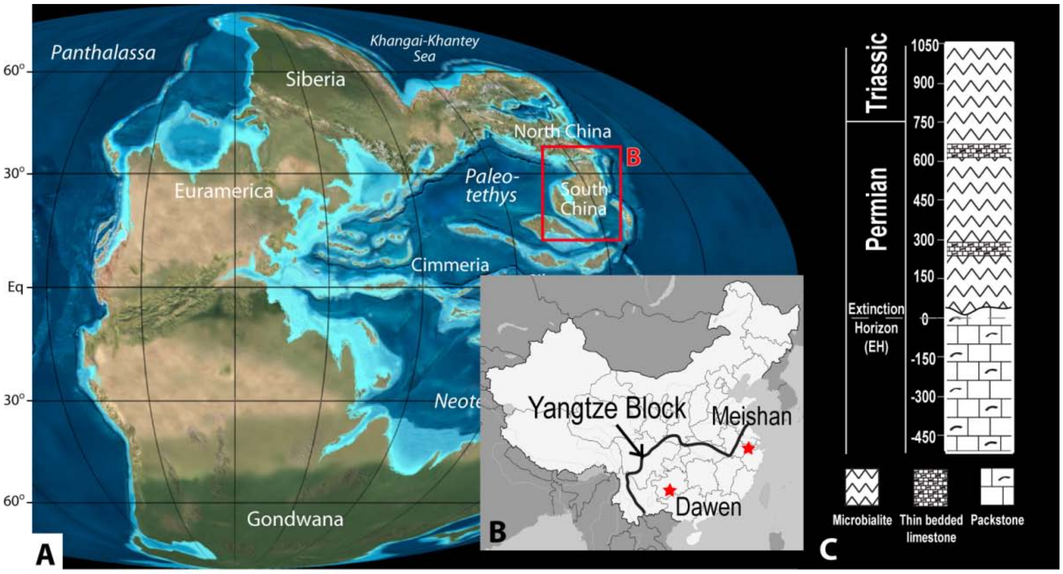

Fig. 4.1. Location of South China at ~252 Ma, the time of the end-Permian extinction (Fig. 4.1A, modified base map from R. Blakey (http://jan.ucc.nau.edu/~rcb7/260moll.jpg)) and present-day location of the Dawen section (Fig. 4.1B, modified from Chen et al., 2009). The location of the Meishan GSSP is shown for reference. Lithostratigraphy of the Dawen section is shown in Fig. 4.1C; see Chen et al. (2009) for its correlation to the Meishan GSSP.

4.2 BACKGROUND

Due to the geochemical properties of uranium (U), the ratio of $^{238}U/^{235}U$ can be used as a tool to investigate the history of ocean oxygenation. The long residence time (~500 kyr) of U in the oceans leads to a homogeneous U concentration in seawater (Klinkhammer and Palmer 1991; Ku et al. 1977), as well as to a homogenous U isotopic composition (Delanghe et al. 2002; Stirling et al. 2007; Weyer et al. 2008). The low-temperature redox transition (U^{6+} to U^{4+}) of U is the primary cause of $^{238}U/^{235}U$ fractionation on Earth, with the reduced species preferentially enriched in ^{238}U (Stirling et al. 2007; Weyer et al. 2008; Bopp et al. 2009; Brennecka et al. 2010). During times of oceanic anoxia, the flux of reduced U to anoxic facies (such as black shales) increases, preferentially removing ^{238}U from seawater. The loss of isotopically heavy U drives seawater to lighter isotopic compositions (Montoya-Pino et al. 2010). Changes in the U isotope ratios of organic-rich sediments have been used to study oceanic redox conditions during the Cretaceous (Montoya-Pino et al. 2010). Here, this isotope system is applied to Late Permian and Early Triassic carbonate rocks. Existing evidence indicates that carbonates record the $^{238}U/^{235}U$ ratio of the seawater in which they were deposited (Stirling et al. 2007; Weyer et al. 2008), suggesting that ancient carbonates that retain a primary signal of U isotopes may be used to estimate relative changes in ocean oxygenation.

4.3 RESULTS AND DISCUSSION

4.3.1 Uranium Isotopic Ratio Change Over the Extinction Horizon

In the Dawen section, the average U isotopic composition of samples deposited prior to the EH ($\delta^{238}U$ = -0.37‰) is very close to that of modern seawater ($\delta^{238}U$ = -0.41±0.03‰,(Weyer et al. 2008)). This observation suggests that the fraction of U removed to reducing sinks during the late Permian was similar to that of the modern ocean. The Dawen section exhibits an abrupt and significant change in δ^{238}U at the EH (Fig. 4.2 and Table 4.1) to values averaging -0.65‰. The δ^{238}U ratios of pre- and post-EH samples are significantly different (*p*<0.0001; two-tailed student's t-test with a significance level of α=0.01). A few isotopically light samples are present below the EH (-118 and -97 cm), which may provide evidence of brief episodes of transient intensification of oceanic anoxia preceding the end-Permian mass extinction. This inference is supported by evidence from additional geochemical proxies in other studies (Algeo et al. 2010a) (see further in Section 4.4 discussion).

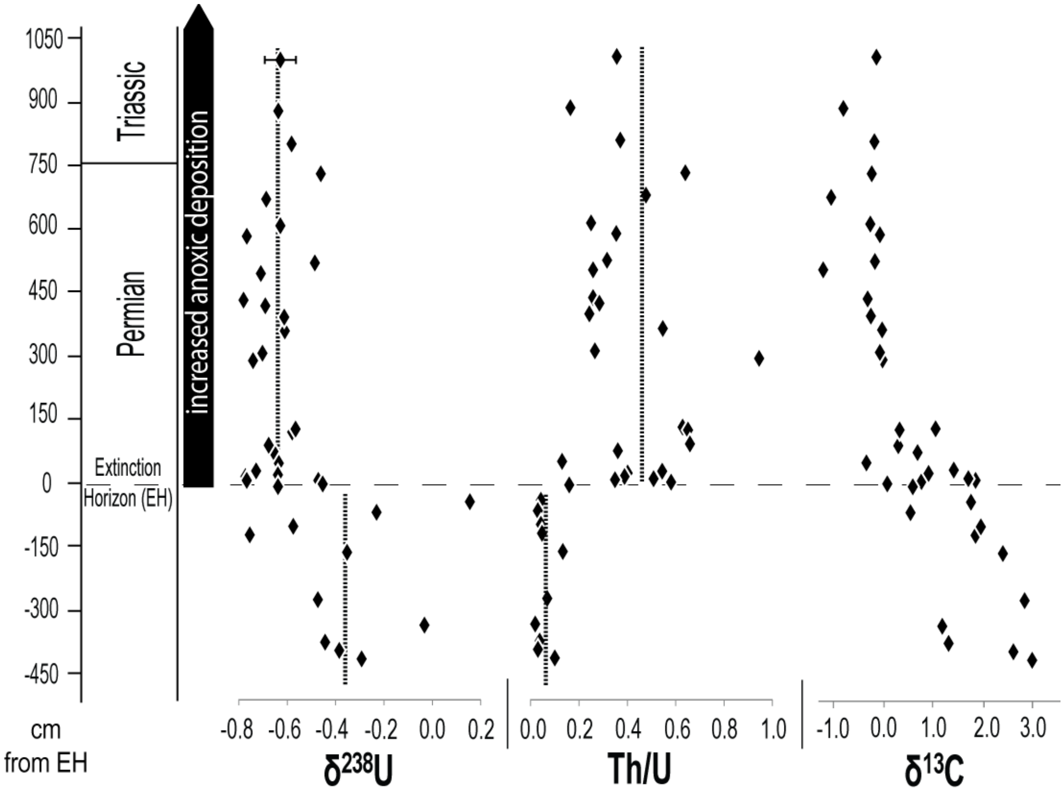

Fig. 4.2. Geochemical profiles for the Dawen section. The vertical dashed lines represent average values of δ^{238}U and Th/U for pre-EH and post-EH samples. The ^{238}U/^{235}U ratios are reported using standard δ-notation, where δ^{238}U = [Ratio$_{meas}$/Ratio$_{std\ (SRM950a)}$ - 1] ×1000. Average 2SD uncertainty of δ^{238}U values is shown on the top data point only for clarity. δ^{13}C, and age data from Chen et al. (2009).

Table 4.1. Data table showing sample number, represented by distance from the EH in cm, δ^{238}U (in ‰) with associated uncertainty (2SD) and number of runs (N), Th/U, U/Al, and %Dolomite in samples of this study. The δ^{13}C values from Chen et al. (2009) are included for reference. "N", the number of runs, refers to the times the sample was run for U isotopes. Multiple samples were run as replicates for quality control from powder, and these replicates are included in "N" as the same sample.

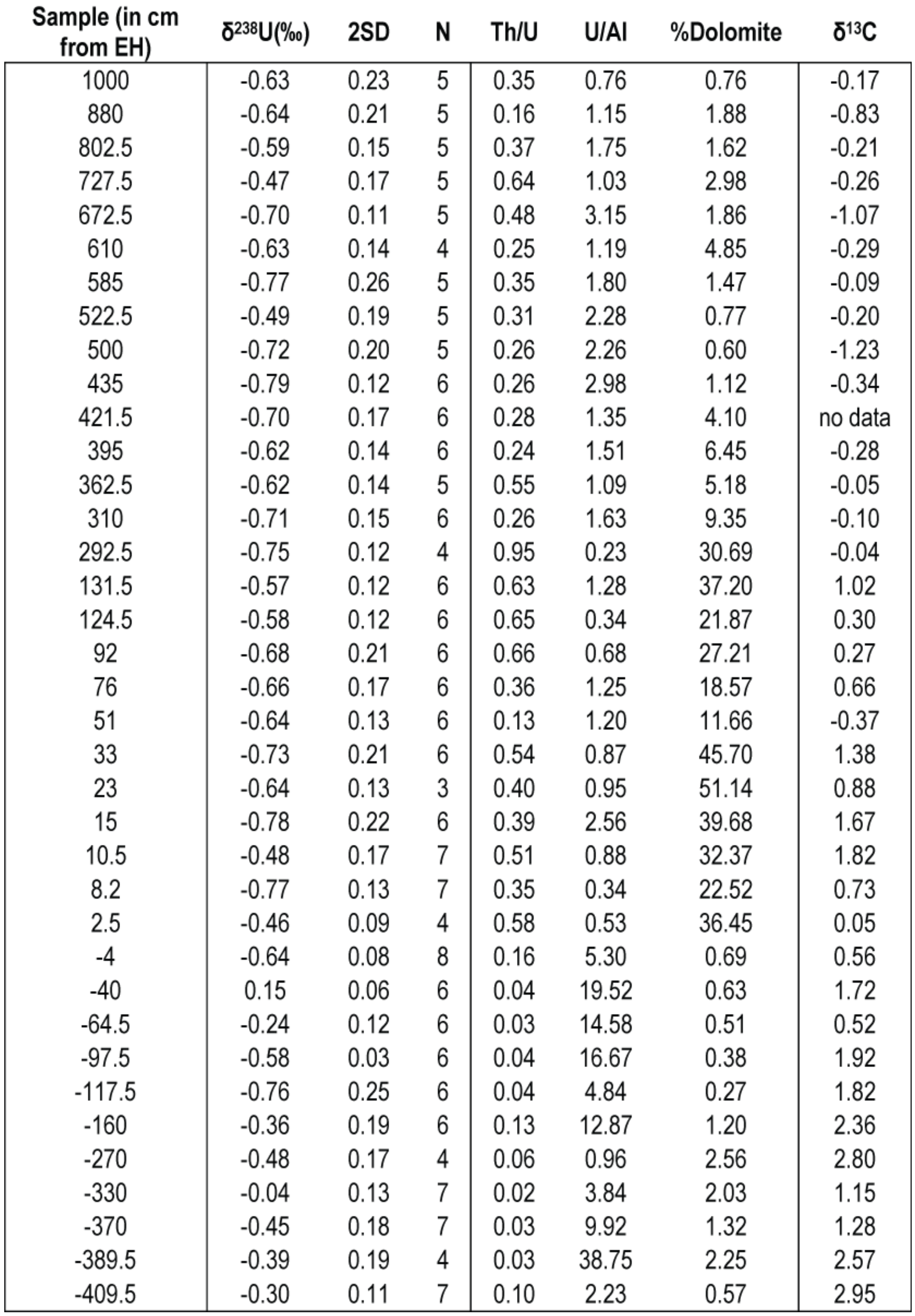

Sample (in cm from EH)	δ238U(‰)	2SD	N	Th/U	U/Al	%Dolomite	δ13C
1000	-0.63	0.23	5	0.35	0.76	0.76	-0.17
880	-0.64	0.21	5	0.16	1.15	1.88	-0.83
802.5	-0.59	0.15	5	0.37	1.75	1.62	-0.21
727.5	-0.47	0.17	5	0.64	1.03	2.98	-0.26
672.5	-0.70	0.11	5	0.48	3.15	1.86	-1.07
610	-0.63	0.14	4	0.25	1.19	4.85	-0.29
585	-0.77	0.26	5	0.35	1.80	1.47	-0.09
522.5	-0.49	0.19	5	0.31	2.28	0.77	-0.20
500	-0.72	0.20	5	0.26	2.26	0.60	-1.23
435	-0.79	0.12	6	0.26	2.98	1.12	-0.34
421.5	-0.70	0.17	6	0.28	1.35	4.10	no data
395	-0.62	0.14	6	0.24	1.51	6.45	-0.28
362.5	-0.62	0.14	5	0.55	1.09	5.18	-0.05
310	-0.71	0.15	6	0.26	1.63	9.35	-0.10
292.5	-0.75	0.12	4	0.95	0.23	30.69	-0.04
131.5	-0.57	0.12	6	0.63	1.28	37.20	1.02
124.5	-0.58	0.12	6	0.65	0.34	21.87	0.30
92	-0.68	0.21	6	0.66	0.68	27.21	0.27
76	-0.66	0.17	6	0.36	1.25	18.57	0.66
51	-0.64	0.13	6	0.13	1.20	11.66	-0.37
33	-0.73	0.21	6	0.54	0.87	45.70	1.38
23	-0.64	0.13	3	0.40	0.95	51.14	0.88
15	-0.78	0.22	6	0.39	2.56	39.68	1.67
10.5	-0.48	0.17	7	0.51	0.88	32.37	1.82
8.2	-0.77	0.13	7	0.35	0.34	22.52	0.73
2.5	-0.46	0.09	4	0.58	0.53	36.45	0.05
-4	-0.64	0.08	8	0.16	5.30	0.69	0.56
-40	0.15	0.06	6	0.04	19.52	0.63	1.72
-64.5	-0.24	0.12	6	0.03	14.58	0.51	0.52
-97.5	-0.58	0.03	6	0.04	16.67	0.38	1.92
-117.5	-0.76	0.25	6	0.04	4.84	0.27	1.82
-160	-0.36	0.19	6	0.13	12.87	1.20	2.36
-270	-0.48	0.17	4	0.06	0.96	2.56	2.80
-330	-0.04	0.13	7	0.02	3.84	2.03	1.15
-370	-0.45	0.18	7	0.03	9.92	1.32	1.28
-389.5	-0.39	0.19	4	0.03	38.75	2.25	2.57
-409.5	-0.30	0.11	7	0.10	2.23	0.57	2.95

4.3.2 Quantifying Increased Anoxic Deposition

The shift toward lighter U isotopic compositions after the extinction event is consistent with an increase in the deposition of isotopically heavy U in anoxic facies. The isotopic composition of U in seawater is ultimately controlled by the relative sizes and isotopic signatures of the major sources and sinks of U to the ocean. A simple box model of the oceanic U budget for the modern and end-Permian oceans is shown in Figure 4.3. Invoking mass balance, the approximate increase in anoxic sedimentation in the end-Permian ocean is calculated as:

$$\boldsymbol{\delta^{238}U_{input} = ((1-f_{anoxic}) \times \delta^{238}U_{other}) + (f_{anoxic} \times \delta^{238}U_{anoxic})} \qquad \textbf{Eq. 1}$$

Here, f_{anoxic} represents the fraction of U deposited in anoxic facies and $\delta^{238}U$ represents the $\delta^{238}U$ values of the anoxic and "other" (i.e., non-anoxic) sinks. Following Montoya-Pino et al. (2010), it is assumed: (1) isotopically constant U input from rivers (the largest source of U to the ocean (Dunk et al. 2002)) over geologic time with a value of -0.3‰; (2) a constant isotope fractionation between seawater and anoxic/euxinic environments of +0.5‰; and (3) a constant (+0.1‰) isotope fractionation between seawater and the sum of other sinks, including ferromanganese oxide, hydrothermal, and suboxic sediments. Suboxic sediments are defined by their low oxygen concentrations in the bottom water (e.g., 0.2–2 ml O_2 in 1 l H_2O (Tyson and Pearson 1991)). Based on the assumptions above, $^{238}U_{input}$ = -0.3 ‰, $\delta^{238}U_{other}$ = -0.55‰ (i.e., -0.65+0.1 ‰), and $\delta^{238}U_{anoxic}$ = -0.15‰ (i.e., -0.65+0.5 ‰). These values yield an estimated six-fold increase in the flux of U to anoxic facies in conjunction with the EH.

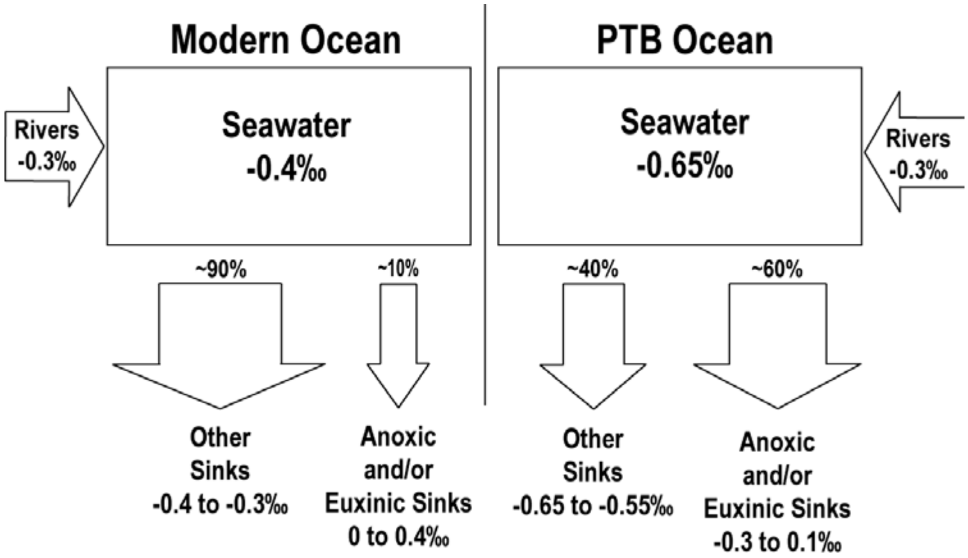

Fig. 4.3. Box models showing the modern ocean (left) and the hypothesized end-Permian anoxic ocean on the right. Estimates of the percentage of U flux for each sink are shown above the arrows. All data is displayed using standard δ-notation, as defined above. Modern $\delta^{238}U$ values are taken from Weyer et al. (2008). The values from the PTB ocean (right) are based on calculations using the average $\delta^{238}U$ of carbonates after the EH in the sample set (see equation 1) and assuming a constant isotope fractionation between seawater and anoxic sediments.

4.3.3 Th/U Ratios of the Dawen Carbonates

Th/U ratios serve as an additional and independent line of evidence for oceanic redox changes in conjunction with the end-Permian extinction. Previous workers have used Th/U ratios in reduced sediments as a proxy for ocean redox chemistry (Wignall andTwitchett 1996). As Th has only one redox state (Th^{4+}), its concentration in sediments is unaffected by redox chemistry. On the other hand, U is a redox-sensitive metal and is readily removed from seawater as insoluble U^{4+} under reducing conditions (Anderson et al. 1989; McManus et al. 2006; Morford et al. 1999), thus concentrating U relative to Th in anoxic facies. An increase in anoxic sedimentation reduces the concentration of U in seawater as more U is sequestered in organic-rich sediments. Because carbonates reflect the U concentration of the seawater in which they are deposited (Gvirtzman et al. 1973; Shen and Dunbar 1995), an increase in anoxic sedimentation results in an increase in the Th/U ratio of carbonate sediments. At Dawen, average Th/U ratios increase from 0.06 below the EH to 0.42 above the EH (Fig. 4.2). This increase reflects a decrease in the U content of seawater, possibly by a factor of ~7× if Th concentrations remained constant. A change in seawater U concentrations of this magnitude is consistent with the 6-fold expansion of oceanic anoxic inferred from $\delta^{238}U$ data, and is also consistent with the sharp decrease in U concentrations across the Permian-Triassic boundary (PTB) previously reported from a carbonate section in Oman (Ehrenberg et al. 2008).

The results are unlikely to have been affected by diagenesis. For example, neither $\delta^{238}U$ nor Th/U shows a correlation with degree of dolomitization or with terrigenous input; see section 4.4.2 for further discussion.

4.3.4 Implications for Late-Permian Ocean Models

The timing indicated by these data for the onset of ocean anoxia is difficult to reconcile with previous hypotheses of extended anoxia prior to the extinction event (Bond and Wignall 2005; Wignall and Twitchett 1996; Cao et al.

2009; Isozaki 1997). The abrupt increase in Th/U ratios and decrease in $\delta^{238}U$ that begins at or just below the EH indicate that the Late Permian ocean was not in a sustained anoxic state until immediately prior to the extinction event. This global redox signal is consistent with proxies recording local redox conditions (Wignall et al. 2010; Algeo et al. 2010b). In contrast, the steady and prolonged decline of carbonate $\delta^{13}C$ seen in many stratigraphic sections prior to the EH has been used to argue for an extended period of ocean stagnation and whole-ocean anoxia (Erwin et al. 2002). If so, $\delta^{238}U$ and Th/U in carbonates should track $\delta^{13}C$. This behavior is not observed (Fig. 4.2).

The existence of an unconformable surface in the Dawen section at the level of the EH (Fig. 4.2) makes exact assessment of the timing of global redox changes unattainable. If the missing section is equivalent to beds 25 and 26 at Meishan, it would represent a hiatus of about 50,000-75,000 years (Chen et al. 2009). However, it is noted that the $\delta^{13}C$ curve for Dawen (see figure 5 in (Chen et al. 2009)) shows an almost unbroken shift toward more negative values across the contact, suggesting that the hiatus was of limited duration. The persistence of low $\delta^{238}U$ and high Th/U ratios through the 10 meters of section above the EH that were analyzed in this study (Fig. 2) indicate that intensified anoxia persisted in the global ocean for a minimum of ~40,000-50,000 years following the end-Permian extinction (Chen et al. 2009; Mundil et al. 2010; Guo et al. 2008).

While these data do not support the extended period of whole-ocean anoxia prior to the EH inferred from $\delta^{13}C$ records, they do not invalidate the idea that the end-Permian mass extinction was caused by oceanic oxygen depletion and a subsequent buildup and release of H_2S from the oceans, as inferred on the basis of geochemical, isotopic and biomarker studies (Bond and Wignall 2005; Grice et al. 2005; Wignall and Twitchett 1996; Cao et al. 2009; Isozaki 1997). Commonly, models of this process invoke an extended period of sluggish ocean circulation, producing deep ocean anoxia and accumulation of H_2S. This interpretation was previously challenged by numerical models of the ocean-climate system suggesting that the deep ocean was most likely well ventilated throughout the Late Permian-Early Triassic interval (Winguth and Maier-Reimer 2005). It is proposed that the geochemical data and numerical models can be reconciled by hypothesizing expanded and more intense oxygen minimum zones at mid-depths in the late-Permian ocean (Algeo et al. 2010b; Algeo et al. 2011). Suboxic deep-ocean conditions during the Late Permian prior to the EH (Algeo et al. 2011, Algeo et al. 2010b) would have decreased the U concentration of the ocean, lowering the residence time of U in seawater and setting the stage for the rapid shift in Th/U at the EH observed at Dawen (Fig. 4.2). Suboxic deep-ocean conditions would not have markedly altered the U isotope budget of the global ocean, as suboxic sedimentation does not fractionate U isotopes with the same magnitude as anoxic sedimentation (Weyer et al. 2008;Montoya-Pino et al. 2010). Uranium isotopes would have shifted measurably only with an increase in anoxic sedimentation. However, transient disturbances to Late Permian oceans (e.g., warming or an increase in continentally derived nutrients (Algeo et al. 2011)) may have resulted in brief episodes of expansion of oxygen minimum zones before the end-Permian extinction, as reflected in light $\delta^{238}U$ ratios below the EH (-118 and -

97 cm). Expanded oxygen minimum zones could have accumulated significant H_2S in the photic zone (Algeo et al. 2011), resulting in release of toxic gasses into shallow-marine environments and the atmosphere (Meyer et al. 2008), similar to the degassing of H_2S in modern oxygen minimum zones in Namibia (Brüchert et al. 2009).

A model of ocean chemistry with widespread regions of relatively warm and poorly oxygenated deep water and localized intermittent sulfide maxima at mid-water depths (i.e., within the oxygen-minimum zone) satisfies not only $\delta^{13}C$ evidence previously used to argue for sustained oceanic anoxia prior to the EH, but also explains the observed geochemical and biogeochemical signatures associated with anoxia/euxinia at the close of the Permian. Development of mid-depth sulfide maxima poised on the edge of expansion into the surface water layer could account for the presence of biomarkers indicative of photic-zone euxinia in shallow-marine sections prior to the EH (Grice et al. 2005; Cao et al. 2009) without requiring anoxia of the deep ocean, which would alter the U isotope budget of seawater. Evidence from the U system indicates widespread oceanic anoxia only became pronounced and persistent at, or just preceding the EH. Thus, this study supports the possibility of H_2S as a killing mechanism, but calls for buildup of H_2S in the oxygen minimum zone rather than prolonged accumulation in the deep ocean.

4.4 METHODS AND FURTHER DISCUSSION

4.4.1 Sample Preparation and Measurement

Carbonate samples were obtained as powdered samples and dissolved using dilute (~1M) hydrochloric acid, leaving any non-carbonate species present (e.g., organics, pyrite, siliciclastics, etc…) intact and non-participatory in the subsequent chemistry. The dissolved material was dried and brought up in 3M HNO_3. Approximately 10% of the material was used for trace element analyses, with data obtained using a Thermo X-series quadrupole ICP-MS at the W. M. Keck Laboratory for Environmental Biogeochemistry at ASU. The remaining 90% of the dissolved carbonate material was passed through a column containing Eichrom® UTEVA resin, following the procedure outlined in Weyer et al. (2008) to separate uranium from the matrix. Uranium isotope measurements were performed on a ThermoFinnigan Neptune MC-ICP-MS instrument at Arizona State University (ASU, W. M. Keck Laboratory for Environmental Biogeochemistry), utilizing a ^{236}U:^{233}U double-spike MC-ICP-MS procedure described in Weyer et al. (2008). The isotopic composition of the double spike used is $^{236}U/^{233}U = 1.00494$, $^{238}U/^{233}U = 0.000958$, $^{235}U/^{233}U = 0.000108$. Samples were spiked to achieve ^{236}U and ^{233}U signals of ~2.5 times the voltage on the least abundant measured isotope, ^{235}U. This spiking technique maximizes the counting statistics on the spike masses, while minimizing the tailing contributions at mass 235. All measured isotopes of U were collected by a Faraday cup collector array, utilizing 10^{11} ohm resistors for all masses. Samples dissolved in 2% HNO_3 were introduced with an Apex-Q sample introduction system. Optimum precision was obtained running samples at ~100 ppb U. The U isotope standards SRM950a and CRM129a were measured bracketing samples as checks for run reproducibility and consistency. External reproducibility based on multiple runs of the SRM950a and CRM129a standards over the course of this study is shown in Fig. 4.4. The U isotopic compositions of the samples are reported as relative to the U isotope standard SRM950a.

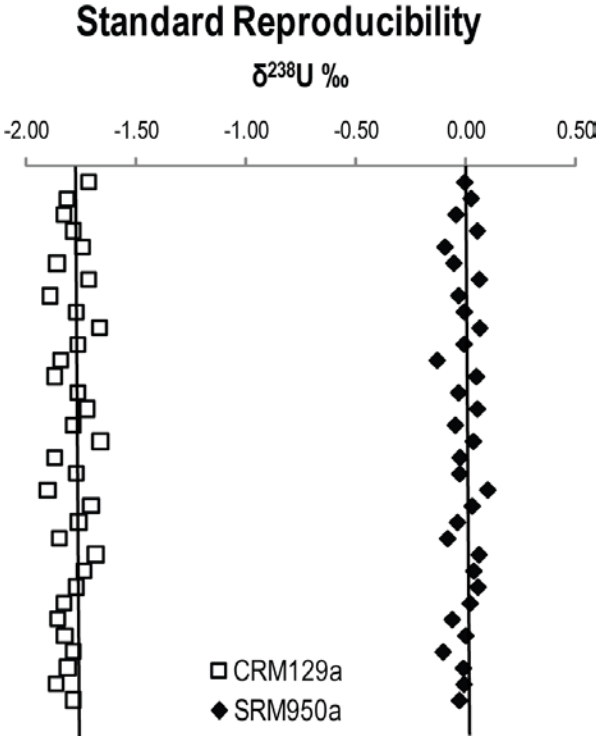

Fig. 4.4. The long-term external reproducibilities of the SRM950a and CRM129a standards for analyses performed during this study, relative to SRM950a. The solid vertical line represents the average of all analyses for the given sample. The average δ^{238}U values are represented for SRM950a and CRM129a are 0.00±0.11 and -1.79±0.13, respectively with both uncertainties calculated as 2×standard deviation (2SD).

4.4.2 Discussion on Secondary Alteration of Carbonates

Due to the reactivity of carbonates, diagenetic alteration of samples is a potential concern. Fluctuations of the δ^{238}U value in samples immediately below the extinction horizon (EH) at Dawen may indicate pre-extinction instability in the redox state of the ocean preceding the end-Permian extinction (Algeo et al. 2010a); however because these fluctuations are not seen in Th/U in the same samples, they could be the result of secondary processes such as addition of isotopically heavy U. Given the current understanding of the U isotope system there is no secondary process that generates isotopically lighter δ^{238}U values in carbonates, although secondary redox precipitation of U would produce heavy δ^{238}U in diagenetically altered samples (Weyer et al. 2008; Bopp et al. 2009; Brennecka et al. 2010).

Although it is difficult to rule out diagenesis in samples of this type, several considerations support the interpretation that variation in both δ^{238}U and Th/U at Dawen is mainly of primary origin. First, the major changes in both Th/U and δ^{238}U occur at, or immediately preceding, the EH. Data from δ^{238}U and Th/U are independent of one another, and both fit previously proposed models for isotopic and elemental response to ocean anoxia from other basins (Ehrenberg et al. 2008). The fact that the Dawen section displays a similar trend of U chemistry across the Permian-Triassic boundary as in Oman (Ehrenberg et al. 2008) argues for a global cause, rather than local diagenetic processes. Secondly, the current understanding of U chemistry in marine sediments argues against the local effects of diagenesis. The possibilities of altering the δ^{238}U and Th/U of the samples are primarily limited to 1) secondary precipitation of U and 2) removal of U from the system. In the first case, precipitation of U containing calcium carbonate cement as a secondary process is generally an early diagenetic process (Gvirtzman et al. 1973) and would thus reflect seawater values as well. Precipitation of uranium carbonate containing cements during late stage burial diagenesis could shift the isotopic values of the carbonate sediments; however, the conclusions that are being drawn would still be valid, even when assuming that the entire section has undergone some late burial cement precipitation, as the temporal trends should not change in a relative sense. In the second case, if U was being leached from the Dawen samples, only the Th/U ratio would be affected with $\delta^{238}U$ remaining unchanged. Unlike ^{234}U, which is concentrated in the aqueous phase by preferential leaching of alpha-recoil damage sites from the decay of ^{238}U[7], leaching of U has been shown not to measurably alter the $^{238}U/^{235}U$ ratio (Bopp et al. 2009; Brennecka et al. 2010; Stirling et al. 2007). Furthermore, it has been suggested that because U is incorporated into the calcium carbonate as a uranyl complex as part of a dilute solid solution, remobilization of U would require bulk dissolution (Reeder et al. 2000; Swart and Hubbard 1982). This should have no effect on the isotopic composition of the residual carbonate material as no leaching has taken place.

The carbonate $\delta^{13}C$ curve for Dawen shows good correspondence to $\delta^{13}C$ curves at other PTB sections, so it is unlikely that bulk carbonate $\delta^{13}C$ has been modified to any significant degree by diagenesis. Further, the carbonate sediment at Dawen appears to have stabilized early in the burial environment, as reflected in relatively heavy $\delta^{18}O$ values, which average -4.6±1.7‰ (n = 75). The absence of negative $\delta^{18}O$ outliers is also an indication of little, if any, late-stage diagenesis. These considerations are consistent with the idea that the carbonate $\delta^{13}C$ curve is a record of primary marine $\delta^{13}C$ values, adding confidence that U isotopes and Th/U signals are primary in origin.

The concentration of Al was obtained on the samples as an indicator of terrigenous input and is shown as U/Al. Virtually no correlations exist between $\delta^{238}U$ or Th/U when plotted against U/Al in these samples (Fig. 4.5), it is highly unlikely that the large changes in $\delta^{238}U$ and Th/U across the EH were caused by terrigenous input of U. Similarly, the $\delta^{238}U$ and Th/U are not controlled by lithology, as no correlation exists between $\delta^{238}U$ and the degree of dolomitization of the sample, and only a weak correlation exists between Th/U and percent dolomite ($R^2 = 0.24$).

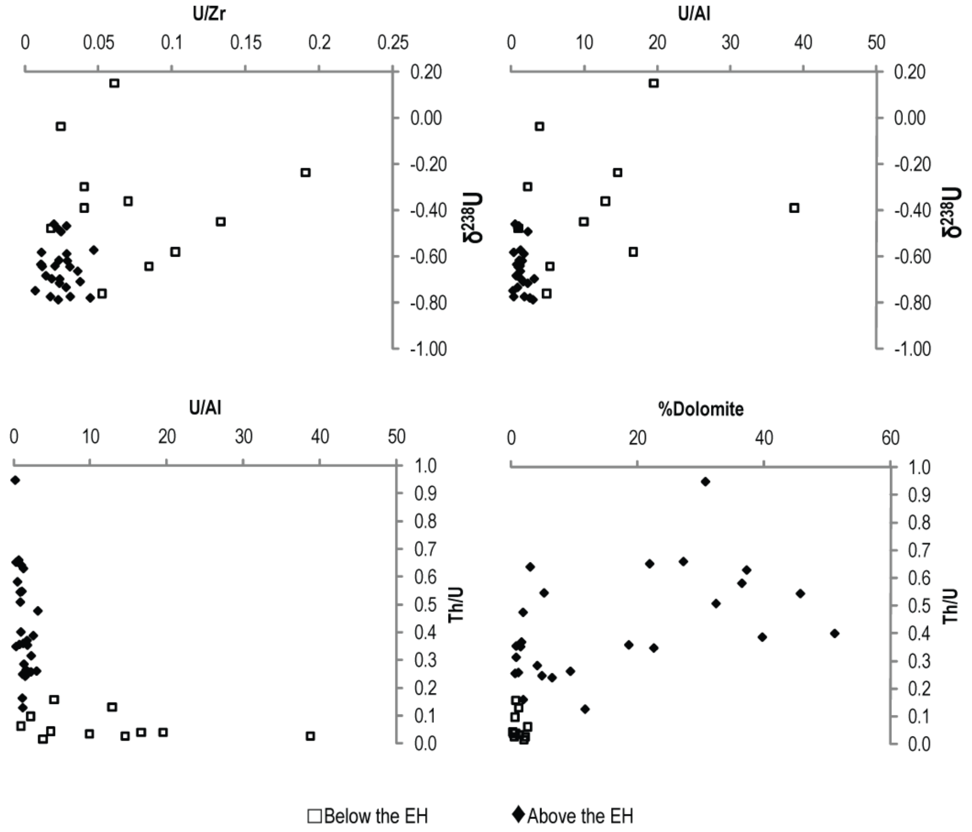

Fig 4.5. Crossplots of U/Al, U/Zr, and %Dolomite vs. Th/U and/or δ^{238}U. Open squares (□) represent samples below the EH, closed diamonds (♦) represent samples above the EH.

Chapter 5

^{238}U/^{235}U VARIATIONS IN METEORITES: EXTANT ^{247}CM AND IMPLICATIONS FOR PB-PB DATING[1]

5.1 INTRODUCTION

Meteorites can provide a wealth of information about the formation and evolution of the Solar System. In chondrite meteorites, calcium-aluminum-rich inclusions (CAIs) represent the first solids to condense from the cooling protoplanetary disk during the birth of the Solar System (Grey et al. 1973); therefore, the ages of CAIs are generally considered to date its origin (Amelin et al. 2002; Bouvier et al. 2007; Jacobsen et al. 2008). High precision Pb-Pb dating studies, which rely on a known ratio of parent U isotopes, assume that the ^{238}U/^{235}U ratio is invariant in meteoritic material (=137.88) (Chen and Wasserburg 1980). Uranium isotope variations in meteorites may be produced by many mechanisms, including the decay of extant ^{247}Cm to ^{235}U, nucleosynthetic anomalies in U isotopes, or fractionation of U isotopes during chemical reactions, as recently observed on Earth (Stirling et al. 2007; Weyer et al. 2008). While any or all of these mechanisms may play some role in ^{238}U/^{235}U variability in early Solar System materials, the existence and effect of ^{247}Cm on the ^{238}U/^{235}U ratio can be studied using geochemical proxies for Cm.

---

[1] This chapter and the values reported in it are given as published in Brennecka et al. (2010) in the journal *Science*. Subsequent work has shown the ^{238}U/^{235}U value of the SRM950a standard is not =137.88, as assumed in this work and discussed in section 5.5. All reported values of samples in this study would be subject to recalculation based on the newly determined value of SRM950a.

^{247}Cm is only created in certain types of supernovae during *r*-process nucleosynthesis. It decays to ^{235}U with a half-life of 15.6 Ma (Arden 1977; Tatsumoto and Shimamura 1980; Lugmair and Galer 1992; Stirling et al. 2005; Chen and Wasserburg 1981; Nittler and Dauphas 2006). If ^{247}Cm was present during the formation of the Solar System, it would be detected by variations of ^{238}U/^{235}U in ancient meteoritic materials in which the original Solar System Cm/U ratio may have been significantly fractionated by processes associated with their formation. The CAIs in chondritic meteorites are likely to be such materials, due to the fact that many of them experienced elemental fractionation during condensation/evaporation processes involved in their formation and since Cm is more refractory than U (Boynton 1978).

5.2 BACKGROUND

Quantification of the abundance of extant ^{247}Cm has the potential to provide new constraints on the origin of short-lived radionuclides in the early Solar System. If the ^{247}Cm in the early Solar System was predominantly inherited from galactic chemical evolution (Nittler and Dauphas 2006), then it should be possible to determine the time interval of free decay (Δ) between the last *r*-process nucleosynthetic event and the formation of the Solar System (Chen and Wasserburg 1980; Wasserburg et al. 1996; Wasserburg et al. 2006; Stirling et al. 2005). Supposed claims of large variations in the ^{238}U/^{235}U ratio caused by the decay of ^{247}Cm (Arden 1977; Tatsumoto and Shimamura 1980) were refuted in subsequent studies (Chen and Wasserburg 1980; Shimamura and Lugmair 1981;

Lugmair and Galer 1992; Stirling et al. 2005). Here, high-precision $^{238}U/^{235}U$ ratios obtained from 13 CAIs of the Allende meteorite are presented to quantify the amount of ^{247}Cm present in the early Solar System and to determine the extent of potential offsets in the calculated Pb-Pb ages of early Solar System materials.

5.3 RESULTS

The $^{238}U/^{235}U$ ratios of the two bulk meteorites (Allende and Murchison) are 137.818±0.012 and 137.862±0.042, respectively (Fig. 5.1). The 13 CAIs show a large range of U isotope compositions, with $^{238}U/^{235}U$ ratios varying from 137.409±0.039 to 137.885±0.009. All but two CAIs differ outside uncertainties from the standard value and five CAIs have significantly lower $^{238}U/^{235}U$ values than that of bulk Allende.

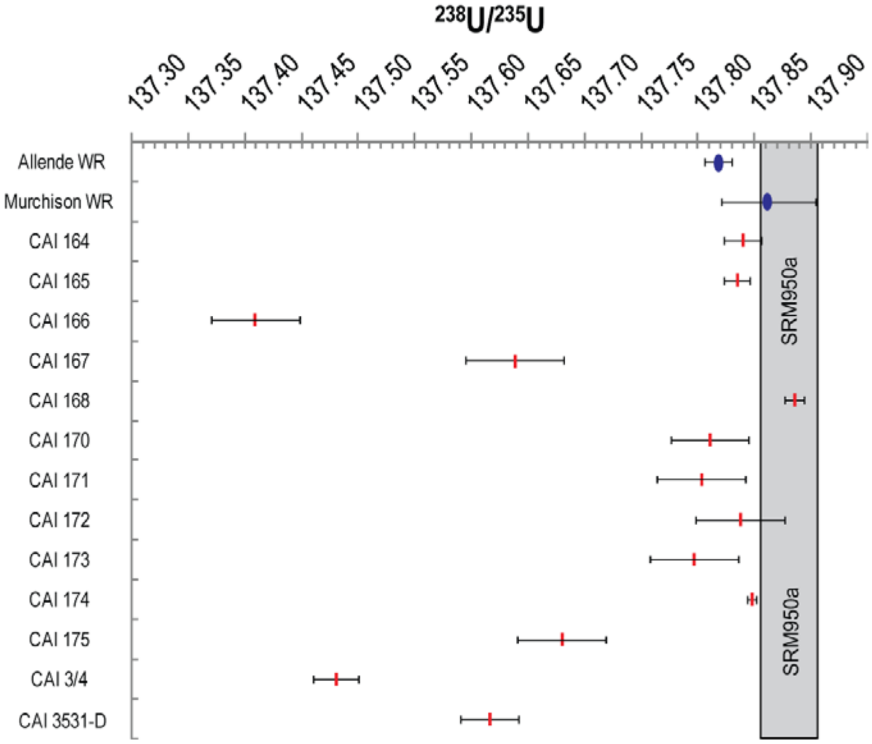

Fig. 5.1. $^{238}U/^{235}U$ isotope values for the samples of this study. The box represents the measured value and analytical precision of replicate analyses of 20-100 ppb solutions of the SRM950a standard. Error bars are calculated as 2 × the standard deviation (2SD) of multiple runs of each sample, when possible. In samples with extremely limited uranium, for which fewer than 3 runs were possible, the reported errors are conservatively represented by the long term reproducibilities (2SD) based upon multiple runs of SRM950a measured over the course of this study at the same concentration as the sample.

If ^{247}Cm decay is the primary mechanism for $^{238}U/^{235}U$ variability, then materials with high initial Cm/U would contain a higher relative amount of ^{235}U than those with lower initial Cm/U. However, as Cm has no long-lived stable isotope, the initial Cm/U ratio of a sample cannot be directly determined. Because Th and Nd have similar geochemical behavior to Cm, Th/U and Nd/U ratios can serve as proxies for the initial Cm/U ratio in the sample (Tatsumoto and Shimamura 1980; Stirling et al. 2005). This sample set spans a large range of Th/U and Nd/U, and both these ratios correlate with the U isotopic composition (Fig. 5.2).

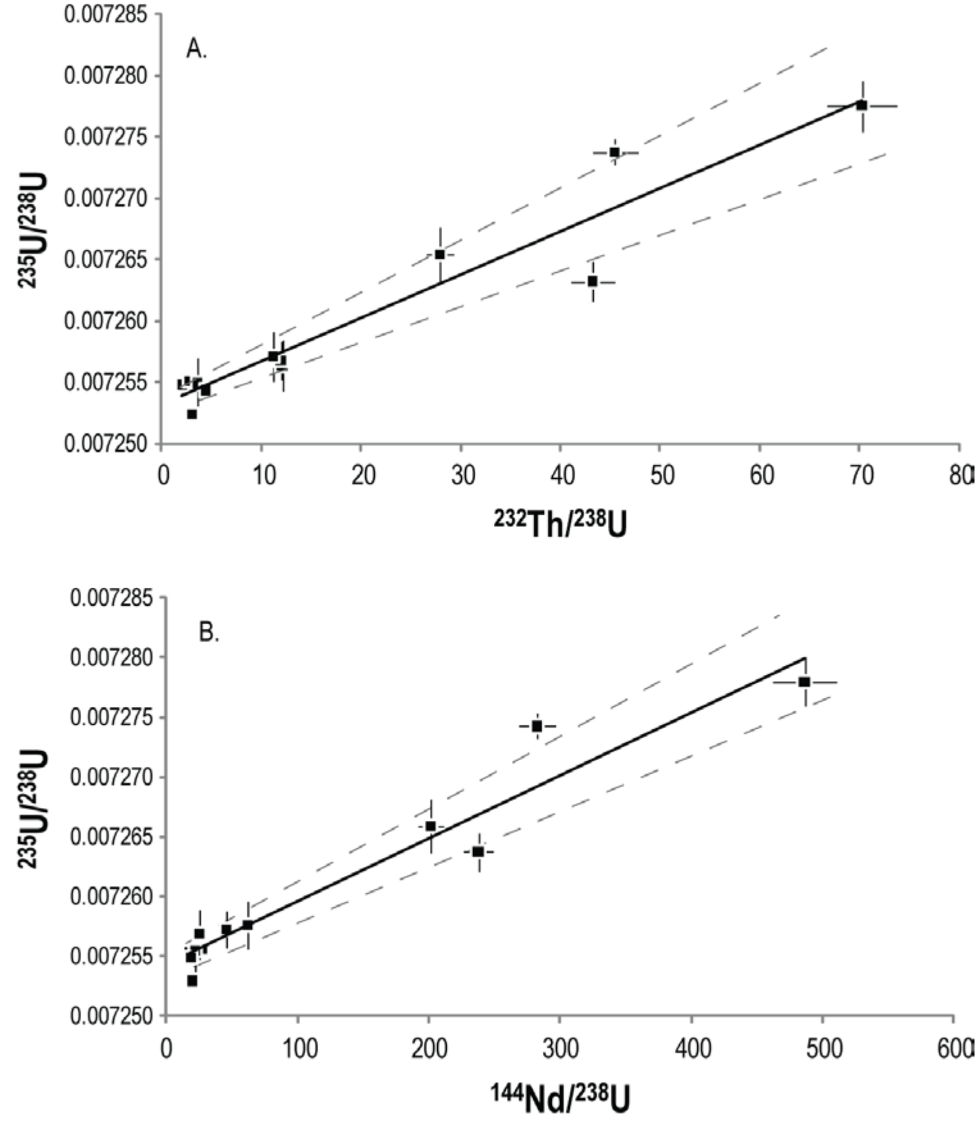

Fig. 5.2. $^{232}Th/^{238}U$ and $^{144}Nd/^{238}U$ ratios plotted versus $^{235}U/^{238}U$ ratios, the reciprocal values of the measured $^{238}U/^{235}U$ ratios. The grey dashed lines represent the 2SD errors on the best-fit line (solid black). Errors on the Y-axis data are ±2SD; X-axis error bars are ±5% of the determined value of the elemental ratio.

5.4 DISCUSSION

5.4.1 Elemental fractionation in CAIs

Due to the higher volatility of uranium, thermodynamic calculations suggest that substantial fractionation of Cm (and other geochemically similar elements such as Th and Nd) from U is possible in the early solar nebula (Blake and Shramm 1973). Large variations in the Th/U and Nd/U ratios seen in this CAI data set (Table 5.1) support this claim. A special group of CAIs, called "Group II" CAIs, are distinguished by a unique abundance pattern of the rare earth elements (REEs); they are highly depleted in the most refractory (i.e., heavy REE except Tm and Yb) and the most volatile (i.e., Eu and Yb) REEs, yet the moderately refractory light REE (including Nd) are only present in chondritic relative abundances (MacPherson 2003). This REE pattern characteristic of Group II CAIs suggests a complex condensation history involving fractional condensation (Boynton 1975; Davis and Grossman 1979). The four CAIs of this study that have the highest Nd/U and Th/U ratios (as well as the lowest $^{238}U/^{235}U$ ratios) are all classified as Group II CAIs by their REE patterns (Fig. 5.3). Due to the lower condensation temperature of U relative to Nd and Th (Mason and Taylor 1982), the fractional condensation history that resulted in the characteristic Group II REE pattern in these objects is likely to have produced the relatively high Nd/U and Th/U ratios.

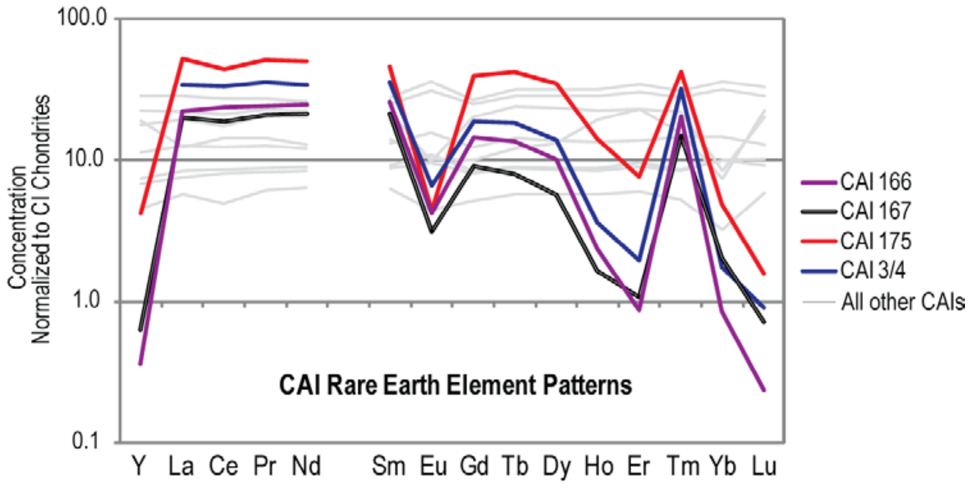

Fig. 5.3. REE patterns of four Group II CAIs analyzed in this study, normalized to CI chondrites. All other CAI samples studied here (except 3531-D, for which the REE abundances were not measured) display flat REE patterns indicating chondritic relative abundances of these elements (light-grey lines).

Table 5.1. The uranium isotope and elemental ratio data obtained in this study, as well as the calculated adjustment in the Pb-Pb age required given the measured $^{238}U/^{235}U$ ratio relative to that obtained if a value of 137.88 is assumed. The U isotope composition of meteoritic materials presented here is relative to the SRM950a standard, for which the $^{238}U/^{235}U$ value of 137.88 was assumed. Errors on the U isotope ratios are calculated as 2× the standard deviation (2SD) of multiple runs of each sample, when possible; for N<3, the errors are taken to be the long-term reproducibility (2SD) based on analyses of similar concentrations of the SRM950a standard conducted over the course of this study.

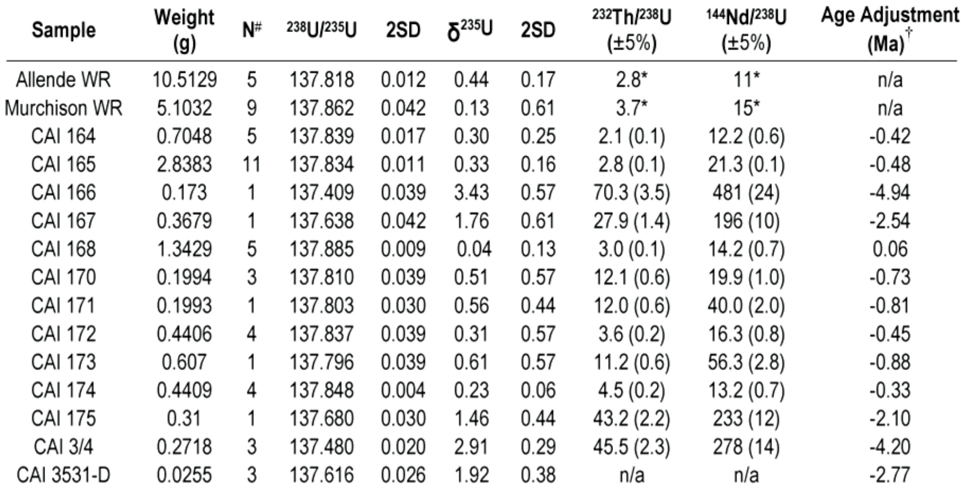

Sample	Weight (g)	N$^{\#}$	^{238}U/^{235}U	2SD	δ^{235}U	2SD	^{232}Th/^{238}U (±5%)	^{144}Nd/^{238}U (±5%)	Age Adjustment (Ma)†
Allende WR	10.5129	5	137.818	0.012	0.44	0.17	2.8*	11*	n/a
Murchison WR	5.1032	9	137.862	0.042	0.13	0.61	3.7*	15*	n/a
CAI 164	0.7048	5	137.839	0.017	0.30	0.25	2.1 (0.1)	12.2 (0.6)	-0.42
CAI 165	2.8383	11	137.834	0.011	0.33	0.16	2.8 (0.1)	21.3 (0.1)	-0.48
CAI 166	0.173	1	137.409	0.039	3.43	0.57	70.3 (3.5)	481 (24)	-4.94
CAI 167	0.3679	1	137.638	0.042	1.76	0.61	27.9 (1.4)	196 (10)	-2.54
CAI 168	1.3429	5	137.885	0.009	0.04	0.13	3.0 (0.1)	14.2 (0.7)	0.06
CAI 170	0.1994	3	137.810	0.039	0.51	0.57	12.1 (0.6)	19.9 (1.0)	-0.73
CAI 171	0.1993	1	137.803	0.030	0.56	0.44	12.0 (0.6)	40.0 (2.0)	-0.81
CAI 172	0.4406	4	137.837	0.039	0.31	0.57	3.6 (0.2)	16.3 (0.8)	-0.45
CAI 173	0.607	1	137.796	0.039	0.61	0.57	11.2 (0.6)	56.3 (2.8)	-0.88
CAI 174	0.4409	4	137.848	0.004	0.23	0.06	4.5 (0.2)	13.2 (0.7)	-0.33
CAI 175	0.31	1	137.680	0.030	1.46	0.44	43.2 (2.2)	233 (12)	-2.10
CAI 3/4	0.2718	3	137.480	0.020	2.91	0.29	45.5 (2.3)	278 (14)	-4.20
CAI 3531-D	0.0255	3	137.616	0.026	1.92	0.38	n/a	n/a	-2.77

$^{\#}$ Number of U isotope measurement runs (30 cycles of 8.4 second integrations) made on the sample
†Age difference between Pb-Pb ages (calculated using Isoplot/EX3.00 (Ludwig 2003)) determined based on the measured ^{238}U/^{235}U ratio and the assumed ^{238}U/^{235}U value of 137.88
* Data are from (Rochell and Jochum 1993)

The correlation of both Th/U and Nd/U with U isotope ratios in the CAIs indicates that the ^{238}U/^{235}U variations do not arise from nucleosynthetic anomalies or U isotope fractionation – neither of which easily give rise to such a trend – and instead provides evidence for the presence of extant ^{247}Cm in the early Solar System. Under this interpretation, deviations from the best-fit lines in Fig. 5.2 could be caused by heterogeneity of ^{238}U/^{235}U in the solar nebula, Th and Nd acting as imperfect proxies for Cm, or ^{238}U/^{235}U fractionation following Allende CAI formation, possibly from variable redox during secondary alteration processes (Weyer et al. 2008).

In contrast to these findings, a recent study did not detect deviations in the ^{238}U/^{235}U ratio among a variety of bulk meteorite samples, including Allende and Murchison (Stirling et al. 2005). Given the reported precision of the study's U isotope analysis, the ^{144}Nd/^{238}U ratios should have been sufficient to reveal detectable variations in ^{238}U/^{235}U from ^{247}Cm decay. Although the ^{238}U/^{235}U value of bulk Murchison samples agree within error with the observed values of this study, those for bulk Allende differ well outside of reported errors. The reason for this disagreement is unclear at this time.

5.4.2 Determining the interval of free decay

The initial ^{247}Cm/^{235}U ratio in the early Solar System can be estimated by using the slopes of the best-fit lines in Fig. 5.2 (Stirling et al. 2005). Using Th and Nd as proxies for Cm, it can be estimated that the initial Solar System ^{247}Cm/^{235}U ratio was $2.4\pm0.6\times10^{-4}$ and $1.1\pm0.2\times10^{-4}$, respectively. The difference between the estimates may be due to slight differences in the geochemical behavior of Th and Nd or possibly due to uncertainties in the assumed Solar System Nd/U or Th/U ratios. Nevertheless, these values are, on average, higher than the upper limit derived previously using analyses of the U isotope compositions of bulk chondritic meteorites (Stirling et al. 2005). The estimates of this study are, however, in agreement with the upper limit of $\sim4\times10^{-3}$ determined previously based on analyses of CAIs (Chen and Wasserburg 1981). If ^{247}Cm is inherited from galactic chemical evolution, the range of initial Solar System ^{247}Cm/^{235}U ratios estimated here translates to a $\Delta \sim$110 to 140 Ma. This value is similar to, but more precise than, previous estimates of Δ based on the inferred initial Solar System abundances of other *r*-process-only radionuclides such as ^{244}Pu and ^{129}I, but does not match the significantly shorter estimate of Δ (~30 Ma) derived from the initial abundance of ^{182}Hf (Wasserburg et al. 2006). However, because ^{182}Hf was overabundant in the early Solar System compared to its expected abundance from galactic chemical evolution, it may have been injected into the presolar molecular cloud or the solar nebula by a nearby supernova event [e.g., (Nittler and Dauphas 2006)].

5.4.3 Implications for Pb-Pb dating

The findings of this study also have implications for precise dating of early events in the history of the Solar System. The Pb-Pb age equation (Eqn. 1) has been used for decades to calculate the absolute ages of both meteoritic and terrestrial materials (Patterson 1956). This equation assumes that ^{238}U/^{235}U is invariant at any given time, and that the present-day value is 137.88.

$$\frac{^{207}\mathrm{Pb}^*}{^{206}\mathrm{Pb}^*} = \frac{^{235}\mathrm{U}\ \ e^{\lambda_{235}t} - 1}{^{238}\mathrm{U}\ \ e^{\lambda_{238}t} - 1} = \frac{1}{137.88}\ \frac{e^{\lambda_{235}t} - 1}{e^{\lambda_{238}t} - 1} \qquad (1)$$

Therefore, any deviation from this assumption would cause miscalculation in the determined Pb-Pb age of a sample. A difference of up to 3.5‰ implies that a correction of up to -5 Ma would be required if the Pb-Pb ages of these CAIs were obtained using the previously assumed ^{238}U/^{235}U value (Fig. 5.4).

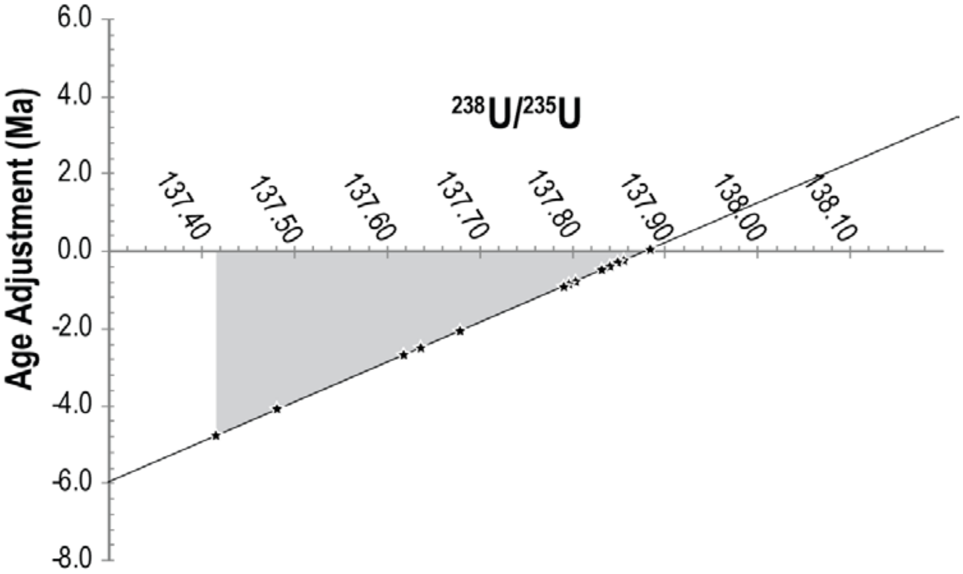

Fig. 5.4. Age adjustment required for samples found not to have a $^{238}U/^{235}U$ value of 137.88, as assumed in the Pb-Pb age equation. The shaded region represents the range of U isotope compositions reported in this study, and the star symbols represent the specific $^{238}U/^{235}U$ ratios measured in these samples.

Because $^{238}U/^{235}U$ variations in Solar System materials are not restricted to CAIs, this requirement may extend to high precision Pb-Pb dating of other materials as well. It is possible, however, that the $^{238}U/^{235}U$ values of bulk chondrites are controlled to a significant degree by CAIs, which may be heterogeneously distributed at the scale at which these analyses were made.

The Pb-Pb dating technique is the only absolute dating technique able to resolve age differences of < 1 Ma in materials formed in the early Solar System. While the full range of $^{238}U/^{235}U$ ratios reported here would result in an overestimation of the ages of these CAIs by up to 5 Ma, the largest excesses (>3.5‰) in ^{235}U occur in the Group II CAIs that appear to have experienced the largest Cm/U fractionation. For non-Group II CAIs, the age overestimation is ≤ 1 Ma. The apparent discrepancies between absolute Pb-Pb ages and relative (e.g., ^{26}Al-^{26}Mg, ^{53}Mn-^{53}Cr, ^{182}Hf-^{182}W) ages (Amelin et al. 2002; Jacobsen et al. 2008; Lugmair and Shukolyukov 1998; Burkhardt et al. 2008) may therefore place limits on the uncertainty of the age of the Solar System.

5.5 METHODS

Several CAIs, including both fine- and coarse-grained inclusions, were separated from different sections of the CV3 Allende meteorite. Samples were crushed and dissolved using a high pressure acid digestion system (made by PicoTrace) at the University of Frankfurt utilizing HNO_3, HF, and $HClO_4$ acids. Approximately 5% of each sample reserved for trace element measurements (i.e., REE patterns, Th/U and Nd/U ratios). Uranium from the remaining sample solutions was separated from the matrix for measurement of the ^{238}U/^{235}U ratio, following a procedure outlined in (Weyer et al. 2008). Whole rock samples of Allende and Murchison (CM2) were processed using the same methods. To ensure that the chemical separation procedure for U is not producing in any analytical artifacts on the ^{238}U/^{235}U ratio measurements, the matrices (with U removed) of CAI 171 and of ~0.42 g Murchison WR were mixed with SRM950a and both passed through chemistry again; the results of U isotopic ratio measurements following these “matrix-addition” tests are shown in Table 5.2.

Table 5.2. The uranium isotope standard data for various instrument parameters, comparing the data obtained at ASU and UF. Also shown are the results of tests (chemistry procedure checks) that were run to check that no fractionation in U isotopes resulted from the chemical separation procedures, as well as the laboratory location (ASU and/or UF) where each sample was analyzed.

Instrument Parameters	Average SRM950a $^{238}U/^{235}U$	2SD
ASU (20-100 ppb U)	137.881	0.032
ASU (5-20 ppb U)	137.881	0.042
U. Frankfurt (20-100 ppb U)	137.884	0.018
U. Frankfurt (5-20 ppb U)	137.883	0.035
Combined (20-100 ppb U)	137.882	0.039
Combined (5-20 ppb U)	137.882	0.026
Chemistry Procedure Checks	$^{238}U/^{235}U$	2SD
Murchison Matrix + SRM950a	137.882	0.018
CAI 171 Matrix + SRM950a	137.873	0.018
SRM950a only	137.887	0.018
Sample Measurement Locations	ASU	U. Frankfurt
Allende WR	X	X
Murchison WR	X	X
CAI 164	X	
CAI 165	X	X
CAI 166		X
CAI 167	X	
CAI 168	X	
CAI 170	X	X
CAI 171		X
CAI 172	X	X
CAI 173		X
CAI 174	X	X
CAI 175		X
CAI 3/4		X
CAI 3531-D		X

Measurement of the $^{238}U/^{235}U$ ratio was performed using ThermoFinnigan Neptune multicollector inductively coupled plasma mass spectrometer (MC-ICPMS) instruments at Arizona State University (ASU, in the Isotope

Cosmochemistry and Geochronology Laboratory) and the University of Frankfurt (UF, at the Institut für Geowissenschaften), utilizing a ^{236}U:^{233}U double spike to correct for instrumental mass bias. Two separate ^{236}U:^{233}U double spikes were used during this study, and both double spikes were used at both labs to check for consistency. They are referred to henceforth as the UF double spike and the ASU double spike, referring to the lab at which they were calibrated. The isotopic composition of the UF double spike is ^{236}U/^{233}U = 0.65920, ^{238}U/^{233}U = 0.00249, ^{235}U/^{233}U = 0.000824 (Weyer et al. 2008). The isotopic composition of the ASU double spike is ^{236}U/^{233}U = 1.00525, ^{238}U/^{233}U = 0.000958, ^{235}U/^{233}U = 0.000108.

Multiple samples and standards were measured on both instruments independently to ensure the quality and reproducibility of the data. Table 5.2 and Figures 5.5a and 5.5b show the long-term reproducibility of the SRM950a standard at both ASU and the University of Frankfurt over the course of this study. Table 5.2 also indicates of the laboratory (ASU or UF) where each sample measurement was made.

Trace element data (REEs, Th/U, Nd/U) was obtained using a both a Thermo X-series quadrupole ICP-MS at the W. M. Keck Laboratory for Environmental Biogeochemistry at ASU, and a Thermo Element2 ICP-MS at UF. No trace element data was collected on CAI 3531-D.

The U isotopic compositions of the samples are reported as ^{238}U/^{235}U ratios calculated relative to the U isotope standard SRM950a, with an assumed ^{238}U/^{235}U=137.88 (Shields 1960; Chen and Wasserburg 1980; Chen and Wasserburg 1981). With this method precise determinations of the differences in the ^{238}U/^{235}U compositions of individual samples relative to the standard can be obtained, with errors (given the typically small amounts of U in the samples) ranging from ±0.05 to ±0.2‰ (2SD). External reproducibility (based on multiple runs of the SRM950a standard over the course of this study) is shown in Fig. 5.5 for different concentration ranges of SRM950a measured at both ASU and UF. Calculations of initial ^{247}Cm assume a value of 0.138 for the ^{247}Cm/^{238}U production ratio (Nittler and Dauphas 2006).

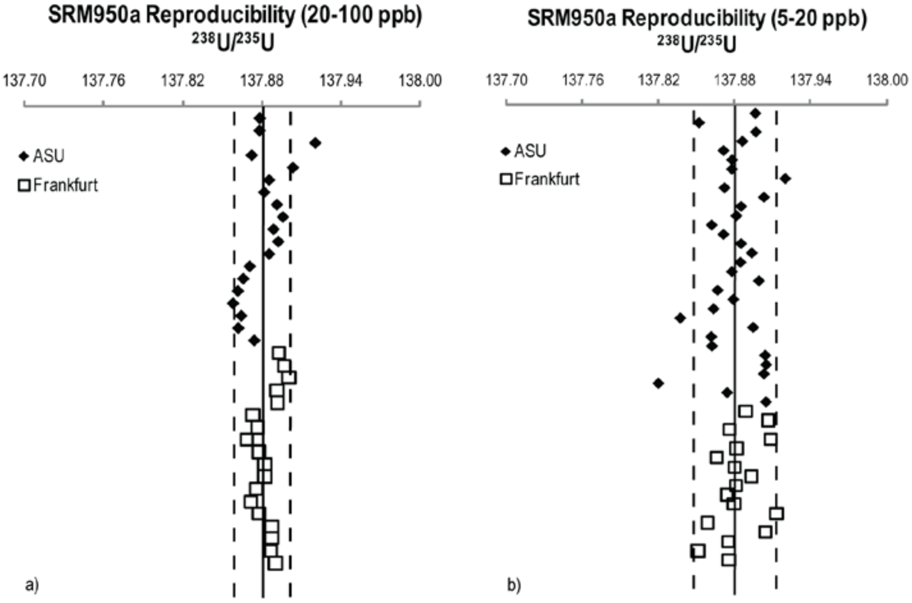

Fig. 5.5. The long-term external reproducibilities of different concentration ranges of SRM950a standard for analyses performed at ASU and UF. The solid vertical line represents the average of all analyses for the given concentration range, and the dashed lines represent the long-term reproducibility (2SD). The average

$^{238}U/^{235}U$ values represented for SRM950a are 137.882±0.026 and 137.882±0.039 for data shown in Fig. 5.5a and 5.5b, respectively.

Chapter 6

ADJUSTMENTS TO THE AGES OF ANGRITE TIME ANCHORS: THE IMPORTANCE OF $^{238}U/^{235}U$ FOR THE SHORT-LIVED CHRONOMETERS

6.1 INTRODUCTION

The time from the formation of the first solids in the Solar System to differentiation of planetary bodies is less than 10 million years (Ma) (Nyquist et al. 2009; references therein). As such, extremely precise and accurate geochronology is required to unravel this early sequence of events. A very limited number of radiometric chronometers can provide the sub-Ma precision necessary to resolve early Solar System events. These include short-lived chronometers such as ^{26}Al-^{26}Mg ($t_{1/2}$ ~0.72 Ma), ^{53}Mn-^{53}Cr ($t_{1/2}$ ~3.7 Ma), and ^{182}Hf-^{182}W ($t_{1/2}$ ~9 Ma), as well as the long-lived lead-lead (Pb-Pb) chronometer. Previous studies have revealed inconsistencies between ages determined for the same meteoritic object by different high-resolution chronometers (e.g., Nyquist et al. 2009; Wadhwa et al. 2009). These discrepancies may be caused by a variety of reasons, including heterogeneous distribution of the short-lived radionuclides and resetting of different isotopic systems to different degrees by secondary processes. The assumption of an invariant $^{238}U/^{235}U$ ratio in Solar System materials could also be responsible for some of these discrepancies since it may result in erroneous Pb-Pb ages of the time anchors.

The Pb-Pb system is the only *absolute* dating technique able to resolve sub-Ma time differences. Because ^{238}U and ^{235}U decay to ^{206}Pb and ^{207}Pb, respectively, a known $^{238}U/^{235}U$ is required for age calculation, as shown in equation 1. This equation also shows the previously assumed value for $^{238}U/^{235}U$ (=137.88).

$$\frac{^{207}Pb^*}{^{206}Pb^*} = \frac{^{235}U}{^{238}U}\frac{e^{\lambda_{235}t} - 1}{e^{\lambda_{238}t} - 1} = \frac{1}{137.88}\frac{e^{\lambda_{235}t} - 1}{e^{\lambda_{238}t} - 1} \qquad (1)$$

6.2 BACKGROUND

6.2.1 Time Anchors

Recent work has shown that the assumption of an invariant $^{238}U/^{235}U$ ratio in Solar System materials is no longer valid (Brennecka et al. 2010a; Brennecka et al. 2010d; Amelin et al. 2010; Amelin et al. 2011) and the uranium isotopic compositions must be measured to obtain accurate Pb-Pb dates. Also, the high-resolution relative ages of early Solar System events based on extinct chronometers (such as ^{26}Al-^{26}Mg) must be “anchored” by precise and accurate absolute ages from Pb-Pb dating. Therefore, determination of the uranium isotope compositions of meteoritic objects that serve as age anchors is particularly important since this has implications for the accuracy of the absolute model ages obtained using short-lived chronometers.

6.2.2 Angrites as Time Anchors

The accuracy of the absolute model ages obtained using short-lived chronometers is ultimately dependent on the choice of an appropriate meteoritic material to serve as an age anchor. An ideal age anchor 1) contains measureable quantities of the daughter products of multiple short-lived radioisotope systems (e.g. ^{26}Al-^{26}Mg, ^{53}Mn-^{53}Cr, and ^{182}Hf-^{182}W) 2) cooled rapidly while those systems were still “live”, and 3) has remained undisturbed by secondary alteration since the initial closure of these isotopic systems.

Angrites are a small group of basaltic achondrites distinguished by ancient crystallization ages and unique geochemical and mineralogical characteristics (Mittlefehldt et al., 1998). Several of these achondritic meteorites have been used in previous studies as age anchors for the short-lived chronometers (Burkhardt et al. 2008; Kleine et al. 2009; Goodrich et al. 2010). Currently known angrites define two distinct subgroups: the plutonic (course-grained) and quenched (fine-grained) angrites. Geochemical evidence suggests both subgroups originated from the same angrite parent body (Floss et al. 2003), but the crystallization of the quenched angrites predates that of the plutonic angrites by ~7 My (Amelin et al. 2008).

The quenched angrites in particular can serve as suitable age anchors for multiple short-lived chronometers for a variety of reasons. First, these angrites are basaltic samples, meaning they originated from crystallization of a melt, and were therefore isotopically homogenized at the time of their original formation. Secondly, they formed early enough in the history of the Solar System that they are likely to contain measureable excesses of the daughter products of several short-lived radionuclides. Additionally, they crystallized and cooled rapidly at the time of their formation, so the isotope systems associated with both extinct and long-lived chronometers closed at effectively the same time in these samples.

Among the quenched angrites, the D’Orbigny meteorite represents an especially attractive age anchor because it is relatively unmetamorphosed and has consequently remained unaltered by secondary processing (Mittlefehldt et al. 2002). In several recent studies, the short-lived ^{26}Al-^{26}Mg, ^{53}Mn-^{53}Cr, and ^{182}Hf-^{182}W systems have been anchored to the Pb-Pb age of the D’Orbigny angrite (e.g., Wadhwa et al. 2009; Burkhardt et al. 2008; Kleine et al. 2009), and thus, the model ages calculated based on these extinct chronometers inherently depend on the precision and accuracy of the Pb-Pb date of the D’Orbigny anchor. The previously reported highly precise absolute Pb-Pb age of 4564.42±0.12 Ma for the D’Orbigny angrite (Amelin et al. 2008) is based on an internal isochron from pyroxene separates and whole rock fractions, but assumes a ^{238}U/^{235}U ratio of 137.88. This work reports precise measurements of the ^{238}U/^{235}U ratio in several angrite samples, including D’Orbigny, and discusses the implications for obtaining precise and accurate ages for early Solar System events.

6.3 RESULTS

Uranium isotope ratios in a pyroxene separate and two whole-rock fractions of D’Orbigny, a phosphate separate from Angra dos Reis (ADOR), whole-rock fractions of NWA 4590, NWA 4801 and NWA 6291, as well as an acid leach and remaining residue from a second whole-rock fraction of NWA 6291 were obtained during this study. All uncertainties reported here are 2 × standard deviation (2SD). A ^{238}U/^{235}U ratio of 137.778±0.034 is reported for the D’Orbigny pyroxene separate, 137.790±0.025 for a whole rock sample of

D'Orbigny (Bulk D'Orbigny-1), and 137.791±0.026 for another whole rock sample of D'Orbigny (Bulk D'Orbigny-2). Whole-rock fractions of NWA 4590, NWA 4801 and NWA 6291 yielded $^{238}U/^{235}U$ ratios of 137.772±0.026, 137.778±0.026, and 137.769±0.026, respectively. The 0.5M HNO_3 acid leach of a second whole-rock sample of NWA 6291 (Leach) yielded a $^{238}U/^{235}U$ of 137.800±0.026, with the remaining residue having a $^{238}U/^{235}U$ of 137.759±0.026. Finally, the ADOR phosphate separate has a $^{238}U/^{235}U$ ratio of 137.806±0.039. The data are summarized in Figure 6.1 and Table 6.1.

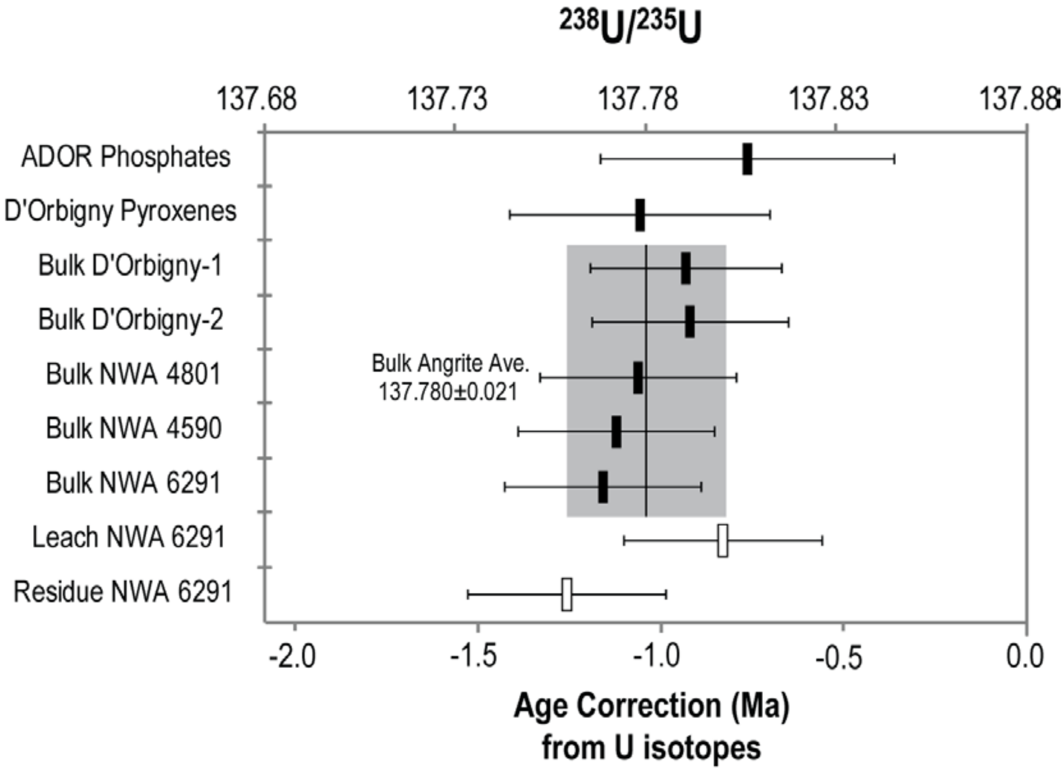

Fig. 6.1. The $^{238}U/^{235}U$ ratio of the samples of this study (upper axis) and the associated age correction (lower axis) based on the measured U isotope ratio

compared to the previously assumed value (^{235}U/^{238}U = 137.88). Uncertainties represent total 2SD uncertainties propagated from the uncertainties on the U isotope ratio measurements and the spike composition. The average value of bulk angrites is shown with a vertical line, with associated 2SD uncertainty in grey. This value represents the best estimate for the modern ^{238}U/^{235}U ratio of the angrite parent body.

Table 6.1. The U isotopic compositions of angrite samples measured in this study. The age adjustment is calculated based on the measured U isotope composition in comparison to the previous assumption of a ^{238}U/^{235}U ratio =137.88.

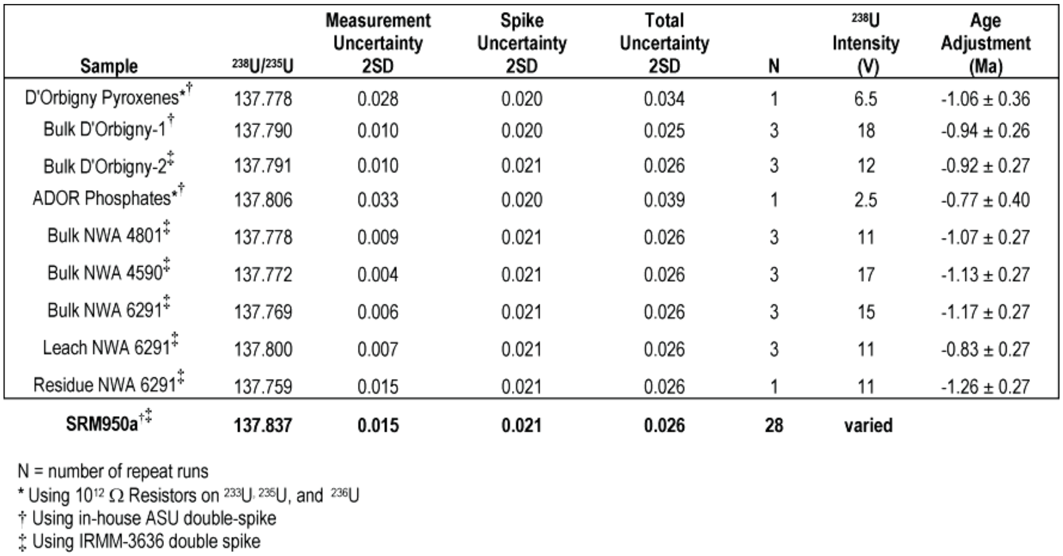

Sample	^{238}U/^{235}U	Measurement Uncertainty 2SD	Spike Uncertainty 2SD	Total Uncertainty 2SD	N	^{238}U Intensity (V)	Age Adjustment (Ma)
D'Orbigny Pyroxenes*†	137.778	0.028	0.020	0.034	1	6.5	-1.06 ± 0.36
Bulk D'Orbigny-1†	137.790	0.010	0.020	0.025	3	18	-0.94 ± 0.26
Bulk D'Orbigny-2‡	137.791	0.010	0.021	0.026	3	12	-0.92 ± 0.27
ADOR Phosphates*†	137.806	0.033	0.020	0.039	1	2.5	-0.77 ± 0.40
Bulk NWA 4801‡	137.778	0.009	0.021	0.026	3	11	-1.07 ± 0.27
Bulk NWA 4590‡	137.772	0.004	0.021	0.026	3	17	-1.13 ± 0.27
Bulk NWA 6291‡	137.769	0.006	0.021	0.026	3	15	-1.17 ± 0.27
Leach NWA 6291‡	137.800	0.007	0.021	0.026	3	11	-0.83 ± 0.27
Residue NWA 6291‡	137.759	0.015	0.021	0.026	1	11	-1.26 ± 0.27
SRM950a†‡	**137.837**	**0.015**	**0.021**	**0.026**	**28**	**varied**	

N = number of repeat runs
* Using 10^{12} Ω Resistors on ^{233}U, ^{235}U, and ^{236}U
† Using in-house ASU double-spike
‡ Using IRMM-3636 double spike

6.4 DISCUSSION AND IMPLICATIONS

6.4.1 Age change of angrites

Samples of this study include a mix of quenched, plutonic, and angrite mineral separates and these materials have $^{238}U/^{235}U$ values that are indistinguishable from one other within the reported uncertainties. This uniformity suggests that $^{238}U/^{235}U$ variation did not exist on the angrite parent body (APB) or between angrite mineral phases at the current level of precision. Given this isotopic uniformity, an average of the $^{238}U/^{235}U$ ratios of the bulk angrites measured in this study (=137.780±0.021) provides the best estimate for the $^{238}U/^{235}U$ ratio of the APB, and thus, of any meteorite originating from this parent body. Using this average value as the $^{238}U/^{235}U$ composition for the angrites and propagating uncertainties from both this U isotopic composition and the previously reported Pb-Pb dates, the corrected Pb-Pb age for each sample is calculated and shown in Figure 6.2 and Table 6.2. Any sample that has been dated using a short-lived chronometer that utilizes any of these angrites as a time anchor requires an age adjustment of the same magnitude as that anchor.

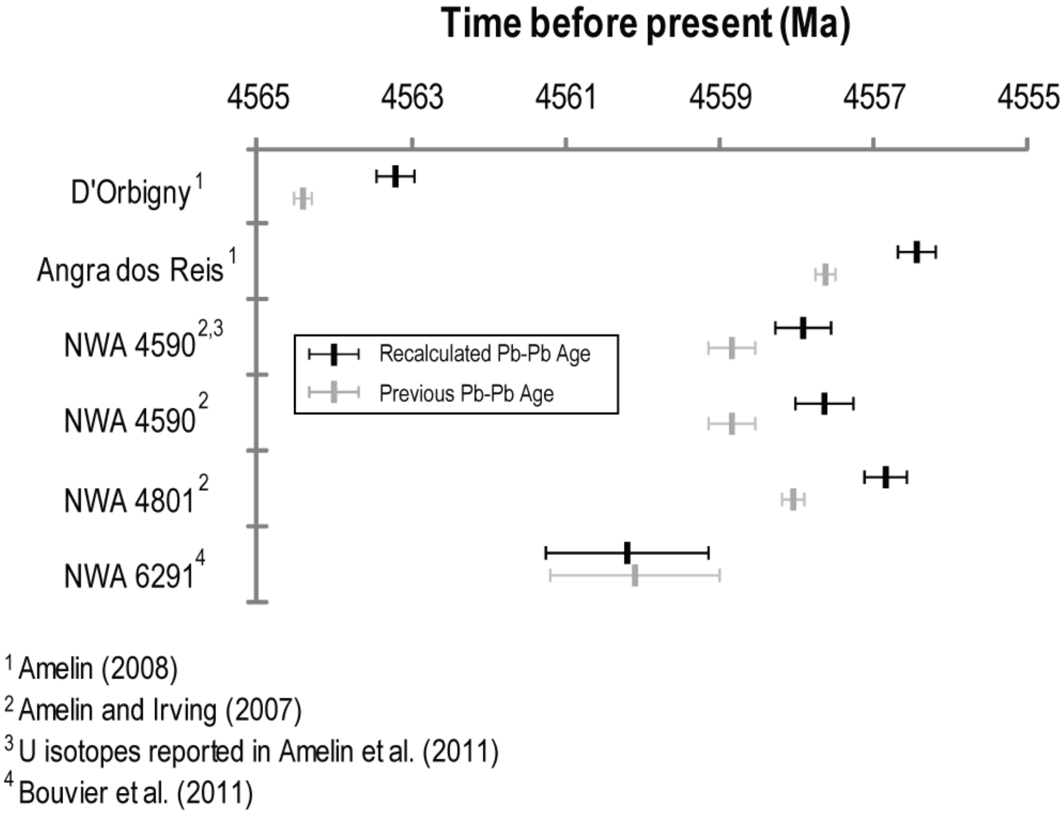

Fig. 6.2. Comparison of the Pb-Pb ages recalculated using the average $^{238}U/^{235}U$ ratio obtained from all angrite samples analyzed in of this study with the previously reported Pb-Pb ages. Recalculated age uncertainties include total 2SD uncertainties propagated from the uncertainties on the U isotope ratio measurements and the spike composition.

Table 6.2. Recalculated Pb-Pb ages of the angrites, with propagated 2SD uncertainty.

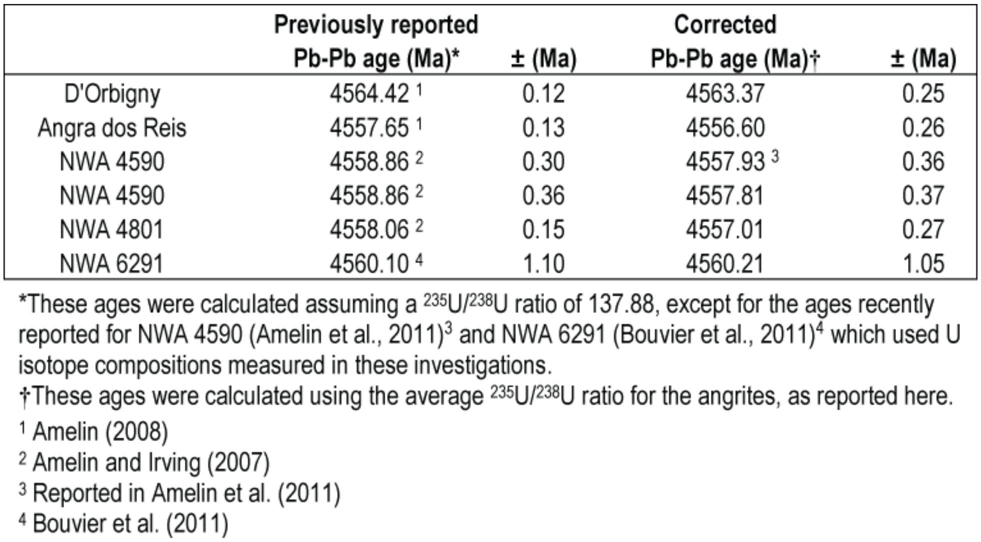

	Previously reported Pb-Pb age (Ma)*	± (Ma)	Corrected Pb-Pb age (Ma)†	± (Ma)
D'Orbigny	4564.42 [1]	0.12	4563.37	0.25
Angra dos Reis	4557.65 [1]	0.13	4556.60	0.26
NWA 4590	4558.86 [2]	0.30	4557.93 [3]	0.36
NWA 4590	4558.86 [2]	0.36	4557.81	0.37
NWA 4801	4558.06 [2]	0.15	4557.01	0.27
NWA 6291	4560.10 [4]	1.10	4560.21	1.05

*These ages were calculated assuming a $^{235}U/^{238}U$ ratio of 137.88, except for the ages recently reported for NWA 4590 (Amelin et al., 2011)[3] and NWA 6291 (Bouvier et al., 2011)[4] which used U isotope compositions measured in these investigations.

†These ages were calculated using the average $^{235}U/^{238}U$ ratio for the angrites, as reported here.

[1] Amelin (2008)

[2] Amelin and Irving (2007)

[3] Reported in Amelin et al. (2011)

[4] Bouvier et al. (2011)

6.4.2 Uranium isotopes on the angrite parent body

Recent analytical advances leading to significantly greater precision along with renewed interest have led to several investigations of the U isotopic compositions of meteoritic materials in recent years. While refractory calcium-aluminum-rich inclusions (CAIs) in the carbonaceous chondrite Allende have been shown to have large variability in $^{238}U/^{235}U$ ratios (Brennecka et al. 2010d; Amelin et al. 2010), the measured $^{238}U/^{235}U$ ratios of bulk samples of several types of chondrites and achondrites are all within analytical uncertainty of one another, and have an average $^{238}U/^{235}U$ ratio ≈137.78 (Brennecka et al. 2010a; Brennecka et al. 2010d; Amelin et al. 2010; Amelin et al. 2011; Bouvier et al. 2011a; Bouvier et al. 2011b; Kaltenbach et al. 2011). There are many other meteorite types that have not yet been measured, but the current data suggest that while the $^{238}U/^{235}U$ ratio of Solar System materials is resolvably distinct the previously assumed value of 137.88, the extent of U isotopic variation among bulk meteorites is likely to be relatively small (i.e., smaller than the current level of precision of the U isotope measurements of ±1-2 ε units).

6.4.3 Chronometer concordance

Obtaining the same age within uncertainties for multiple high-resolution chronometers on an object in which one might expect similar closure temperatures for these chronometers is a critical step in unraveling the sequence of events in the early Solar System. If concordant ages are not obtained, and if there is not clear petrographic or geochemical evidence indicating that significantly different closure times may be expected for different chronometers, the confidence in time constraints obtained from such chronometers is diminished. Measurement of $^{238}U/^{235}U$ ratio as part of the Pb-Pb dating procedure of samples, particularly those that can serve as time anchors, clearly has a significant implication for the accuracy of the reported dates. Moreover, this has a similarly major effect on the model ages obtained using other high-resolution chronometers based on extinct radionuclides that are anchored to these Pb-Pb dates, and could therefore impact the concordance of these various chronometers. An example of this is illustrated in Fig. 6.3, that shows the corrected Pb-Pb ages for several angrites and the unique achondrite NWA 2976 for which U isotope compositions have been measured (Bouvier et al. 2011b; this study), and compares these with high-resolution model ages calculated based on three extinct chronometers (Al-Mg, Mn-Cr and Hf-W; data for these chronometers are from references shown in Fig. 6.3) using D'Orbigny as the time anchor. As can be seen in Fig. 6.3, there is now good agreement between the ages for these various objects using the Pb-Pb absolute chronometer and the three extinct chronometers; this would not have been the case for previously published Pb-Pb ages of the various angrites (determined using $^{238}U/^{235}U = 137.88$; refs. Amelin et al. 2008; Amelin and Irving 2007) that were ~1 Ma older than shown here.

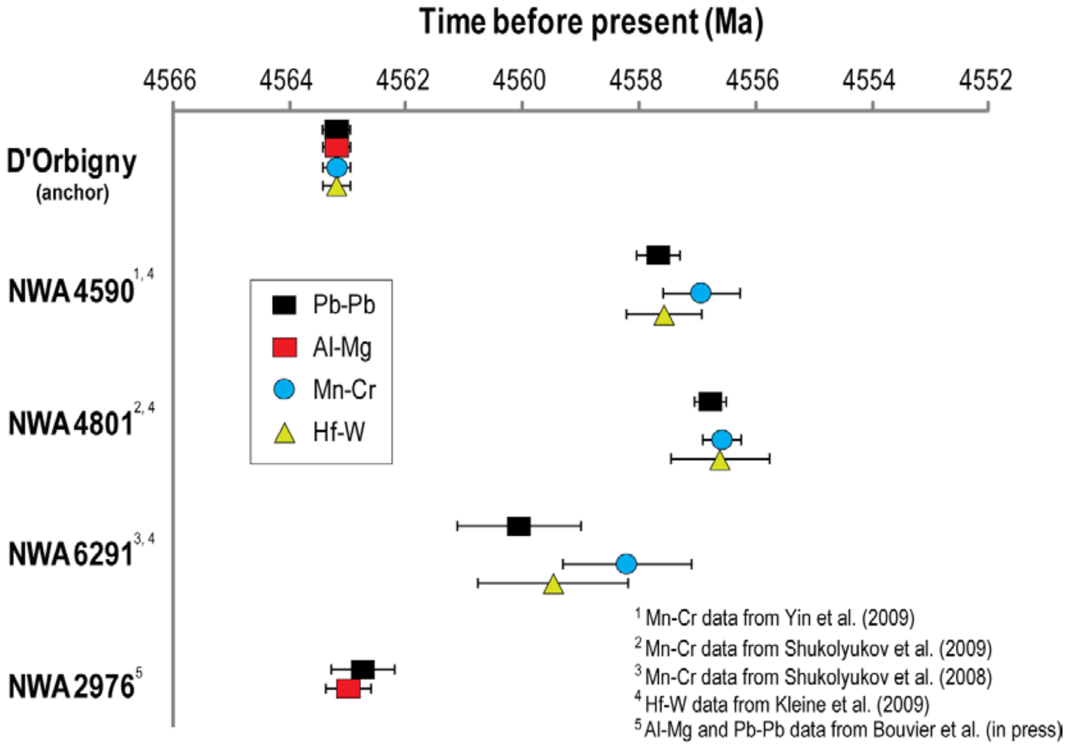

Fig. 6.3. Corrected Pb-Pb ages of the angrites (shown in Table 2, and calculated using the average $^{235}U/^{238}U$ ratio based on all angrite samples analyzed here) and the unique achondrite NWA 2976 (calculated using its measured $^{235}U/^{238}U$ ratio;

ref. Bouvier et al. 2011b) compared with model ages based on short-lived chronometers anchored to the corrected Pb-Pb age for D'Orbigny of 4563.37±0.25 Ma.

Finally, using the corrected age of D'Orbigny (4563.37±0.25 Ma), the "canonical" Solar System initial $^{26}Al/^{27}Al$ ratio (Lee et al. 1977; Jacobsen et al. 2008) and the $^{26}Al/^{27}Al$ at the time of crystallization of D'Orbigny (Spivak-Birndorf et al. 2009), the age of the Solar System is calculated to be 4568.2±0.4 Ma. This age is in good agreement with the Pb-Pb and Al-Mg internal isochron ages reported by Bouvier and Wadhwa (2010) for CAI 2364-B1 from NWA 2364. While the Pb-Pb age of CAI 2364-B1 does not include U isotope measurement, the $^{238}U/^{235}U$ is estimated for it using its measured Th/U ratio and the correlation of the Th/U ratio with the U isotope composition in Allende CAIs (Brennecka et al. 2010d). In comparison, high precision Pb-Pb internal isochron ages reported previously for other CAIs from Allende and Efremovka, and assuming a $^{238}U/^{235}U$ ratio of 137.88, are younger by ~1 Ma (Jacobsen et al. 2008; Amelin et al. 2002; Amelin et al. 2009). A more recent determination of the internal isochron Pb-Pb age for another Allende CAI, however, does include measurement of its U isotope composition, and also has a somewhat younger age (4567.18±0.50 Ma; Amelin et al. 2010) compared to that of the NWA 2364 CAI. While it is unclear at this time why this age discrepancy exists, it is possible that Pb-Pb systematics in Allende and Efremovka CAIs have been disturbed by secondary processes (e.g., Scott et al. 1992), thereby yielding systematically younger ages.

For obtaining the precise and accurate chronology of the early Solar System and understanding the time sequence of events during its first few millions of years, it is essential that the $^{238}U/^{235}U$ ratio be measured (and not assumed to be 137.88) when determining absolute Pb-Pb dates for meteoritic materials. This has been shown to be particularly important for refractory inclusions from the primitive chondrites in which large variations in the $^{238}U/^{235}U$ ratio (of up to ~3-4 per mil) have been reported (e.g., Brennecka et al. 2010d). This investigation demonstrates that while the $^{238}U/^{235}U$ ratio of the APB and meteorites originating from it is indeed also distinct from the previously assumed value of 137.88, it is uniform (at the current level of precision). Although the U isotope compositions of several other meteorite types remain to be measured, this study as well as some other recent investigations of the U isotope compositions of bulk sample of various undifferentiated and differentiated meteorites suggest that $^{238}U/^{235}U$ ratio in the early Solar System was homogenous on the scale of bulk samples.

6.5 MATERIALS AND METHODS

Multiple fragments of the D'Orbigny meteorite were obtained, two from the Center for Meteorite Studies (CMS) at Arizona State University (ASU) and one from R. Carlson (Carnegie Institution of Washington). Whole-rock samples of NWA 4590, NWA 4801, and NWA 6291 were obtained from the CMS. Interior fragments of all meteorites were obtained for analyses to avoid fusion crust and to minimize any terrestrial contamination. All chemical processing was performed under clean laboratory conditions in the Isotope Cosmochemistry and Geochronology Laboratory (ICGL) at ASU. One whole rock sample of D'Orbigny (1.1612 g) was gently crushed with agate mortar and pestle, sieved, and 174 mg of clean pyroxenes were separated by hand-picking. This pyroxene separate was then agitated in an ultrasonic bath for 5 minutes in 0.05M HCl. Other whole rock samples of D'Orbigny (0.5969 g and 0.7281 g), NWA 4801 (0.6112 g), NWA 4590 (0.7375 g), and NWA 6291 (0.6454 g) were crushed and washed following the same procedure. The samples were completely dissolved in Savillex® beakers using a mix of concentrated HNO_3, HF, and HCl. An additional piece of NWA 6291 (0.3400 g) was acid leached, with material dissolved in 0.5M HNO_3 (ultrasonicated) designated as "Leach". The residue remaining from this leaching was completely dissolved using a mix of concentrated HNO_3, HF, and HCl, and was designated as "Residue". Hand-picked phosphates (5.4 mg) from ADOR were provided by G. J. Wasserburg (Caltech) and were dissolved directly in 3M HNO_3. Approximately 5% of each dissolved sample used in this study was reserved for trace element measurements. Uranium was separated from the remaining sample solutions for measurement of the $^{238}U/^{235}U$ ratio, following previously published procedures (Brennecka et al. 2010d; Weyer et al. 2008). Sample weights, total U contents and U concentrations are shown in Table 6.3.

Table 6.3. The weight, calculated total ng U and U concentration of each sample analyzed in this study.

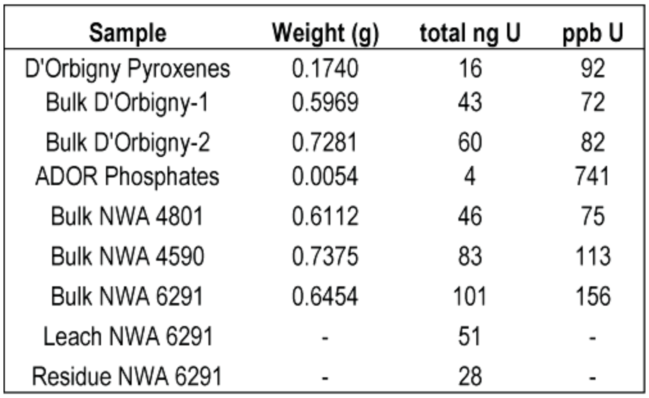

Sample	Weight (g)	total ng U	ppb U
D'Orbigny Pyroxenes	0.1740	16	92
Bulk D'Orbigny-1	0.5969	43	72
Bulk D'Orbigny-2	0.7281	60	82
ADOR Phosphates	0.0054	4	741
Bulk NWA 4801	0.6112	46	75
Bulk NWA 4590	0.7375	83	113
Bulk NWA 6291	0.6454	101	156
Leach NWA 6291	-	51	-
Residue NWA 6291	-	28	-

Uranium isotope measurements were performed on a ThermoFinnigan Neptune multicollector inductively coupled plasma mass spectrometer (MC-ICPMS) in the ICGL. All samples were measured using a ^{236}U:^{233}U double-spike to correct for instrumental mass bias. The ADOR phosphate separate, the D'Orbigny pyroxene separate and one of D'Orbigny whole rock samples were spiked with an in-house ASU double spike. The ASU double spike consists of a ~1:1 ratio of ^{236}U and ^{233}U with the minor contributions of ^{235}U and ^{238}U subtracted during data reduction ($^{236}U/^{233}U = 1.00496$; $^{238}U/^{233}U = 0.000958$; $^{235}U/^{233}U = 0.000108$). The second D'Orbigny whole rock sample, the whole rock samples of NWA 4590, NWA 4801, NWA 6291 as well as the leach and residue from NWA 6291 were spiked with the gravimetrically prepared IRMM-3636 double spike (Richter et al. 2008).

The long-term reproducibility of the U isotopic measurements was assessed by repeat measurements of the SRM950a standard over the course of this study (Fig. 6.4). The measured $^{238}U/^{235}U$ ratios of all samples are relative to the absolute value of the $^{238}U/^{235}U$ ratio of SRM950a (137.837±0.015), as reported in (Richter et al. 2010).

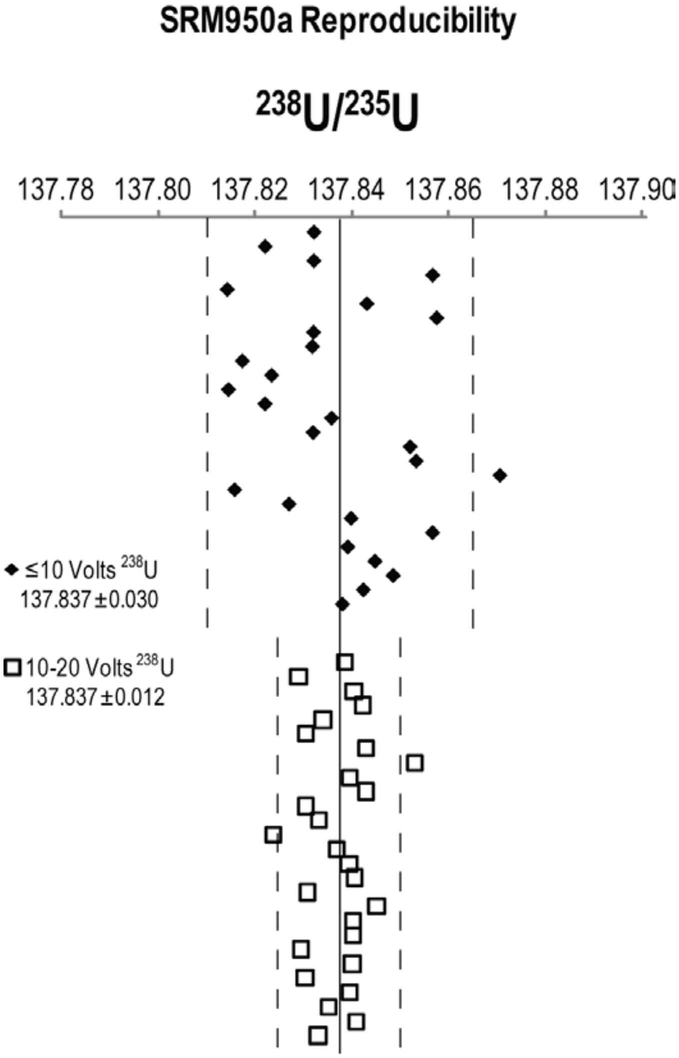

Fig. 6.4. The long-term external reproducibility of the SRM950a standard run at the same concentrations as the samples of this study. The dashed lines represent the long-term reproducibilities (2SD) at the specified concentration ranges. These are based only on the U isotope ratio measurement uncertainties and do not include the uncertainty associated with the composition of the double spike used.

All U isotope ratio measurement uncertainties ("Measurement Uncertainty" in Table 1) reported in this study are calculated as 2 × standard deviation (2SD) of multiple runs of the sample or same number of runs of the concentration-matched SRM 950a standard (analyzed during the same analytical session as the sample), whichever was larger. For samples with very limited uranium where only one run was possible, this uncertainty is calculated as 2SD of five or more runs of the SRM950a standard analyzed at the same concentration as that sample. Uncertainty on the value of the ASU in-house spike was determined by in-house calibration using the SRM950a standard, resulting in an inherent uncertainty of ±0.020 (2SD) on the $^{238}U/^{235}U$ ratio ("Spike Uncertainty" in Table 6.1). Thus, the total uncertainty on the U isotope composition of a sample measured using this in-house spike ("Total Uncertainty" in Table 6.1) includes the U isotope ratio measurement uncertainty for that sample as well as the propagated uncertainty on the in-house spike composition (which includes the error in the U isotope composition of SRM 950a). Similarly, the total uncertainty on the U isotope composition of a sample spiked with the gravimetrically prepared IRMM-3636 double spike ("Total Uncertainty" in Table 6.1) includes the U isotope measurement uncertainty for that sample as well as the propagated uncertainty on the absolute value of IRMM-3636 (Richter et al. 2008).

REFERENCES

Abdelouas, A., Lutze, W., Nuttall, E. (1998). Chemical Reactions of Uranium in Ground Water at a Mill Tailings Site. *Journal of Contaminant Hydrology* v. 34: p. 343–361.

Abe, M., Suzuki, T., Fujii, Y., Hada, M., Hirao, K. (2008). An *ab initio* Molecular Orbital Study of the Nuclear Volume Effects in Uranium Isotope Fractionations. *The Journal of Chemical Physics* v. 129: p. 164309-1-164309-7.

Algeo, T. J., Chen, Z. Q., Fraiser, M. L. & Twitchett, R. J. (2011, in press). Terrestrial-marine teleconnections in the collapse and rebuilding of Early Triassic marine ecosystems. *Palaeogeography Palaeoclimatology Palaeoecology*.

Algeo, T. J. et al. (2010a). Changes in productivity and redox conditions in the Panthalassic Ocean during the latest Permian. *Geology* v. 38: p. 187-190.

Algeo, T. J. et al. (2010b, in press). Spatial variation in sediment fluxes, redox conditions, and productivity in the Permian‑Triassic Panthalassic Ocean. *Palaeogeography, Palaeoclimatology, Palaeoecology*.

Amari, S., Hoppe, P., Zinner, E., and Lewis, R. S. (1995). Trace-element concentrations in single circumstellar silicon carbide grains from the Murchison meteorite. *Meteoritics* v. 30: p. 679-693.

Amelin, Y., Krot, A. N., Hutcheon, I. D., Ulyanov A. A. (2002). Lead isotopic ages of chondrules and calcium-aluminum‑rich inclusions. *Science* v. 297: p. 1678-1683.

Amelin, Y. (2008). U-Pb Ages of Angrites. *Geochimica et Cosmochimica Acta*, **72**, p. 221-232.

Amelin, Y. et al. (2009). Modern U–Pb chronometry of meteorites: Advancing to higher time resolution reveals new problems. *Geochimica et Cosmochimica Acta* v. 73: p. 5212–5223.

Amelin, Y., Kaltenbach, A., Iizuka, T., Stirling, C. H., Ireland, T. R., Petaev, M. Jacobsen, S. B. (2010). U–Pb chronology of the Solar System's oldest solids with variable $^{238}U/^{235}U$. *Earth and Planetary Science Letters* v. 300: p. 343-350.

Amelin, Y., Kaltenbach, A., Stirling, C. H. (2011). The U-Pb systematics and cooling rate of plutonic angrite NWA 4590. *Lunar and Planetary Science Conference* Abstract #1682.

Amelin, Y., and Irving, A. J. (2007). Seven million years of evolution on the angrite parent body from Pb-isotopic data. *Workshop on Chronology of Meteorites & the Early Solar System* Abstract #4061.

Angeli, I. (2004). A consistent set of nuclear rms charge radii: properties of the radius surface R(N, Z). *AtomicData and Nuclear Tables* v. 87: p. 185-206.

Anderson, R. F., Fleisher, M. Q. & Lehuray, A. P. (1989). Concentration, oxidation-state, and particulate flux of uranium in the Black-Sea. *Geochimica et Cosmochimica Acta* v. 53: p. 2215–2224.

Andreasen, R. and Sharma, M. (2006). Solar Nebula Heterogeneity in *p*-Process Samarium and Neodymium Isotopes. *Science* v. 314: p. 806-809.

Andreasen, R. and Sharma, M. (2007). Mixing and homogenization in the early Solar System: Clues from Sr, Ba, Nd and Sm isotopes in meteorites. *The Astrophysical Journal*, v. 655: p. 874-883.

Ankudinov, A.L., Ravel, B. Rehr, J.J. Conradson, S.D. (1998). Real-space multiple-scattering calculation and interpretation of X-ray absorption near-edge structure. *Physical Review B* v.58: p. 7565-7576.

Arden, J. W. (1997). Isotopic composition of uranium in chondritic meteorites. *Nature* v. 269: p. 788-789.

Arlandani, C., Käppeler, F., Wisshak, K., Gallino, R., Lugaro, M. Busso, M., Straniero, O. (1999). Neutron capture in low-mass asymptotic giant branch stars: cross sections and abundance signatures. *The Astrophysical Journal* v. 525: p. 886-900.

Aufmuth, P., Heilig, K. Steudel, A. (1987). Changes in mean-square nuclear-charge radii from optical isotope shifts, *Atomic Data and Nuclear Data Tables* v. 37: p. 455–490.

Bargar, J.R., Reitmeyer, R., Lenhart, J.J., Davis, J.A. (2000). Characterization of U(VI)-carbonato ternary complexes on hematite: EXAFS and electrophoretic mobility measurements. *Geochimica et Cosmochimica Acta* v. 64: p. 2737-2749.

Barling, J. Arnold G. L., Anbar A.D. (2001). Natural mass dependent variations in the isotope compositions of molybdenum. *Earth and Planetary Science Letters* v. 193: p. 447–457.

Barling, J., Anbar A. D. (2004). Molybdenum isotope fractionation during adsorption by manganese oxides. *Earth and Planetary Science Letters* v. 217: p. 315–329.

Bermingham, K. R., and Mezger, K. (2010). Ba isotope abundances in equilibrated meteorites and CAIs. *Lunar and Planetary Science Conference*, #1735.

Bertsch, P.M., Hunter, D. B., Sutton, S. R., Bajt, S., Rivers, M. L. (1994). *In situ* chemical speciation of uranium in soils and sediments by micro X-ray absorption spectroscopy. *Environmental Science & Technology* v. 28: p. 980-984.

Bigeleisen, J. (1996). Nuclear Size and Shape Effects in Chemical Reactions; Isotope Chemistry of the Heavy Elements. *Journal of the American Chemical Society* v. 118: p. 3676-3680.

Blake, J. B. and Schramm, D. N. (1973). A possible alternative to the *r*-process. *Nature* v. 289: p. 138-140.

Bond, D. P. G. and Wignall, P. B. (2005). Pyrite framboid study of marine Permian–Triassic boundary sections: A complex anoxic event and its relationship to contemporaneous mass extinction. *GSA Bulletin* v. 122: p. 1265-1279.

Boltwood, B. B., (1907). On the ultimate disintegration products of the radio-active elements. Part II. The disintegration products of uranium. *American Journal of Science* v. 23: p. 77-88.

Bopp, C. J., Lundstrom, C. C., Johnson, T. M., Glessner, J. J. G. (2009). Variations in ^{238}U/^{235}U in uranium ore deposits: Isotopic signatures of the U reduction process?. *Geology* v. 37: p. 611–614.

Bopp, C. J., Lundstrom, C. C., Johnson, T. M., Sanford, R. A., Long, P. E., Williams, K. H. (2010). Uranium ^{238}U/^{235}U isotope ratios as indicators of reduction: results from an *in situ* biostimulation experiment at Rifle, Colorado, U.S.A. *Environmental Science & Technology* v.44: p. 5927-5933.

Bouvier, A., Blichert-Toft, J., Moynier, F., Vervoort, J. D., Albarede, F. (2007). Pb‑Pb dating constraints on the accretion and cooling history of chondrites. *Geochimica et Cosmochimica Acta* v. 71: p. 1583-1604.

Bouvier, A. and Wadhwa, M. (2010). The age of the Solar System redefined by the oldest Pb‑Pb age of a meteoritic inclusion. *Nature Geoscience* v. 3: p. 637-641.

Bouvier, A., Brennecka, G. A., Sanborn, M. E., Wadhwa, M. (2011a). U-Pb Chronology of a newly recovered angrite. *Lunar and Planetary Science Conference* Abstract #2747.

Bouvier, A., Spivak-Birndorf, L. J., Brennecka, G. A., Wadhwa, M. (2011b) New constraints on early Solar System chronology from Al-Mg and U-Pb isotope systematics in the unique basaltic achondrite Northwest Africa 2976. *Geochimica et Cosmochimica Acta* v. 75: p. 5310‑5323.

Boynton W. V. (1975). Fractionation in the solar nebula: condensation of yttrium and the rare earth elements. *Geochimica et Cosmochimica Acta* v. 39: p. 569-589.

Boynton W. V. (1978). Fractionation in the solar nebula, II. Condensation of Th, U, Pu and Cm. *Earth and Planetary Science Letters* v. 40: p. 63-70.

Brennecka, G. A., Wadhwa, M., Janney, P. E., Anbar A. D. (2010a). Towards reconciling early solar system chronometers: the ^{238}U/^{235}U ratios of chondrites and D'Orbigny pyroxenes. *Lunar and Planetary Science Conference* Abstract #2117.

Brennecka, G. A., Borg, L. E., Hutcheon, I. D., Sharp, M. A. Anbar, A. D. (2010b). Natural variations in uranium isotope ratios of uranium ore concentrate: Understanding the ^{238}U/^{235}U fractionation mechanism. *Earth and Planetary Science Letters* v. 291: p. 228–233.

Brennecka, G. A., Borg, L. E., Wadhwa M. (2010c). Barium isotope compositions of Allende refractory inclusions: *r*-process excesses and evidence for ^{138}La decay. *Meteoritical Society Meeting* Abstract #5318.

Brennecka, G. A., Weyer, S., Wadhwa, M., Janney, P. E., Zipfel, J., Anbar, A. D. (2010d). ^{238}U/^{235}U Variations in Meteorites: Extant ^{247}Cm and Implications for Pb-Pb Dating. *Science* v. 327: p. 449-451.

Brüchert, V., Currie, B., and Peard, K. R. (2009). Hydrogen sulphide and methane emissions on the central Namibian shelf. *Progress In Oceanography* v. 83: p. 169-179.

Burkhardt, C., Kleine, T., Bourdon, B., Palme, H., Zipfel, J., Friedrich, J. M., Ebel, D. S. (2008). Hf–W mineral isochron for Ca,Al-rich inclusions: Age of the solar system and the timing of core formation in planetesimals. *Geochimica et Cosmochimica Acta* v. 72: p. 6177-6197.

Burkhardt, C., Kleine, T., Oberli, F., Pack, A., Bourdon, B., Wieler, R. (2011). Nucleosynthetic Mo isotope anomalies in planetary materials as tracers of circumstellar disk processes. *Lunar and Planetary Science Conference* Abstract #2554.

Cao, C., et al. (2009). Biogeochemical evidence for euxinic oceans and ecological disturbance presaging the end-Permian mass extinction event. *Earth and Planetary Science Letters* v. 281: p. 188–201.

Carlson, R. W., Boyet, M., Horan, M. (2007). Chondrite Barium, Neodymium, and Samarium Isotopic Heterogeneity and Early Earth Differentiation. *Science* v. 316: p. 1175-1178.

Carlson, R. W., Qin, L., Alexander, C. M. O'D. (2010). Ba, Nd, and Sm isotope anomalies in Murchison leaches: Distinct carriers of *s*- and *r*-process nucleosynthetic components. *Lunar and Planetary Science Conference* Abstract #2415.

Catalano, J. G., Brown, Jr., G. E. (2005). Uranyl adsorption on montmorillonite: evaluation of binding sites and carbonate complexation. *Geochimica et Cosmochimica Acta* v. 69: p. 2995-3005.

Cowan, G. A., and Adler, H. H. (1976). The Variability of the natural abundance of ^{235}U. *Geochimica et Cosmochimica Acta* v. 40: p. 1487-1490.

Chen, J., Beatty, T. W., Henderson, C. M. & Rowe, H. (2009). Conodont biostratigraphy across the Permian–Triassic boundary at the Dawen section, Great Bank of Guizhou, Guizhou Province, South China: Implications for the Late Permian extinction and correlation with Meishan. *Journal of Asian Earth Sciences* v. 36: p. 442–458.

Chen, J., and Wasserburg, G. J. (1980). A search for isotopic anomalies in uranium. *Geophysical Research Letters* v. 7: p. 275-278.

Chen, J., and Wasserburg, G. J. (1981). The isotopic composition of uranium and lead in Allende inclusions and meteoritic phosphates. *Earth and Planetary Science Letters* v. 52: p. 1-15.

Condon, D. J., McLean, N., Noble, S. R., Bowring, S. A. (2010). Isotopic composition (^{238}U/^{235}U) of some commonly used uranium reference materials. *Geochimica et Cosmochimica Acta* v. 74: p.7127-7143.

Davis, A. M. and Grossman, L. (1979). Condensation and fractionation of rare earths in the solar nebula. *Geochimica et Cosmochimica Acta* v. 43: p. 1611-1632.

Delanghe, D., Bard, E., and Hamelin, B. (2002). New TIMS constraints on the uranium-238 and uranium-234 in seawaters from the main ocean basins and the Mediterranean Sea. *Marine Chemistry* v. 80: p. 79-93.

Dunk, R. M., Mills, R. A., and Jenkins, W. J. (2002). A reevaluation of the oceanic uranium budget for the Holocene. *Chemical Geology* v. 190: p. 45-67.

Ehrenberg, S. N., Svånå, T. A., and Swart, P. K. (2008). Uranium depletion across the Permian–Triassic boundary in Middle East carbonates: Signature of oceanic anoxia. *AAPG Bulletin* v. 92: p. 691–707.

Erwin, D. H., Bowring, S. A. & Yugan, J. (2002). in *Catastrophic events and mass extinctions: Impacts and beyond.* Boulder, CO: Geological Society of America Special Paper. p. 363–383.

Fehr, M., Rehkämper, M. Halliday, A. N., Hattendorf, B., Günther, D. (2009). Tellurium isotope compositions of calcium-aluminum-rich inclusions. *Meteoritics & Planetary Science* v. 44: p. 971-984.

Fernandes, H. M., Franklin, M. R., Veiga, L. H. S., Freita, P., Gomiero, L.A. (1996). Management of uranium mill tailing: Geochemical processes and radiological risk assessment. *Journal of Environmental Radioactivity* v. 30: p. 69-95.

Floss, C., Crozaz, G., McKay, G., Mikouchi, T., Killgore, M. (2003). Petrogenesis of Angrites. *Geochimica et Cosmochimica Acta* v. 67: p. 4775–4789.

Fujii, T., Moynier, F., Albarède, F. (2006). Nuclear field vs. nucleosynthetic effects as cause of isotopic anomalies in the early Solar System. *Earth and Planetary Science Letters* v. 247: p. 1-9.

Fujii, Y., Nomura, M., Onitsuka, H., Takeda, K. (1989). Anomalous isotope fractionation in uranium enrichment process. *Journal of Nuclear Science and Technology* v. 26: p. 1061-1064.

Gallino, R., Busso, M., Lugaro, M. (1997). in *Astrophysical Implications of the Laboratory Study of Presolar Materials.* New York, NY: American Institute of Physics. p. 115–153.

Gannoun, A., Boyet, M., Rizo, H., El Goresy, A. (2011). ^{146}Sm–^{142}Nd systematics measured in enstatite chondrites reveals a heterogeneous distribution of ^{142}Nd in the solar nebula. *Proceedings of the National Academy of Sciences* v. 108: p. 7693-7697.

Gounelle, M. and Russell, S.S. (2005). On early Solar System chronology: Implications of an heterogeneous spatial distribution of ^{26}Al and ^{53}Mn. *Geochimica et Cosmochimica Acta* v. 69: p. 3129–3144.

Goodrich, C. A. et al. (2010) ^{53}Mn-^{53}Cr and ^{26}Al-^{26}Mg ages of a feldspathic lithology in polymict ureilites. *Earth and Planetary Science Letters* v. 295: p. 531-340.

Gray, C. M., Papanastassiou, D. A., Wasserburg, G. J. (1973). The identification of early condensates from the Solar nebula. *Icarus* v. 20: p. 213-239.

Grice, K. et al. (2005). Photic zone euxinia during the Permian–Triassic superanoxic event. *Science* v. 307: p. 706–709.

Guo, G., Tong, J., Zhang, S., Zhang, J., Bai, L. (2008). Cyclostratigraphy of the Induan (Early Triassic) in West Pingdingshan Section, Chaohu, Anhui Province. *Science in China Series D: Earth Sciences* v. 51, p. 22-29.

Gvirtzman, G., Friedman, G. M. & Miller, D. S. (1973). Control and distribution of uranium in coral reefs during diagenesis. *Journal of Sedimentary Research* v. 43: p. 985-997.

Hamilton, W.C. (1965). Significance tests on the crystallographic R factor. *Acta Crystallographica* v. 18: p. 502.

Harper, C. L., Weismann, H., Nyquist, L. E. (1992). The search for ^{135}Cs in the early solar system: Very high precision measurements of barium isotopes in bulk Allende and refractory inclusions. *Meteoritics,* v. 27: p. 230.

Heilig, K., and Steudel, A. (1974). Changes in mean-square nuclear charge radii from optical isotope shifts. *Atomic Data and Nuclear Data Tables,* v.14: p. 613-638.

Hidaka, H., Ebihara, M., Yoneda, S. (2000). Neutron capture effects on samarium, europium, and gadolinium in Apollo 15 deep drill-core samples. *Meteoritics & Planetary Science* v. 35: p. 581-589.

Hidaka, H., Ohta, Y., Yoneda, S., DeLaeter, J. R. (2001). Isotopic search for live ^{135}Cs in the early solar system and possibility of ^{135}Cs-^{135}Ba chronometer. *Earth and Planetary Science Letters* v. 193: p. 459-466.

Hidaka, H., Ohta, Y., Yoneda, S. (2003). Nucleosynthetic components of the early solar system inferred from Ba isotopic compositions in carbonaceous chondrites. *Earth and Planetary Science Letters* v. 214: p. 455-466.

Holland, H. D. (2005). Sedimentary Mineral Deposits and the Evolution of Earth’s Near-Surface Environments. *Economic Geology* v. 100: p. 1489-1509.

Hoppe, P., Ott, U. (1997). in *Astrophysical Implications of the Laboratory Study of Presolar Materials.* New York, NY: American Institute of Physics.p. 27–58.

Huss, G. R. and Lewis, R. S. (1995). Presolar diamond, SiC, and graphite in primitive chondrites: Abundances as a function of meteorite class and petrologic type. *Geochimica et Cosmochimica Acta* v. 59: p. 115-160.

IAEA-TEC-DOC-427 (1987). Uranium deposits in Proterozoic Quartz-Pebble Conglomerates. *Technical Document Issued by the International Atomic Energy Agency, Vienna*.

IAEA-TEC-DOC-322 (1984). Surficial Uranium Deposits. *Technical Document Issued by the International Atomic Energy Agency, Vienna.*

IAEA-TEC-DOC-328 (1985).Geological Environments of Sandstone-type Uranium Deposits. *Technical Document Issued by the International Atomic Energy Agency, Vienna*.

IAEA-TEC-DOC-361 (1985). Vein-type Uranium Deposits. *Technical Document Issued by the International Atomic Energy Agency, Vienna.*

Institute for Reference Materials and Measurements (2005 revised). Certificate for Isotopic Reference material IRMM-184, B-2440, Geel, Belgium,

Isozaki, Y. (1997). Permian–Triassic boundary superanoxia and stratified superocean: Records from lost deep sea. *Science* v. 276: p. 235–238.

Jacobsen, B. et al. (2008). ^{26}Al-^{26}Mg and ^{207}Pb-^{206}Pb systematics of Allende CAIs: Canonical solar initial ^{26}Al/^{27}Al ratio reinstated. *Earth and Planetary Science Letters* v. 272: p. 353-364.

Kaltenbach, A., Stirling, C.H., Amelin, Y. (2011) Revised Ages of Angrites. *Mineralogical Magazine* v. 75: p. 1137.

Kigoshi, K. (1971). Alpha Recoil Thorium-234: Dissolution into Water and Uranium-234/Uranium-238 Disequilibrium in Nature. *Science* v. 173: p. 47–48.

Kleine, T. et al. (2009). Hf‑W chronology of the accretion and early evolution of asteroids and terrestrial planets. *Geochimica et Cosmochimica Acta* v. 73: p. 5150‑5188.

Klinkhammer, G. P. & Palmer, M. R. (1991). Uranium in the oceans: where it goes and why. *Geochimica et Cosmochimica Acta* v. 55: p. 1799-1806.

Ku, T.-L., Knauss, K., Mathieu, G.G. (1977). Uranium in the open ocean: concentration and isotopic composition. *Deep-Sea Research* v. 24: p. 1005–1017.

Kump, L. R., Pavlov, A. & Arthur, M. A. (2005). Massive release of hydrogen sulfide to the surface ocean and atmosphere during intervals of oceanic anoxia. *Geology* v. 33: p. 397-400.

Lee, T. Papanastassiou, D. A., Wasserburg, G. J. (1977). Aluminum-26 in the early solar system: Fossil or Fuel? The Astrophysical Journal v. 211: p. L107-L110.

Lodders, K. and Amari, S.(2005). Presolar grains from meteorites: Remnants from the early times of the solar system. Chemie der Erde v. 65 p. 93–166.

K. Ludwig (2003). *Isoplot/EX 3.00.*

Lugmair, G. W. and Galer, S. J. G. (1992). Age and isotopic relationships among the angrites Lewis Cliff 86010 and Angra dos Reis. *Geochimica et Cosmochimica Acta* v. 56: p. 1673-1694.

Lugmair, G. W. and Shukolyukov, A.(1998). Early solar system timescales according to ^{53}Mn-^{53}Cr systematic. *Geochimica et Cosmochimica Acta* v. 62: p. 2863-2886.

MacPherson, G. J. (2003). *Treatise on Geochemistry, Volume 1,* Amsterdam: Elsevier. p. 201-246.

Mason, B. and Taylor, S. R. (1982). Inclusions in the Allende Meteorite. *Contributions to the Earth Sciences* v. 25: p. 1-30.

McCulloch, M. T. and Wasserburg, G. J. (1978a). Barium and Neodymium Isotopic Anomalies in the Allende Meteorite *The Astrophysical Journal* v. 220: p. L15-L19.

McCulloch, M. T. and Wasserburg, G. J. (1978b). More Anomalies from the Allende Meteorite: Samarium *Geophysical Research Letters* v. 5: p. 599-602.

McManus, J., Berelson, W. M., Severmann, S., Poulson, R. L., Hammond, D. E., Klinkhammer, G. P.; Holm, C. (2006). Molybdenum and uranium geochemistry in continental margin sediments: Paleoproxy potential. *Geochimica et Cosmochimica Acta* v. 70: p. 4643–4662.

Meyer, K. M., Kump, L. R. & Ridgwell, A. (2008). The biogeochemical controls on photic-zone euxinia during the end-Permian mass extinction. *Geology* v. 36: p. 747-750.

Mittlefehldt, D. W., McCoy, T. J., Goodrich, C. A., Kracher, A. (1998) in Review in Mineralogy v. 36 (ed. J. J. Papike) p.1-195.

Mittlefehldt, D. W., Kilgore, M., Lee, M. T. (2002). Petrology and geochemistry of D'Orbigny, geochemistry of Sahara 99555, and the origin of angrites. *Meteoritics and Planetary Science* v. 37: p. 345-369.

Montoya-Pino, C., et al. (2010). Global enhancement of ocean anoxia during the OAE-2: A quantitative approach using U isotopes. *Geology* v. 38: p. 315-318.

Morford, J. L. & Emerson, S. (1999). The geochemistry of redox sensitive trace metals in sediments. *Geochimica et Cosmochimica Acta* v. 63: p. 1735-1750.

Moynier, F., Fujii, T., Telouk, P. (2009a). Nuclear field shift effect as a possible cause of Te isotopic anomalies in the early solar system—An alternative explanation of Fehr et al. (2006 and 2009). *Meteoritics & Planetary Science* v. 44: p. 1735-1742.

Moynier, F., Fujii, T., Telouk, P. (2009b). Mass-independent isotopic fractionation of tin in chemical exchange reaction using a crown ether. *Analytica Chimica Acta* v. 632: p. 234–239.

Mundil, R., Palfry, J., Renne, P. R., Brack, P. (2010). in *The Triassic Timescale*. London: Geological Society Special Publications. p. 41–60.

Neuilly, M., et al. (1972). Sur l'existencedans un passerecide d'un ereaction en chaine naturelle de fission, dans.le gisement d'uranium d'Oklo (Gabon). *Comptes Rendus Acad Sci Paris* v. 257: p. 1847–1849.

New Brunswick Laboratory Certificate of Analysis (2003). CRM 129-A Uranium Oxide (U_3O_8) Assay and Isotopic Standard, *Document issued by New Bruswick Laboratory, US Department of Energy*

Nittler, L. R. and Dauphas, N. (2006). *Meteorites and the Early Solar System II*. Tucson: The University of Arizona Press. p. 127-146.

Nyquist, L. E., Kleine, T., Shih, C.-Y., Reese, Y. D. (2009). The distribution of short-lived radioisotopes in the early solar system and the chronology of asteroid accretion, differentiation, and secondary mineralization. *Geochimica et Cosmochimica Acta* v.73: p. 5115–5136.

Patterson, C. C. (1956). The age of meteorites and the Earth. *Geochimica et Cosmochimica Acta* v. 10: p. 230-237.

Qian, Y. Z., Vogel, P., Wasserburg, G. J. (1998). Diverse supernova sources for the *r*-process. *The Astrophysical Journal* v. 494: p. 285.

Quitté, G., Halliday, A. H., Meyer, B. S., Markowski, A., Latkosczy, C., Günther D. (2007). Correlated iron 60, nickel 62, and zirconium 96 in refractory inclusions and the orgin of the solar system. *The Astrophysical Journal* v. 655: p. 678-684.

Ranen M. C., and Jacobsen S. B. (2006). Barium Isotopes in Chondritic Meteorites: Implications for Planetary Reservoir Models *Science* v. 314: p. 809-812.

Reeder, R. J., Nugent, M., Lamble, G. M., Tait, C. D. & Morris, D. E. (2000). Uranyl incorporation into calcite and aragonite: XAFS and luminescence studies. *Environmental Science and Technology* v. 34: p. 638-644.

Riccardi, A., Kump, L. R., Arthur, M. A. & D'Hondt, S. (2007). Carbon isotopic evidence for chemocline upward excursions during the end-Permian event. *Palaeogeography, Palaeoclimatology, Palaeoecology* v. 248: p. 73-81.

Richter, S., Alonso, A., De Bolle, W., Wellum, R., Taylor, P. D. P. (1999). Isotopic “fingerprints” for natural uranium ore samples. *International Journal of Mass Spectrometry* v. 193: p. 9-14.

Richter, S., Eykens, R., Kühn, H., Aregbe, Y., Verbruggen, A., Weyer, S. (2010). New average values for the n(^{238}U)/n(^{235}U) isotope ratios of natural uranium standards. *International Journal of Mass Spectrometry* v. 295: p. 94–97.

Richter, S., et al. (2008). The isotopic composition of natural uranium samples—Measurements using the new n(^{233}U)/n(^{236}U) double spike IRMM-3636. *International Journal of Mass Spectrometry* v. 269: p.145–148.

Rochell A. and Jochum P. K. (1993). Th, U and other trace elements in carbonaceous chondrites: Implications for the terrestrial and solar-system Th/U ratios. *Earth and Planetary Science Letters* v. 117: p. 265-278.

Schauble, E.A. (2006). Equilibrium Uranium Isotope Fractionation by Nuclear Volume and Mass-Dependent Processes. *Eos* v. 87: December supplement, abs. V21B-0570.

Schauble, E.A. (2007). Role of Nuclear Volume in Driving Equilibrium Stable Isotope Fractionation of Mercury, Thallium, and Other Very Heavy Elements. *Geochimica et Cosmochimica Acta,* v. 71: p. 2170-2189.

Scott, E. R. D., Keil, K., Stöffler D. (1992) Shock metamorphism of carbonaceous chondrites. *Geochimica et Cosmochimica Acta* v. 56: p. 4281-4293.

Shen, G. T. & Dunbar, R. B. (1995). Environmental controls on uranium in reef corals. *Geochimica et Cosmochimica Acta* v. 59: p. 2009-2024.

Shields W.R. (1960). NBS Meeting of the Advisory Committee 17-18 May, 1960.

Shimamura, T. and Lugmair, G. W. (1981). U-isotopic abundances *Lunar and Planetary Science Conference* Abstract p. 976-978.

Shock, E. L., Sassani, D. C., Betz, H. (1997). Uranium in Geologic Fluids: Estimates of Standard Partial Molal Properties, Oxidation Potentials, and Hydrolysis Constants at High Temperatures and Pressures. *Geochimica et Cosmochimica Acta* v. 61: p. 4245-4266.

Shukolyukov, A., Lugmair, G. W., (2008). Mn-Cr chronology of eucrite CMS 04049 and angrite NWA 2999. *Lunar and Planetary Science Conference* Abstract #2094.

Shukolyukov, A., Lugmair, G. W., Irving, A. J. (2009). Mn-Cr isotope systematics of angrite northwest Africa 4801. *Lunar and Planetary Science Conference* Abstract #1381.

Siebert C., Nägler T. F., von Blanckenburg, F., Kramers, J. D. (2003). Molybdenum isotope records as a potential new proxy for paleooceanography. *Earth and Planetary Science Letters* v. 211: p. 159–171.

Spivak-Birndorf, L., Wadhwa, M., Janney, P. (2009). ^{26}Al–^{26}Mg systematics in D'Orbigny and Sahara 99555 angrites: Implications for high-resolution chronology using extinct chronometers. *Geochimica et Cosmochimica Acta* v. 73: p. 5202–5211.

Stanley, S. M. (2007). An Analysis of the History of Marine Animal Diversity. *Paleobiology* v. 33: p. 1-55.

Stirling, C. H., Halliday, A. N., Porcelli, D. (2005). In search of live ^{247}Cm in the early solar system. *Geochimica et Cosmochimica Acta* v. 69: p. 1059-1071.

Stirling, C. H., Anderson, M. B., Potter, E-K., Halliday, A. N. (2007). Low-Temperature Isotopic Fractionation of Uranium. *Earth and Planetary Science Letters*, v. 264: p. 208-225.

Stroes-Gascoyne, S., Kramer, J. R., Snodgrass, W. J. (1987). Preparation, characterization and aging of δ-MnO_2, for use in trace metal speciation studies. *Applied Geochemistry* v. 2: p. 217-226.

Swart, P. K. & Hubbard, J. (1982). Uranium in scleractinian coral skeletons. *Coral Reefs* v. 1: p. 13-19.

Swarzenski, P. W., McKee, B. A., Skei, J. M., Todd, J. F. (1999). Uranium biogeochemistry across the redox transition zone of a permanently stratified fjord: Framvaren, Norway. *Marine Geochemistry* v. 67: p. 181-198.

Tatsumoto, M. and Shimamura, T. (1980). Evidence for live ^{247}Cm in the early solar system. *Nature* v. 286: p. 118-122.

Tizard, J., Lyon, I., Henkel, T. (2005). The gentle separation of presolar SiC grains from meteorites. *Meteoritics & Planetary Science* v. 40: p. 335-342.

Travaglio, C., et al. (1999). Galactic chemical evolution of heavy elements: from barium to europium. *The Astrophysical Journal* v. 521: p. 691-702.

Triquier, A., Elliott, T., Ulfbeck, D., Coath, C., Krot, A. N., Bizzaro M. (2009). Origin of Nucleosynthetic Isotope Heterogeneity in the Solar Protoplanetary Disk. *Science* v. 324: p. 374-376.

Tyson, R. V. & Pearson, T. H. (1991). in *Modern and Ancient Continental Shelf Anoxia*. Boulder, CO: Geololgical Society Special Publications. p. 1–26.

Urey, H.G. (1947). The thermodynamic properties of isotopic substances. *Journal of the Chemical Society* v. 1: p. 562–581.

Wadhwa, M., et al. (2009). Ancient relative and absolute ages for a basaltic meteorite: Implications for timescales of planetesimal accretion and differentiation. *Geochimica et Cosmochimica Acta* v. 73: p. 5189-5201.

Waite, T.D., Davis, J. A., Payne, T.E., Waychunas, G. A., Xu, N (1994). Uranium(VI) adsorption to ferrihydrite: Application of a surface complexation model. *Geochimica et Cosmochimica Acta* v. 58: p. 5465-5478.

Wasserburg, G. J., Busso, M., Gallino, R. (1996). Abundances of actinides and short-lived nonactindes in the interstellar medium: Diverse supernova sources for the r-processes. *The Astrophysical Journal* v. 466: p. L109–L113.

Wasserburg, G. J., Busso, M., Gallino, R., Nollet, K. M. (2006). Short-lived nuclei in the early Solar System: Possible AGB sources. *Nuclear Physics* v. 777: p. 5–69.

Wasylenki, L. E., Weeks, C. L., Bargar, J. R., Spiro, T. G., Hein, J. R., Anbar A. D. (*in review*). The molecular mechanism of Mo isotope fractionation during adsorption to birnessite. *Geochimica et Cosmochimica Acta*

Wasylenki, L. E., Rolfe, B. A., Weeks, C. L., Spiro, T. G., Anbar, A. D. (2008). Experimental investigation of the effects of temperature and ionic strength on Mo isotope fractionation during adsorption to manganese oxides. *Geochimica et Cosmochimica Acta* v. *72*: p. 5997-6005.

Webb, S. M. (2005). SIXPACK: A graphical user interface for XAS analysis using IFEFFIT. *Physica Scripta* T115: p. 1011-1014.

Weyer, S., Anbar, A. D., Gerdes, A., Gordon, G. W., Algeo, T. J., Boyle, E. A. (2008). Natural Fractionation of ^{238}U/^{235}U. *Geochimica et Cosmochimica Acta*, v. 72: p. 345-359.

Wignall, P. B. et al. (2010). An 80 million year oceanic redox history from Permian to Jurassic pelagic sediments of the Mino-Tamba terrane, SW Japan, and the origin of four mass extinctions. *Global and Planetary Change* v. 71: p. 109-123.

Wignall, P. B. & Twitchett, R. J. (1996). Ocean anoxia and the end-Permian mass extinction. *Science* v. 272: p. 1155–1158.

Winguth, A. M. E. & Maier-Reimer, E. (2005). Causes of the marine productivity and oxygen changes associated with the Permian–Triassic boundary: A reevaluation with ocean general circulation models. *Marine Geology* v. 217: p. 283–304.

Wisshak, K., Voss, F. Käppeler, F., Kazakov, L., Reffo, G. (1998). Stellar neutron capture cross section of the Nd isotopes. *Physics Reviews C* v. 57: p. 391-408.

Woosley, S. E., Howard W. M. (1978). The p-process in supernovae. *The Astrophysical Journal (supplement)* v. 36: p. 285-304.

Yin, Q.-Z., Amelin, Y., Jacobsen, B. (2009). Project milestones: Testing consistent chronologies between extinct ^{53}Mn-^{53}Cr and extant U-Pb systematics in the early Solar System. *Lunar and Planetary Science Conference* Abstract #2060.

APPENDIX A

BARIUM, NEODYMIUM, AND SAMARIUM ISOTOPIC SIGNATURES IN REFRACTORY INCLUSIONS: IMPLICATIONS FOR SOLAR SYSTEM FORMATION

A.1 INTRODUCTION

The elemental and isotopic composition of our Solar System is the result of a mixture of countless nucleosynthetic reactions from past generations of stellar environments. Isotopes of elements heavier than boron are created by three principal modes of production: the *p*-, *s*-, and *r*-processes. The *p*-process creates isotopes through photodisintegration reactions in supernova, forming proton-rich nuclei (Woosley and Howard, 1978). The *s*-process occurs from slow neutron addition in asymptotic giant branch (AGB) stars (Gallino et al. 1997), marching up the “valley of stability” using neutron addition to create, and occasional β-decay to stabilize, new isotopes. Rapid neutron addition (or the *r*-process) occurs in the extremely high neutron densities found in supernova (Qian et al. 1998). The *r*-process creates extraordinarily neutron-rich, radioactive isotopes which β-decay to stability, resulting in neutron-rich stable isotopes. A combination of these processes is responsible for the stable isotopes abundances present in all Solar System materials.

Variations in the non-radiogenic isotope compositions of meteoritic samples (including bulk samples, leachates and residues of chondritic meteorites, as well as refractory inclusions in chondrites) have often been interpreted as nucleosynthetic signatures resulting from distinct inputs of materials produced as a result of *p*-, *s*-, and *r*-processes (Harper et al., 1992; Hidaka et al., 2003; Ranen and Jacobsen, 2006; Andreasen and Sharma, 2006; Carlson et al., 2007; Andreasen and Sharma, 2007; Bermingham et al., 2010; Carlson et al., 2010;

Triquier et al., 2009; Gannoun et al. 2011). These isotopic compositions have been used to argue for heterogeneity and the degree of mixing in the early solar nebula, as well as the nature of potential carriers of the isotope anomalies.

Bulk chondrites contain a variety of materials, including assorted presolar materials which numerous studies have shown to have extreme isotopic compositions (see Lodders and Amari, 2005 for an extensive review). Moreover, because presolar materials are exceptionally small and difficult to identify and separate, the elemental and isotopic compositions of most types of presolar grains are entirely unknown with regard to the heavy elements. While an immense amount of information has and can be gained from the study of bulk chondrites, their complex composition can complicate any interpretation. Calcium-aluminum-rich inclusions (CAIs), which are found in chondrite meteorites, are an important carrier of isotopic information about the early Solar System. Unlike bulk chondrites, CAIs are not mixes of various Solar System components, but are high temperature condensates representing the first solids to form in the cooling protoplanetary disk during the birth of the Solar System (Gray et al. 1973). These refractory objects should contain primary information about the nucleosynthetic composition of the very early Solar System. Additionally, to assess mixing in the early Solar System, measurement of multiple CAIs should provide knowledge about the amount of heterogeneity found in the CAI forming region of the protoplanetary disk.

Barium (Ba), neodymium (Nd) and samarium (Sm) each have multiple stable isotopes. The isotopes of each of these elements have variable inputs from *p*-, *s*-, and *r*-process nucleosynthesis, making these elements ideal for an integrated study of nucleosynthetic signatures in meteoritic material. The pathways of creation for each isotope of Ba, Nd, and Sm are shown in Table A.1.

Table A.1. Nucleosynthetic pathways of isotope creation for Ba, Nd, and Sm. Values are taken from Arlandini et al. (1999), Wisshak et al. (1998) and Travaglio et al. (1999).

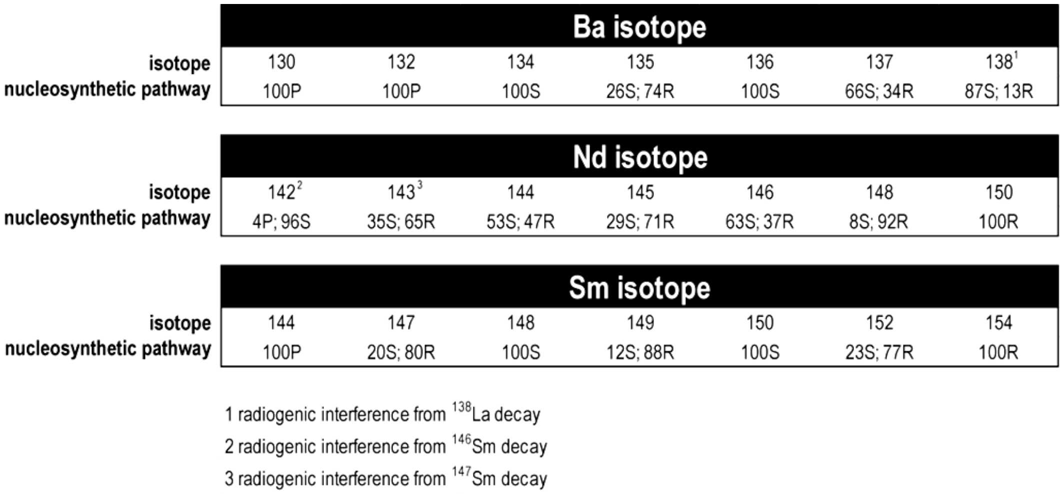

	Ba isotope						
isotope	130	132	134	135	136	137	138[1]
nucleosynthetic pathway	100P	100P	100S	26S; 74R	100S	66S; 34R	87S; 13R

	Nd isotope						
isotope	142[2]	143[3]	144	145	146	148	150
nucleosynthetic pathway	4P; 96S	35S; 65R	53S; 47R	29S; 71R	63S; 37R	8S; 92R	100R

	Sm isotope						
isotope	144	147	148	149	150	152	154
nucleosynthetic pathway	100P	20S; 80R	100S	12S; 88R	100S	23S; 77R	100R

1 radiogenic interference from ^{138}La decay
2 radiogenic interference from ^{146}Sm decay
3 radiogenic interference from ^{147}Sm decay

Previous work on refractory inclusions and various bulk carbonaceous chondrites (and their leachates) has shown excesses in the isotopes of Ba that include significant *r*-process contributions (^{135}Ba and ^{137}Ba) (Harper et al., 1992; Hidaka et al., 2003; Ranen and Jacobsen, 2006; Carlson et al., 2007; Andreasen and Sharma, 2007; Bermingham et al., 2010; Carlson et al., 2010). Other studies have shown *p*-process depletions in Sm and Nd isotopic signatures of bulk carbonaceous chondrites (Andreasen and Sharma, 2006; Carlson et al., 2007; Andreasen and Sharma, 2007; Carlson et al., 2010). Large isotopic anomalies have been reported for Ba, Nd, and Sm in EK1-4-1 and C1, CAIs with fractionation and unidentified nuclear isotope anomalies, or “FUN” CAIs (McCulloch and Wasserburg 1978a; 1978b), but no work has been published Nd and Sm isotope compositions of non-FUN CAIs. This study presents the Ba, Nd, and Sm isotope compositions of eleven Allende CAIs (non-FUN) for which uranium isotope compositions were previously reported (Brennecka et al., 2010).

A.2 MATERIALS AND METHODS

Aliquots from previously dissolved calcium-aluminum-rich inclusions (CAIs) of the Allende meteorite (from which U was separated, as described in (Brennecka et al., 2010)) were processed for Ba, Nd, and Sm isotope measurements. This sample set includes three group II CAIs (CAI 166, 167, 175), as discussed in Brennecka et al. (2010). Barium was separated from the CAI matrix and interfering elements using AG50W-X8 cation exchange resin, following the procedure outlined in Carlson et al. (2007). Nd and Sm were separated from the CAI matrix in a light rare earth element cut in the same column procedure. Complete separation of Nd and Sm from one another (as well as separation from other isobaric interferences) was accomplished using multiple passes through methalactic acid column chemistry.

A separate, unprocessed aliquot of each CAI was spiked with a mixed ^{150}Nd-^{149}Sm spike to obtain very precise Sm/Nd ratios with isotope dilution. The isotope dilution samples were put through the same cation exchange chemistry described above. The light rare earth element cut was then put through LN spec resin to separate the measured isotopes of Nd from Sm. The Nd and Sm cuts from the LN spec chemistry were measured separately at Lawrence Livermore National Laboratory (LLNL) using modified versions of discussed procedures for Nd and Sm isotope measurement. This isotope dilution procedure reduces uncertainty on the ^{147}Sm/^{144}Nd to approximately 0.1%.

The Ba, Nd and Sm isotopic compositions of the samples and standards were measured on a Thermo-Finnigan Triton thermal ionization mass spectrometer (TIMS) at LLNL. Internal normalization was used for correction of instrumental mass bias for all three isotope systems. All samples were run interspersed with standards, with the external reproducibility of the standards recorded as the lowest possible reported uncertainty. Isobaric interferences for Ba, Nd, Sm were monitored and corrected for during runs of all samples and standards.

A.2.1 Barium Isotopic Measurement

When sample size allowed, runs consisted of 300 ratios with 16 second integrations. Barium was analyzed on zone refined double Re filaments and loaded directly on the evaporation filament for measurement. All voltages were measured during a single static run utilizing 10^{11} ohm resistors to measure ^{134}Ba, ^{135}Ba, ^{136}Ba, ^{137}Ba, ^{138}Ba, and ^{140}Ce. To increase the signal, 10^{12} ohm resistors were used to measure ^{130}Ba, ^{132}Ba, and ^{139}La. Data are normalized to ^{136}Ba and fractionation corrected to ^{134}Ba/^{136}Ba = 0.3078 using the exponential law. This normalization was chosen because ^{134}Ba and ^{136}Ba are *s*-process only isotopes, effectively normalizing out the *s*-process component.

A.2.2 Neodymium Isotopic Measurement

Neodymium was analyzed on double Re filaments as Nd+ using a two mass step procedure that calculates ^{142}Nd/^{144}Nd dynamically, utilizing 10^{12} ohm resistors to measure the voltages of the possible interfering isotopes ^{140}Ce, ^{141}Pr, ^{147}Sm, and ^{149}Sm. Both steps of the dynamic run used 8 second integration times for 540 ratios, when sample size allowed. Data are normalized to ^{144}Nd and fractionation corrected to ^{146}Nd/^{144}Nd = 0.7219 using the exponential law.

A.2.3 Samarium Isotopic Measurement

Samarium was measured on double Re filaments, where normal runs consisted of 300 ratios at 8 second integrations. All isotopes of Sm were measured during a single static run, utilizing 10^{12} ohm resistors to monitor ^{146}Nd and ^{155}Gd for potential interference corrections. Isotopes of Sm are normalized to ^{150}Sm and fractionation corrected to ^{148}Sm/^{150}Sm = 1.523370. This normalization was chosen because ^{148}Sm and ^{150}Sm are *s*-process only isotopes, effectively normalizing out the *s*-process component, analogous to Ba. Because ^{149}Sm has an extremely large neutron capture cross section which could potentially create artificial excesses in the normalizing isotope ^{150}Sm, a second normalization was performed, normalizing to ^{152}Sm with a fractionation correction of ^{147}Sm/^{152}Sm =

0.56081. Both normalizations use the exponential law for fractionation correction.

A.3 RESULTS

The data indicate that the non-radiogenic isotopes of Ba, Nd and Sm of Allende CAIs are not statistically different, and are treated as such in the following sections. Measurements from all samples and standards are given in Tables A.2 through A.4.

A.3.1 Barium Isotopes

Relative to a terrestrial ICP standard, CAIs of Allende show an average excess of 0.55 ± 0.10 ε in $^{135}Ba/^{136}Ba$ and an average excess of 0.18 ± 0.09 ε in $^{137}Ba/^{136}Ba$, representing apparent *r*-process excesses in Ba. These averages include ten of the eleven CAIs, excluding CAI 167, for which very poor stability during the analyses may have compromised the accuracy of the data for this sample. The $^{138}Ba/^{136}Ba$ values of samples of this study are highly variable due to differences in the La/Ba ratios and the decay of ^{138}La, discussed in detail in section A.4.1. The excess ^{138}Ba produced by radiogenic ingrowth from ^{138}La has been subtracted in Figure A.1. No resolvable deviations exist from the terrestrial standard in $^{130}Ba/^{136}Ba$ or in $^{132}Ba/^{136}Ba$, although the low isotopic abundances of ^{130}Ba and ^{132}Ba greatly increase the size of the analytical uncertainty. The average isotopic compositions are shown, along with the percent of nucleosynthetic creation of each isotope in Figure A.1. All values are shown in Table A.2.

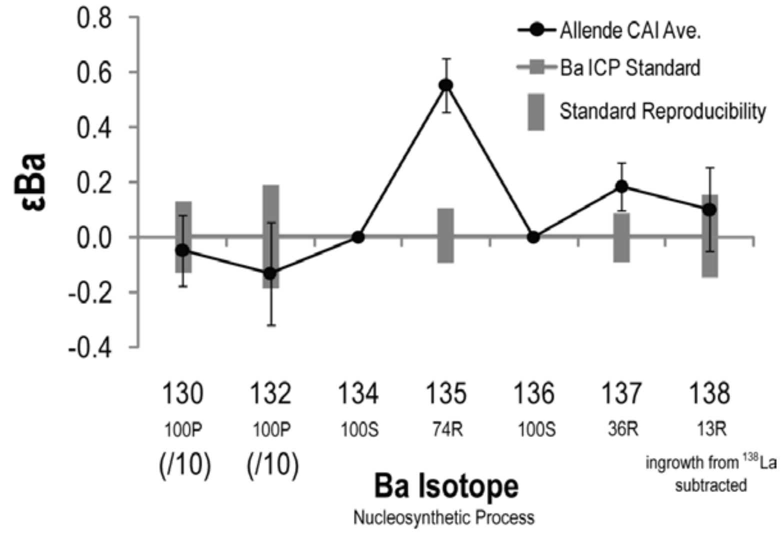

Figure A.1. The average Ba isotopic composition Allende CAIs is shown with the solid black line. Uncertainties are shown as 2SD as the reproducibility of the Ba ICP standard. The values and uncertainties of ^{130}Ba and ^{132}Ba are divided by 10 to fit on the same scale. The percent of one nucleosynthetic process for creation of that isotope is included under each isotope number (e.g., 74% of ^{135}Ba is created by the *r*-process). The calculated ingrowth of ^{138}Ba from the decay of ^{138}La is subtracted as shown in this figure based on measured La/Ba ratios, reported in Table A.2 and discussed in section A.4.1.

A.3.2 Neodymium Isotopes

The Nd isotopic data for the Allende CAIs are shown relative to the JNdi terrestrial standard (Figure A.2). Data for ^{142}Nd and ^{143}Nd contain significant radiogenic components from the decay of ^{146}Sm and ^{147}Sm, respectively, and are not shown in Figure A.2. All CAIs display apparent deficits in the predominately *r*-process isotopes, with the average values: ^{145}Nd/^{144}Nd = -0.23±0.09 ε, ^{148}Nd/^{144}Nd = -0.29±0.12 ε, ^{150}Nd/^{144}Nd = -0.64±0.17 ε. All data is shown in Table A.3.

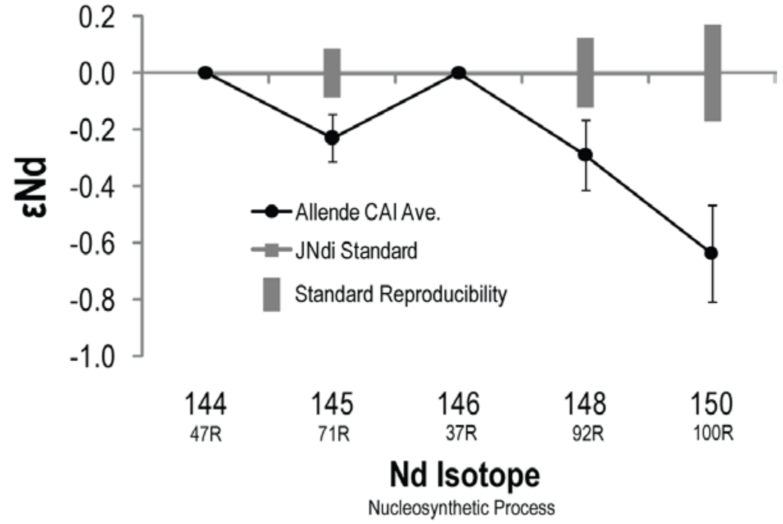

Figure A.2. The average Nd isotopic composition Allende CAIs is shown with the solid black line. Uncertainties are shown as 2SD as the reproducibility of the JNdi standard. ^{142}Nd and ^{143}Nd are not shown because of the large amount of radiogenic input from ^{146}Sm and ^{147}Sm, respectively. The percent of one nucleosynthetic process for creation of that isotope is included under each isotope number.

A.3.3 Samarium Isotopes

The Sm isotopic data are shown relative to the AMES terrestrial std. (Figure A.3). The *p*-process only isotope ^{144}Sm shows an apparent deficit

(^{144}Sm/^{150}Sm = -1.97±0.49 ε), along with the predominantly *r*-process isotopes that also show apparent deficits: ^{147}Sm/^{150}Sm = -0.35±0.17 ε, ^{149}Sm/^{150}Sm = -1.10±0.11 ε, ^{152}Sm/^{150}Sm = -1.57±0.28 ε, ^{154}Sm/^{150}Sm = -2.22±0.44 ε. All data is shown in Table A.4.

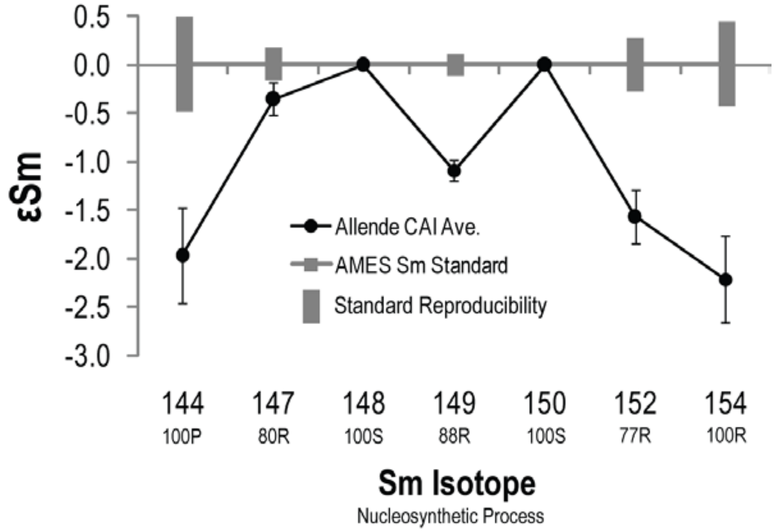

Figure A.3. The average Sm isotopic composition Allende CAIs is shown with the solid black line. Uncertainties are shown as 2SD as the reproducibility of the AMES Sm standard. The percent of one nucleosynthetic process for creation of that isotope is included under each isotope number.

Table A.2. The Ba isotopic compositions and La/Ba ratios of all samples of this study.

						Normalized to					
Sample	number of Ratios	N	volts ^{136}Ba	^{130}Ba/^{136}Ba	^{132}Ba/^{136}Ba	^{134}Ba/^{136}Ba	^{135}Ba/^{136}Ba	^{137}Ba/^{136}Ba	^{138}Ba/^{136}Ba	^{139}La/^{136}Ba	^{140}Ce/^{136}Ba
Ba ICP Standard Ave.	300	9	12.2	0.013486	0.012903	**0.3078**	0.839346	1.429021	9.128734	8.78526E-06	8.68177E-06
2SD				0.000002	0.000002	-	0.000008	0.000012	0.000140	-	-
CAI 164-1	200		10.9	0.013486	0.012901	**0.3078**	0.839393	1.429045	9.128949	3.77E-07	8.63E-07
CAI 164a-1	220		12.7	0.013485	0.012900	**0.3078**	0.839398	1.429036	9.128842	1.93E-06	2.24E-06
CAI 164a-2	260		13.4	0.013484	0.012900	**0.3078**	0.839397	1.429043	9.128940	2.60E-06	8.38E-07
CAI 165-1	300		10.6	0.013485	0.012901	**0.3078**	0.839389	1.429051	9.128883	2.32E-06	-2.03E-06
CAI 165-2	126		11.8	0.013486	0.012903	**0.3078**	0.839398	1.429053	9.128847	2.20E-06	-1.45E-07
CAI 166-1	200		12.4	0.013487	0.012902	**0.3078**	0.839391	1.429041	9.129075	5.63E-06	7.18E-05
CAI 166-2	260		11.8	0.013486	0.012902	**0.3078**	0.839388	1.429048	9.129160	4.77E-06	3.29E-05
CAI 167-1	111		10.7	0.013486	0.012900	**0.3078**	0.839350	1.429022	9.129027	2.61E-06	5.73E-06
CAI 167a-1	260		10.5	0.013485	0.012902	**0.3078**	0.839353	1.429025	9.129080	2.40E-06	2.55E-07
CAI 168-1	220		11.7	0.013484	0.012902	**0.3078**	0.839391	1.429044	9.128820	1.61E-06	4.15E-07
CAI 168a-1	160		11.1	0.013486	0.012901	**0.3078**	0.839397	1.429046	9.128924	7.24E-06	5.22E-06
CAI 170-1	220		12.0	0.013484	0.012901	**0.3078**	0.839394	1.429040	9.128746	4.55E-06	2.43E-05
CAI 170a-1	240		11.7	0.013485	0.012901	**0.3078**	0.839391	1.429033	9.128641	5.02E-06	6.52E-06
CAI 171-1	400		10.4	0.013486	0.012901	**0.3078**	0.839401	1.429043	9.128740	1.96E-06	1.77E-06
CAI 171-2	400		10.5	0.013486	0.012902	**0.3078**	0.839393	1.429034	9.128761	-9.24E-07	1.18E-05
CAI 172-1	360		11.8	0.013485	0.012902	**0.3078**	0.839394	1.429061	9.128996	3.87E-06	1.14E-03
CAI 172-2	400		12.7	0.013484	0.012901	**0.3078**	0.839392	1.429063	9.128974	4.44E-06	3.34E-04
CAI 172a-1	240		10.8	0.013483	0.012900	**0.3078**	0.839400	1.429066	9.129061	2.77E-06	7.07E-07
CAI 172a-2	300		10.8	0.013487	0.012901	**0.3078**	0.839401	1.429054	9.128910	1.07E-06	-1.37E-06
CAI 172a-3	200		13.6	0.013486	0.012901	**0.3078**	0.839390	1.429054	9.129072	2.49E-06	1.21E-06
CAI 173-1	400		11.7	0.013486	0.012900	**0.3078**	0.839383	1.429040	9.128895	3.28E-06	1.51E-05
CAI 173-2	400		10.0	0.013486	0.012902	**0.3078**	0.839387	1.429038	9.128802	2.86E-06	1.84E-05
CAI 174-1	200		11.7	0.013485	0.012901	**0.3078**	0.839388	1.429063	9.129028	2.93E-05	7.80E-05
CAI 174-2	200		13.2	0.013485	0.012901	**0.3078**	0.839390	1.429040	9.128854	2.32E-05	6.62E-05
CAI 174a-1	300		14.0	0.013485	0.012902	**0.3078**	0.839393	1.429048	9.128873	2.42E-06	3.88E-07
CAI 174a-2	300		10.1	0.013486	0.012902	**0.3078**	0.839391	1.429046	9.128803	4.01E-06	1.98E-06
CAI 175-1	201		11.7	0.013485	0.012904	**0.3078**	0.839388	1.429048	9.129130	8.75E-05	1.52E-04
CAI 175-2	200		9.8	0.013486	0.012902	**0.3078**	0.839395	1.429035	9.128955	7.54E-05	2.90E-04
CAI 175a-1	200		10.7	0.013487	0.012904	**0.3078**	0.839386	1.429059	9.129149	3.04E-06	-2.47E-06
CAI 175a-2	200		10.4	0.013486	0.012902	**0.3078**	0.839386	1.429050	9.129237	7.80E-06	1.11E-05
Ave				0.013485	0.012901		0.839390	1.429046	9.128939		
εBa				-0.50	-1.37		0.52	0.17	0.22		
2SD				1.28	1.87		0.10	0.09	0.15		

	La/Ba
Bulk Earth	0.098
CAI 164	0.108
CAI 165	0.163
CAI 166	1.596
CAI 167	1.398
CAI 168	0.085
CAI 170	0.090
CAI 171	0.088
CAI 172	0.086
CAI 173	0.314
CAI 174	0.080
CAI 175	1.507

Table A.3. The Nd isotopic compositions and $^{147}Sm/^{144}Nd$ ratios of all samples of this study.

Sample	Ratios	N	volts ^{144}Nd	$^{142}Nd/^{144}Nd$	$^{143}Nd/^{144}Nd$	Normalized to $^{146}Nd/^{144}Nd$	$^{145}Nd/^{144}Nd$	$^{148}Nd/^{144}Nd$	$^{150}Nd/^{144}Nd$	$^{140}Ce/^{144}Nd$	$^{141}Pr/^{144}Nd$	$^{149}Sm/^{144}Nd$	After Chem $^{147}Sm/^{144}Nd$	Before Chem. $^{147}Sm/^{144}Nd$
JNdi Ave.	540	8	3.9	1.141834	0.512098	0.7219	0.348402	0.241579	0.236455	1.79E-06	3.37E-05	2.81E-06	3.23E-06	-
2SD				0.000008	0.000004	-	0.000003	0.000003	0.000004	-	-	-	-	-
Sample														
CAI 164	270		2.9	1.141841	0.512748	**0.7219**	0.348393	0.241573	0.236439	2.89E-05	6.60E-05	1.13E-06	1.47E-06	0.202
CAI 165	540		3.1	1.141797	0.512279	**0.7219**	0.348393	0.241569	0.236435	1.47E-05	4.43E-05	4.07E-07	4.93E-07	0.187
CAI 166	540		3.9	1.141806	0.512475	**0.7219**	0.348394	0.241571	0.236433	2.50E-05	2.21E-05	2.43E-07	3.41E-07	0.196
CAI 167	540		3.9	1.141807	0.512463	**0.7219**	0.348394	0.241570	0.236438	4.46E-05	2.68E-05	5.05E-07	4.69E-07	0.192
CAI 168	150		3.9	1.141834	0.512607	**0.7219**	0.348396	0.241576	0.236447	1.36E-04	6.06E-05	7.62E-07	1.05E-06	0.198
CAI 170	460		3.6	1.141830	0.512606	**0.7219**	0.348394	0.241573	0.236442	2.96E-04	9.44E-05	3.23E-07	5.56E-07	0.196
CAI 171	145		3.3	1.141834	0.512526	**0.7219**	0.348395	0.241576	0.236444	2.37E-04	9.22E-05	1.08E-06	3.88E-07	0.193
CAI 172	420		3.6	1.141830	0.512711	**0.7219**	0.348395	0.241575	0.236446	2.08E-04	5.62E-05	5.26E-07	5.44E-07	0.199
CAI 173	540		3.8	1.141817	0.512527	**0.7219**	0.348394	0.241572	0.236437	3.46E-05	3.03E-05	6.88E-07	7.25E-07	0.192
CAI 174	314		3.7	1.141822	0.512614	**0.7219**	0.348390	0.241571	0.236437	1.21E-04	4.39E-05	3.88E-07	8.95E-07	0.194
CAI 175	540		3.5	1.141759	0.511557	**0.7219**	0.348393	0.241572	0.236438	2.44E-05	2.30E-05	3.36E-07	6.57E-07	0.162
Ave							0.348394	0.241572	0.236440					
εNd							-0.23	-0.29	-0.64					
2SD							0.09	0.12	0.17					

Table A.4. The Sm isotopic compositions of all samples of this study.

						Normalized to					
Sample	Ratios	N	volts ^{144}Sm	^{144}Sm/^{150}Sm	^{147}Sm/^{150}Sm	**^{148}Sm/^{150}Sm**	^{149}Sm/^{150}Sm	^{152}Sm/^{150}Sm	^{154}Sm/^{150}Sm	^{146}Nd/^{150}Sm	^{155}Gd/^{150}Sm
Ames Sm Ave.	300	10	0.20	0.416583	2.031957	1.523370	1.872696	3.623281	3.082655	3.00E-04	9.56E-05
				0.000021	0.000034	-	0.000020	0.000100	0.000136	-	-
CAI 164	200		0.25	0.416518	2.031919	**1.523370**	1.872474	3.622616	3.081816	6.29E-04	3.08E-04
CAI 165	300		0.20	0.416490	2.031893	**1.523370**	1.872526	3.622824	3.082075	5.12E-04	2.01E-04
CAI 166	300		0.23	0.416501	2.031884	**1.523370**	1.872479	3.622676	3.081947	2.18E-04	1.47E-04
CAI 167	300		0.22	0.416507	2.031873	**1.523370**	1.872479	3.622687	3.081990	1.65E-04	1.59E-04
CAI 168	300		0.18	0.416522	2.031891	**1.523370**	1.872423	3.622551	3.081798	4.34E-04	1.87E-04
CAI 170	300		0.23	0.416504	2.031885	**1.523370**	1.872513	3.622736	3.081987	5.74E-04	1.99E-04
CAI 171	100		0.22	0.416514	2.031872	**1.523370**	1.872452	3.622680	3.081970	7.39E-04	3.70E-04
CAI 172	300		0.24	0.416494	2.031877	**1.523370**	1.872519	3.622778	3.082046	4.00E-04	2.89E-04
CAI 173	300		0.19	0.416494	2.031882	**1.523370**	1.872506	3.622774	3.082035	2.76E-04	1.98E-04
CAI 174	300		0.24	0.416489	2.031884	**1.523370**	1.872526	3.622813	3.082083	3.77E-04	1.22E-04
CAI 175-1	300		0.23	0.416491	2.031879	**1.523370**	1.872491	3.622709	3.081953	3.07E-04	2.43E-04
CAI 175-2	300		0.24	0.416490	2.031888	**1.523370**	1.872502	3.622722	3.081957	2.08E-04	1.10E-04
Ave				0.416501	2.031885		1.872491	3.622714	3.081971		
εSm				-1.97	-0.35		-1.10	-1.57	-2.22		
2SD				0.49	0.17		0.11	0.28	0.44		

A.4 DISCUSSION

A.4.1 Evidence of ^{138}La decay to ^{138}Ba

Lanthanum-138 comprises less than 0.1% of all La, and has a half-life of ~105 Ga. Decay of ^{138}La is branched between ^{138}Ce (33.6%) and ^{138}Ba (66.4%). The long half-life of ^{138}La requires a significant range of La/Ba ratios in various samples to detect ingrowth of ^{138}Ba from ^{138}La. Group-II CAIs have experienced a complex thermal history, resulting in a large elemental fractionation of Ba from La. In this sample set, which includes three group II CAIs, the La/Ba ratio ranges from as low as ~0.08 (in non-group-II CAIs) up to ~1.6 (in group-II CAIs). Based on the half-life of ^{138}La and this range of La/Ba ratios, a ~0.3ε difference in ^{138}Ba should be present in between group II and non-group II CAIs. These data are shown in Fig. A.1 for one group II and one non-group II and isotopic and elemental ratio data for all samples is shown in Table A.1. The group II samples (CAI 166, CAI 167, and CAI 175) all have excesses in ^{138}Ba of ~0.3ε in when compared to the non-group II samples. These data provide the first evidence for the decay of ^{138}La in refractory inclusions and indicate the possibility of further development of a ^{138}La-^{138}Ba chronometer for early Solar System materials.

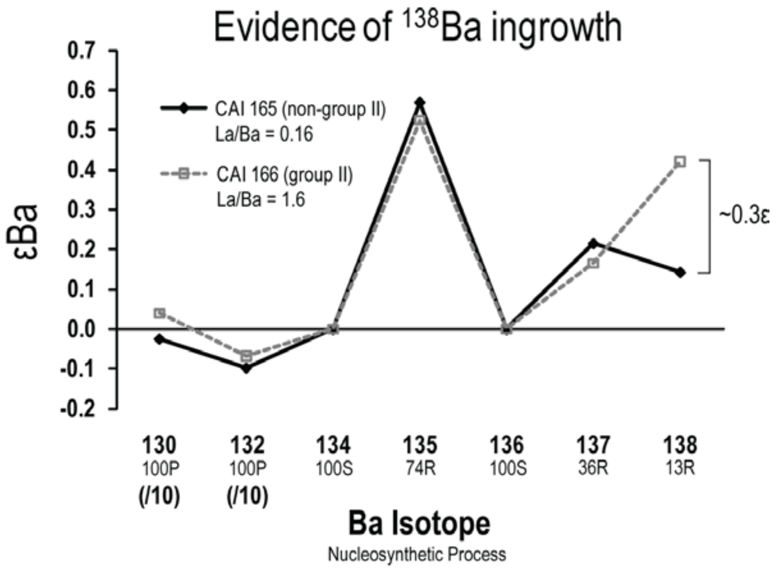

Figure A.4. Evidence of ^{138}Ba ingrowth from the decay of ^{138}La. The decay of ^{138}La to ^{138}Ba causes a measurable change the isotopic composition at ^{138}Ba and is measurable due to the extreme differences in the La/Ba ratios of samples of this study. For figure clarity, the analytical uncertainties are removed and the Ba isotopic patterns of only one non-group II (CAI 165, solid black line) and one group II CAI (CAI 166, dashed grey line) are shown.

A.4.2 Comparison to previous isotopic data

The data show clear excesses in those Ba isotopes that have a significant *r*-process component (^{135}Ba and ^{137}Ba). These apparent *r*-process excesses are consistent with previous work on refractory inclusions (Harper et al., 1992; Bermingham et al., 2010), but slightly higher than reported values for bulk chondrites (Hidaka et al., 2003; Ranen and Jacobsen, 2006; Carlson et al., 2007; Andreasen and Sharma, 2007). Similarly, the reported negative anomalies in the *p*-process isotope ^{144}Sm of this study are significantly larger than those previously reported for bulk chondrites (Andreasen and Sharma, 2006). These data indicate that the Ba, Nd and Sm nucleosynthetic anomalies in CAIs could be largely, if not entirely, responsible for the previously reported anomalies in bulk carbonaceous chondrites.

A.4.3 Evidence of extant ^{135}Cs?

Cesium-135 is a short-lived radionuclide that decays to ^{135}Ba with a half-life of ~2.3Ma. Previous workers have suggested that the anomalies in ^{135}Ba could be caused by the decay of the ^{135}Cs in the early Solar System (Harper et al., 1992; Hidaka et al. 2001; Bermingham et al. 2010). Due to differences in volatility of Cs and Ba, the Cs/Ba ratio of CAIs is lower than bulk chondrites (Hidaka et al. 2001). As the ^{135}Ba anomalies found in Allende CAIs are generally larger than those reported for bulk Allende, the cause of ^{135}Ba anomalies cannot be from the decay of the short-lived ^{135}Cs to ^{135}Ba. Additionally, while the Cs/Ba ratios of the samples of this study were not measured, the variety of CAIs sampled (i.e., group II v. non-group II) would produce large differences in the Cs/Ba ratio of these CAIs. However, the ^{135}Ba anomaly in CAIs is consistent, suggesting that the decay of ^{135}Cs is not the cause of the excess ^{135}Ba.

A.4.4 Origin of isotopic anomalies in CAIs?

At least two isotopically distinct reservoirs were present in the early Solar System: the reservoir from which CAIs formed, and the reservoir that provided material for all other bulk meteorites and Earth. These data clearly show that apparent *r*-process *excesses* in Ba isotopes are preserved along with apparent *p*- and *r*-process *deficits* in Nd and Sm isotopes in the exact same samples. Thus, an explanation is required for how relative *r*-process excesses in one isotope system (Ba) are recorded along with relative *r*-process deficits in other isotope systems (Nd and Sm) in CAIs. Central to this explanation must be the mechanism of how the nucleosynthetic signatures preserved in CAIs relate to the average "bulk Solar System". The following sections will address the plausibility of a few potential scenarios that can be called upon to explain the existence of such data.

A.4.4.1 Mixing of FUN or presolar components

Previous studies have reported the Ba, Nd, and Sm isotopic compositions of the FUN CAIs, EK1-4-1 and C1 (McCulloch and Wasserburg 1978a; 1978b). These values are not only vastly different from bulk meteorites, but they are also vastly different from one other, suggesting that FUN CAIs are not formed from a homogeneous reservoir. The sample EK1-4-1 shows large apparent *r*-process excesses in Ba, Nd and Sm, where sample C1 is isotopically normal except for very small deficits in ^{135}Ba and excesses in ^{144}Sm. Other previous studies have reported the Ba, Nd, and Sm isotopic composition of silicon carbide (SiC) presolar grains (Hoppe and Ott, 1997), which show huge apparent *p*- and *r*-process deficits, indicative of an AGB signature. Interestingly, when the data is displayed for both SiC and the FUN inclusion EK1-4-1, the isotopic signatures are mirror images of one another, however at much different scales. This is shown for Ba, Nd, and Sm in Figure A.5.

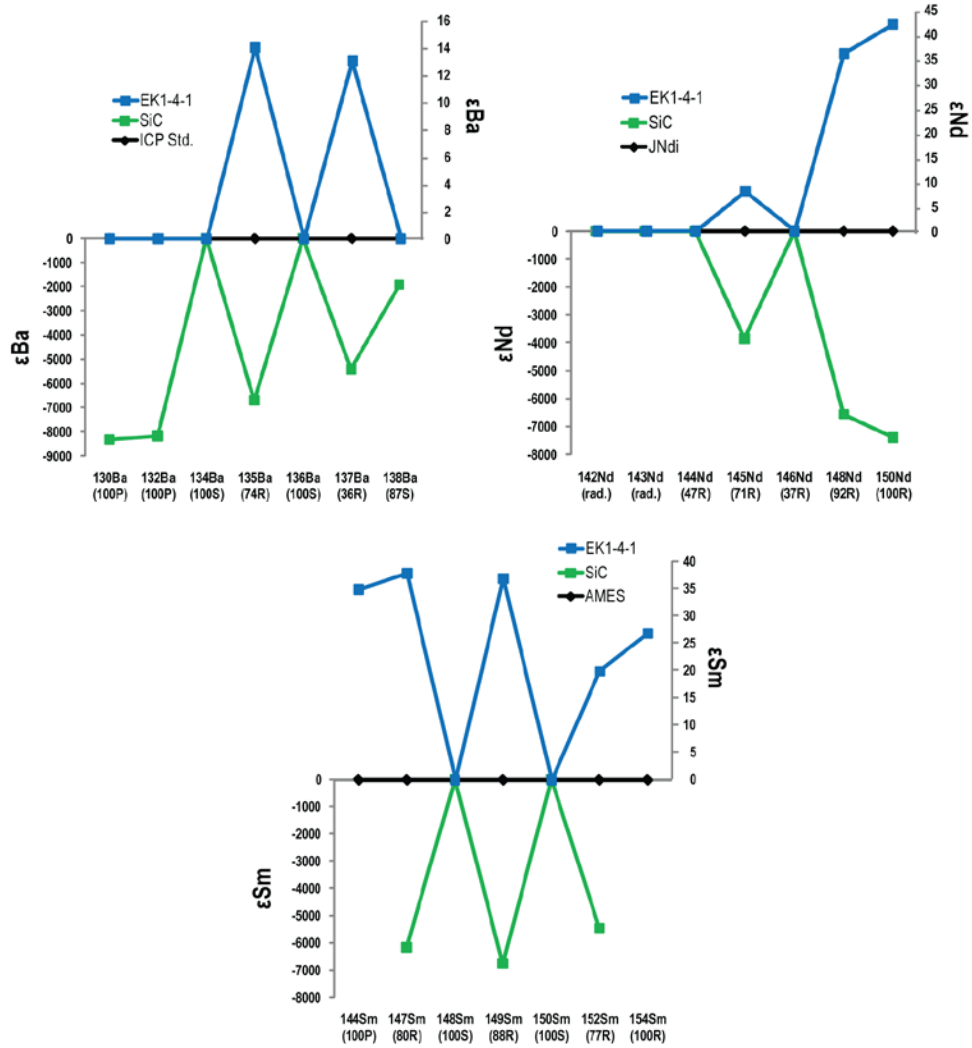

Figure A.5. Ba, Nd, and Sm isotopic signatures of SiC grains and the FUN inclusion EK1-4-1. SiC data is renormalized from Hoppe and Ott (1997), and EK1-4-1 data is renormalized from McCulloch and Wasserburg (1978a; 1978b). Note the vastly different scales at which the values for the materials are plotted.

In principle, incorporation of a mix of the isotopic signatures of EK1-4-1, SiC and bulk Solar System material could produce the isotopic signatures seen in Allende CAIs. However, producing apparent *r*-process excesses in Ba and apparent *r*-process deficits in Nd and Sm would require the concentrations of Ba from Nd and Sm in SiC grains to be vastly different. While the trace element abundances and Ba, Nd, and Sm isotopic signatures are unknown for presolar grains other than SiC, work by Amari et al. (1995) indicates that the abundance of Ba and REEs are approximately the same in SiC grains. In addition, this study includes fine grained, coarse grained, group-II and non-group-II CAIs, requiring that the amount of presolar, FUN and bulk Solar System components mixed into each of these groups must be in the same proportions for all types of CAIs measured. Moreover, since FUN CAIs have vastly different isotopic signatures, a mixing scenario resulting in isotopically homogeneous CAIs becomes even less plausible.

A.4.4.2 Incomplete digestion of sample materials

If the isotopic composition of extremely refractory phases, such as SiC grains, were markedly different from that of the rest of the sample, incomplete digestion of any sample could potentially affect the reported isotopic values. The particular issue of undissolved presolar grains was addressed for the Ba isotopic composition of bulk meteorites by Andreason and Sharma (2007). They concluded that, if ~14 ppm of SiC was left undissolved in a meteorite, it could produce the observed Ba isotopic signature, within error, of that seen in Allende and Murchison. However, two major problems exist with this explanation: first, the SiC abundance in Allende is less than 10 ppb (Huss & Lewis 1995), about 3 orders of magnitude lower than the SiC abundance in Murchison (Tizard et al.

2005). If undissolved SiC was the primary cause for Ba isotopic anomalies in Allende and Murchison, the two meteorites should have vastly different Ba isotopic compositions due to their differences in SiC concentrations. However, the Ba isotope compositions of bulk Allende and bulk Murchison are the same (Andreason and Sharma, 2007). Secondly, if undissolved SiC grains were causing the isotopic anomalies in bulk Allende and Murchison, a similar *r*-process signature should be present in Nd and Sm, which it is not (Andreason and Sharma, 2006).

Similar to bulk chrondrites, incomplete digestion of CAIs causing isotopic anomalies would require that an extremely refractory phase similar to presolar grains with a vastly different isotopic composition from the rest of the CAI was present at the same ratios in group-II, non-group II, coarse- and fine-grained samples, and left undissolved at exactly the same proportion in all types of CAIs of this study. First, no such materials are known to exist in CAIs. Secondly, that unknown refractory material would have to carry different ratios of Ba and REEs with distinct nucleosynthetic inputs. Thirdly, the same unknown refractory material would have had to be present in the same proportion and left undissolved in the same proportion in all other CAI and bulk chondrite studies to provide the same isotopic patterns seen in this study. These multiple lines of evidence make incomplete digestion of CAIs a very unlikely cause of the isotopic anomalies present in Allende CAIs.

A.4.4.3 Neutron capture and the improper normalization of isotopes

The interaction of thermal neutrons with Solar System material has the potential to measurably change the isotopic composition of that material. The likelihood of this occurrence is higher in the case of Sm, for which the thermal neutron capture cross-section for ^{149}Sm is extraordinarily large (~41,500 barns) and consequently has been shown in numerous studies to produce deficits in ^{149}Sm (and corresponding excesses in ^{150}Sm) based on various neutron fluxes (Hidaka et al., 2000, references therein). If measurable anomalies were present in ^{149}Sm and ^{150}Sm from neutron capture in CAIs, internal normalization using the *s*-process only isotopes ^{148}Sm and ^{150}Sm would be problematic. Therefore, a second internal normalization unaffected by neutron capture using ^{147}Sm and ^{152}Sm is shown below in Figure A.6.

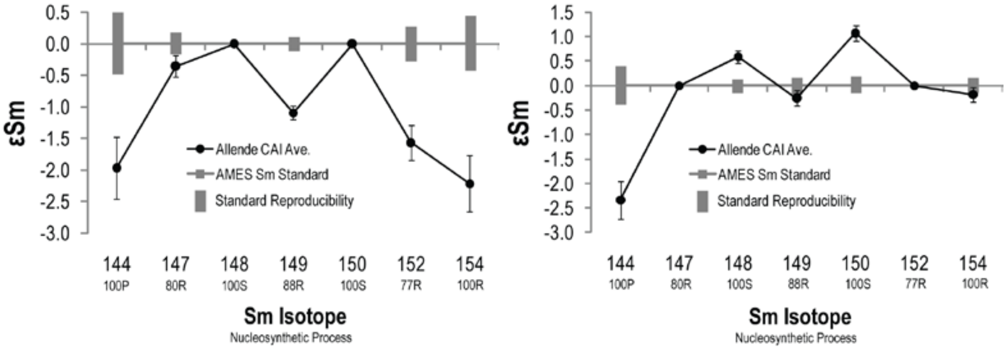

Figure A.6. Sm isotope data shown using two separate normalizations. One normalizations using ^{148}Sm:^{150}Sm is shown on the left. The same data normalized to ^{147}Sm:^{152}Sm is shown on the right.

Regardless of how the data is normalized, deviations from the terrestrial standard are clear and cannot be explained simply by neutron capture processes. Additionally, using this data, it is possible to determine if neutron capture has had a significant effect on these CAIs. For every ^{149}Sm that captures a neutron, a ^{150}Sm is created. Therefore, if neutron capture processes caused depletions in ^{149}Sm and excesses in ^{150}Sm in Allende CAIs, these anomalies should be correlated, as plotted in Figure A.7.

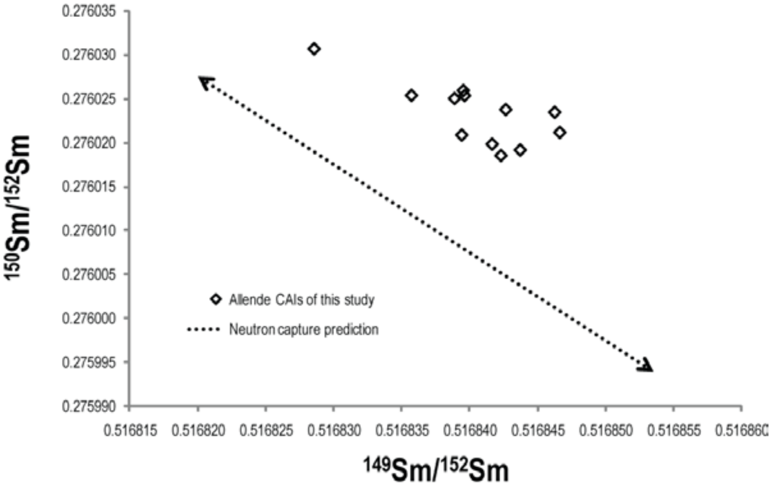

Figure A.7. Predicted neutron capture correlation for ^{149}Sm and ^{150}Sm. CAIs of this study are shown as hollow diamonds, with the predicted neutron capture line shown with a dotted line.

Allende CAIs fall well off the predicted 1:1 neutron capture line and fail to form a defined line. This strongly suggests the ^{148}Sm:^{150}Sm normalization is appropriate for this study and the isotopic anomalies in CAIs are not created by neutron capture processes. The neutron capture cross section of ^{149}Sm is approximately 100 times larger than any other isotope in this study, therefore neutron capture effects cannot explain the anomalies seen in other isotope systems.

A.4.4.4 Nuclear field shift fractionation

Traditionally, isotope geochemists usually explain isotopic deviations of samples from standards in one of three ways: 1) radioactive decay 2) mass-dependent fractionation, or 3) nucleosynthetic anomalies. However, mass-independent isotope fractionation has provided explanations to some very intriguing data sets (e.g., photochemical dissociation of carbon monoxide in the solar nebula explaining oxygen isotope variations) and may play a larger role than previously recognized in other data sets. This work explores the possibility that isotopic anomalies of multiple elements in Allende CAIs may be caused by mass-independent isotope fractionation induced by the nuclear field shift. Isotope fractionation by the nuclear field shift is caused by preferential behavior of isotopes in chemical reactions because of differences in the size, shape and charge between nuclei (Bigeleisen 1996). A number of experiments involving multiple isotopes systems have confirmed the existence of mass-independent fractionation as predicted by the nuclear field shift effect (Moynier et al. 2009b, references therein), and these fractionation patterns can be predicted based on differences in the mean-squared nuclear charge radii between isotopes. The interaction of CAIs with the nebular gas during the early stages of condensation is one possible location in which nuclear field shift fractionation could have taken place in these samples (Moynier et al. 2009a), and the predicted isotope patterns for Ba, Nd, Sm, Mo, Ni, and Te in Allende CAIs can be calculated.

Mass-independent isotope effects are calculated in ε units (parts per 10,000) using the following equation (for full derivation see Fujii et al. 2006).

$$\varepsilon_{mi} = \left(\delta\langle r^2\rangle_{m1,mi} - \frac{m_2(m_i - m_1)}{m_i(m_2 - m_1)} \times \delta\langle r^2\rangle_{m1,m2}\right) \times a$$

In this equation, m_1 and m_2 stand for the atomic masses of the nuclides chosen for internal normalization, and m_i represents the atomic mass of a nuclide indexed with the variable "*i*". Differences in mean-squared nuclear charge radii, $\delta\langle r^2\rangle$, of each isotope pair are taken from Aufmuth et al. (1987). These data, along with the measured ε values of the samples are combined into the equation above, leaving the parameter "*a*" to be determined by regression. The variable "*a*" is an adjustable parameter depending on temperature T as 1/T and represents the overall extent of mass-independent fractionation (Fujii et al. 2006). Data from this study (Figures A.8 through A.10) and literature data from other Allende CAIs (Figures A.11 through A.13) are shown along the isotope fractionation patterns predicted by the nuclear field shift effect at an optimized value of "*a*" for each element. Uncertainties for the calculated data are given as the ranges obtained by using the nuclear charge radii literature values of Heilig and Steudel (1974); Aufmuth (1984); and Angeli (2004).

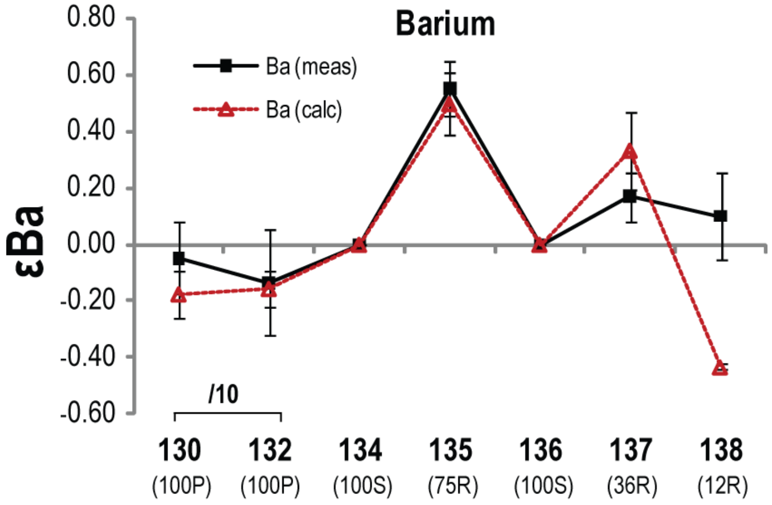

Figure A.8. Barium nuclear field shift effects. The average Ba isotopic data from Allende CAIs is shown with the solid black line. The calculated nuclear field shift effect is shown using a dotted red line. The best-fit to the data for Ba is found using *a* = -15.

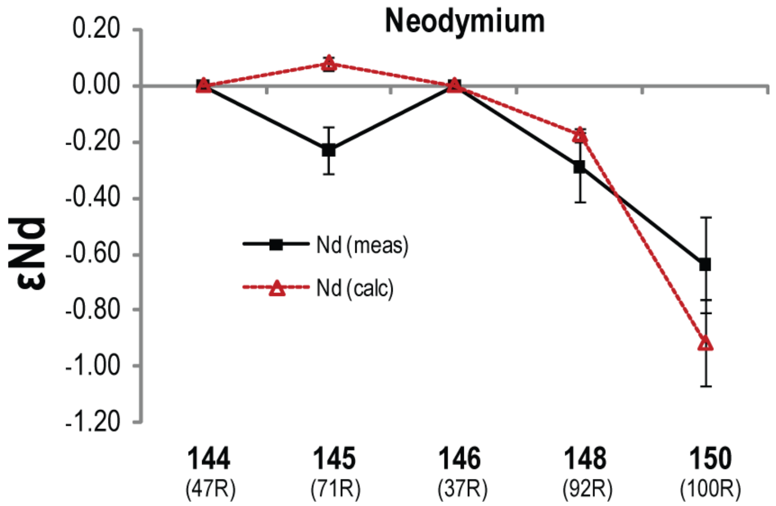

Figure A.9. Neodymium nuclear field shift effects. The average Nd isotopic data from Allende CAIs is shown with the solid black line. The calculated nuclear field shift effect is shown using a dotted red line. The best-fit to the data for Nd is found using *a* = -5.

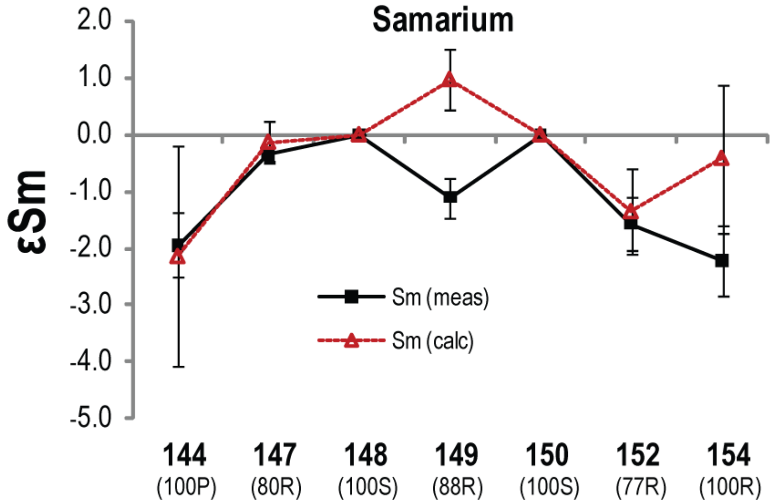

Figure A.10. Samarium nuclear field shift effects. The average Sm isotopic data from Allende CAIs is shown with the solid black line. The calculated nuclear field shift effect is shown using a dotted red line. The best-fit to the data for Sm is found using *a* = -13.

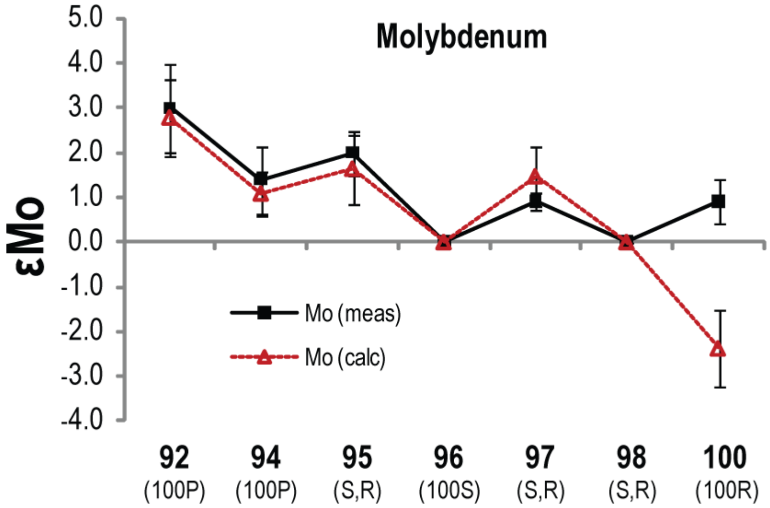

Figure A.11. Molybdenum nuclear field shift effects. The average Mo isotopic data from Allende CAIs is shown with the solid black line, as reported in Burkhardt et al. (2011). The calculated nuclear field shift effect is shown using a dotted red line. The best-fit to the data for Mo is found using *a* = -24.

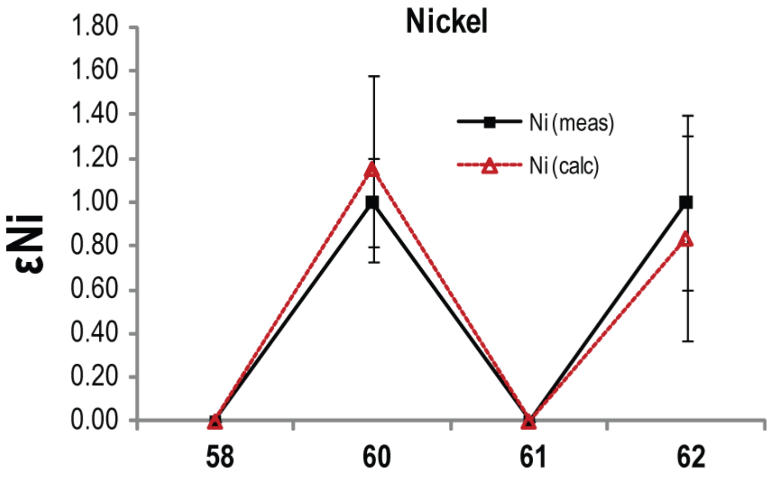

Figure A.12. Nickel nuclear field shift effects. The average Ni isotopic data from Allende CAIs is shown with the solid black line, as reported in Quitte et al. (2007). The calculated nuclear field shift effect is shown using a dotted red line. The best-fit to the data for Ni is found using *a* = 36.

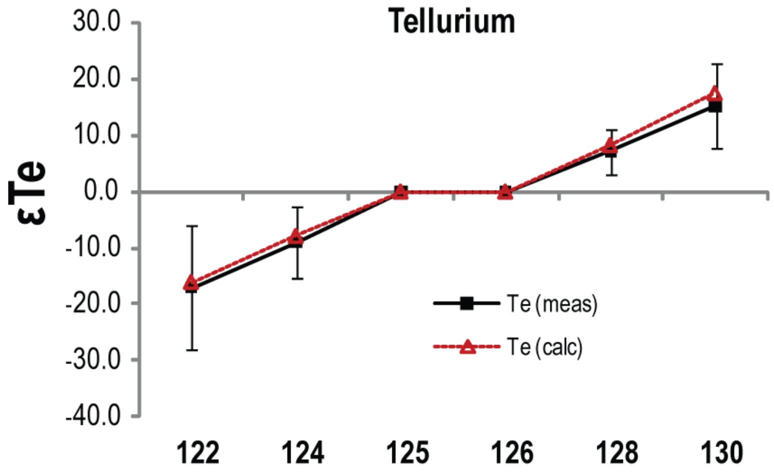

Figure A.13. Tellurium nuclear field shift effects. The average Te isotopic data from Allende CAIs is shown with the solid black line, as reported in Fehr et al. (2009). The calculated nuclear field shift effect is shown using a dotted red line. The best-fit to the data for Te is found using *a* = -160.

The isotopic anomaly patterns for many elements in Allende CAIs can roughly be explained by fractionation resulting from nuclear field effects; however mismatches in a few isotopes cause problems with this interpretation being the sole cause for the isotopic anomalies. For instance, the ^{135}Ba and ^{137}Ba peaks in the measured data are fairly well reproduced by the predicted data by optimizing *a*, however nuclear field shift effects would result in a large negative anomaly in ^{138}Ba not present in the measured data. Similarly, large differences exist between the measured and predicted patterns in ^{145}Nd, as well as ^{149}Sm and ^{154}Sm, regardless of the internal normalization of Sm. Other isotope systems have mixed results when comparing measured and predicted patterns. The measured Mo isotope pattern (Burkhardt et al. 2011) is tantalizingly similar to the predicted pattern, with the exception of ^{100}Mo, which is in disagreement by approximately 3.0ε. The measured patterns of Ni (Quitte et al. 2007) and Te (Fehr et al. 2009) are reproduced within error for all reported isotopes.

A.4.4.5 Supernovae input following CAI formation

One potential scenario to explain apparent *r*-process excesses in Ba and apparent *p*-, and *r*-process deficits in Nd and Sm is injection of a small amount of H-event (a subgroup of Type-II supernovae) supernovae material (Qian et al., 1998) between the time of CAI formation and condensation of the less refractory phases found in chondritic meteorites. H-event material is depleted in the *r*-process isotopes $A \leq 140$ (e.g., Ba) and enriched in *r*-process isotopes $140 \leq A \leq 200$ (e.g., Nd, Sm) (Nittler and Dauphas, 2006), therefore the addition of a small amount of this material to the solar protoplanetary disk from this type of supernova could theoretically explain the isotopic differences between CAIs and bulk Solar System material. This scenario continues to be investigated using supernova production models with regard to *p*-, *s*-, and *r*-isotope ratio variation.

A.5 CONCLUSION

Within analytical uncertainties, the non-radiogenic Ba, Nd and Sm isotope compositions of Allende CAIs analyzed in this study are identical, implying that these CAIs formed in a region with a homogeneous isotopic composition. However, this homogeneous isotopic composition of Allende CAIs is clearly distinct from the isotopic composition of bulk meteorites. This implies that CAIs and the rest of the bulk Solar System formed from two distinct reservoirs. At this time, it is unclear if these reservoirs are separated by 1) space (i.e., different regions of the disk), 2) time (i.e., change in the isotopic composition of the disk) or 2) a combination of both space and time.

APPENDIX B

STATEMENT OF PERMISSION FROM CO-AUTHORS

Co-authors on the previously published articles “Natural variations in uranium isotope ratios of uranium ore concentrates: Understanding the fractionation mechanism”, “Uranium isotope fractionation during adsorption to Mn-oxyhydroxides”, “Rapid expansion of oceanic anoxia immediately before the end-Permian mass extinction”, “^{238}U/^{235}U variations in meteorites: Extant ^{247}Cm and implications for Pb-Pb dating”, and “Adjustments to the ages of the angrite time anchors and the effect on short-lived chronometers” have granted their permission for use of the articles in this dissertation. This list of co-authors includes: T. Algeo, A. Anbar, J. Bargar, L. Borg, A. Herrmann, I. Hutcheon, P. Janney, M. Sharp, M. Wadhwa, L. Wasylenki, S. Weyer, and J. Zipfel.